

Validatable  
Shock-Wave/Turbulent  
Boundary-Layer  
Interaction over a  
Compliant Panel

C.J.G. De Petter



# Validatable Shock-Wave/Turbulent Boundary-Layer Interaction over a Compliant Panel

by

C.J.G. De Petter

to obtain the degree of Master of Science  
at the Delft University of Technology,  
to be defended publicly on Monday July 1, 2019 at 10:00 AM.

Student number:	4279387	
Project duration:	June 1, 2018 – July 1, 2019	
Thesis committee:	Prof. dr. ir. S. Hickel,	TU Delft, supervisor
	Dr. ir. B. W. van Oudheusden,	TU Delft
	Dr. ir. F. F. J. Schrijer,	TU Delft
	Dr. ir. G. E. Elsinga,	TU Delft
	L. Laguarda Sánchez, MSc,	TU Delft

*This thesis is confidential and cannot be made public until July 1, 2020.*

An electronic version of this thesis is available at <http://repository.tudelft.nl/>.



# Preface

For the last year (and one month), I have been working on the thesis you are about to read. It was an interesting period of my life, during which I first of all learned a lot about supersonic aerodynamics, fluid-structure interaction and plates that should definitely flutter but sadly do not. Most of all, I learned that hard work and discipline pay off, but that one must also take time off for the occasional beer to ensure you keep motivated throughout this (unexpectedly) long journey. Luckily, I had two excellent supervisors to accompany me on this trip. First of all I want to thank prof. dr. ir. Stefan Hickel for his indispensable advice and perseverance, especially when CalculiX had to be compiled once again. Secondly, I am very thankful to Lluís Laguarda Sánchez, who was always only a Whatsapp message from providing excellent insights and unrelenting optimism. Next to that, I want to express my gratitude towards the other thesis defence committee members, dr. ir. Bas van Oudheusden, dr. ir. Ferry Schrijer and dr. ir. Gerrit Elsinga.

Next to my supervisors, I was lucky to spend this last year together with many other fellow thesis students. I want to thank Jochem Claes, Laurent Declerck and Stephan Smets for the many coffee breaks and WoBo's, which were perfect occasions to get rid of stress by complaining about the tough thesis-life and by enjoying a nice "Karmelietje". Many thanks also to the other basement residents, which were always there to let me in when I forgot my card once again. A big thank you to fellow panel flutter expert Lucas Mathijssen, who has provided me with great insights and beautiful experimental results.

Lastly, I want to thank my family and friends for their continuous support during this period. Without them I would have not been able to deliver work of this quality, and I would have most certainly not finished writing this document yet. Many thanks also to Robbe Maselis, whose Latex genius was key to delivering an appealing report.

On a final note, I am proud of the work I have delivered, and I hope you will feel the same way after delving into this thesis. Enjoy the journey.

*C.J.G. De Petter  
Delft, July 2019*



# Summary

As a first step, a thorough literature study was executed to identify the parameters which govern panel flutter with shock impingement. Considering the structural parameters, the nondimensional dynamic pressure, the plate thickness, the shock impingement location and its distance from the impingement point of the first PME fan expansion wave are clearly the most dominant. From an aerodynamic point of view the Mach number, impinging shock strength, cavity pressure and Reynolds number have the most influence on the shock-panel interaction. The ST-15 mainly limits the nondimensional dynamic pressure through a limited total pressure range linked to the chosen Mach number, while strong limitations are also put on shock-generator dimensions and plate geometry. Lastly, the turbulent boundary layer characteristics are fixed for the chosen Mach number and total conditions in the settling chamber, and are well known from earlier experiments.

Next, an analytical study was conducted which implemented the Type III model by Ye and Ye [2018] for flutter of simply supported panels subject to an impinging shock. It was observed that implementing the shock by simply introducing a dynamic pressure jump and ignoring the steady pressure differences over the plate was a strong oversimplification. A shift of the flutter boundary towards lower dynamic pressures with increasing shocks strength was obtained, which was also observed by Visbal [2012, 2014], who coupled the Euler equations to a von Kármán plate. This effects was strongly underestimated though, while the initial stiffening effect predicted by Visbal was not obtained.

An attempt was made to improve the model by incorporating the transverse steady pressure difference over the plate. This led to a correct prediction of the initial damping of all panel motion, but this effect was found to not cease for higher shock strengths. This was attributed to the flowfield being too nonlinear to justify linear stability analysis. Based on preliminary analytical calculations it was found that nonlinearity is mainly linked to the impinging shock strength passively adapting to the panel slope at the shock impingement point and the significant Mach number variation along the panel chord, limiting the applicability of classic linear piston theory. Due to the same reason, flutter behaviour with varying shock impingement location was not predicted correctly either.

Since the unmodified analytical model seemed to yield an upper limit for the flutter dynamic pressure for shock strengths exceeding  $p_3/p_1 = 1.4$ , it was used as a means to estimate values for the governing structural and aerodynamic parameters for further inviscid analysis by CFD. Aluminium 7075-T6 was chosen for its high flexibility and relatively high yield strength, while the Mach number was set to 2.0. The cavity pressure was set to the average of the theoretical upper surface pressure to minimise panel stiffening, which should be attainable in the ST-15 by leaving the spanwise panel edges free and allowing pressure equalisation between the test section and the cavity. Assuming shock impingement at the panel midpoint and introducing a correction factor for clamped panels, it became clear that a panel thickness smaller than 0.4mm and a total pressure of 3.5 bars should be sufficient to ensure panel unsteadiness. Lastly, it was observed that shock strength should be maximised, leading to a proposed shock-system static pressure ratio of 3.0, close to the maximum attainable with a regular reflection.

As a next step, the Euler equations were loosely coupled to a FEM model of a clamped 2D panel, which were solved using INCA and CalculiX respectively. The panel response was found to be highly sensitive to shock impingement location. Two distinct unsteady regions were proven to exist, which yielded limit-cycle oscillations: close to the leading edge ( $0.05 \leq k \leq 0.20$ ) and around the panel midpoint ( $0.45 \leq k \leq 0.50$ ). Both regions showed a different sensitivity of the response amplitude and frequency with respect to  $k$ , with the upstream region displaying a reduction in amplitude and increase in frequency with increasing  $k$ , while the midpoint region shows an increase in amplitude and reduction in frequency with downstream movement of the shock. The sudden increase in frequency observed by Visbal [2014] for shock impingement close to the leading edge was not obtained, but a significantly different response for  $k = 0.05$  was seen. While all other shock locations induced a response involving mainly second and third mode content, the most upstream shock location induced a coupling of a high frequency second mode oscillation and a low frequency first mode response (one harmonic lower). Considering pressure fluctuations, unsteadiness was mainly observed near the panel trailing edge, which can be attributed to an alternating expansion-compression wave system.

These expansion and compression waves were found to originate at the panel leading edge and travel downstream towards the trailing edge at constant speed, where they were either amplified or damped depending on the panel slope at the trailing edge. The reflected shock showed a significant flapping motion, especially for  $k = 0.50$  which could be linked back to it being very sensitive to the local panel slope, as postulated during the analytical computations.

Considering parametric effects, increasing the panel thickness beyond  $h/a = 3.0 \times 10^{-3}$  was found to eliminate all panel motion. The effect of increasing the total pressure and thus the dynamic pressure in the tunnel was not as homogeneous, with oscillation amplitudes increasing with increasing  $p_{t,0}$  for  $k = 0.15$ , but all motion being damped for  $p_{t,0} \geq 4.0$  bar for  $k = 0.50$ . This was attributed to the mean deflection becoming too large, inducing enough stiffness to eliminate panel unsteadiness. This unexpected dependency of the flutter boundary on total pressure, and thus nondimensional dynamic pressure, led to a questioning of the latter as a valid parameter to characterise shock-induced panel flutter. Indeed, it was found that different combinations of dimensional quantities yielding the same  $\lambda$  can produce both damped and undamped oscillatory behaviour of the panel. It can thus be concluded that the nondimensional dynamic pressure is not a valid parameter to predict flutter, although it was observed that indeed no flutter occurred for  $\lambda$  values lower than the analytical flutter boundaries.

Based on the inviscid and analytical results, and with literature on SWBLI in mind, values for the governing parameters for future analysis by LES could finally be selected. By averaging the viscous pressure distribution obtained by Matheis and Hickel [2015], it was determined that the theoretical estimate for the averaged cavity pressure was only 5% off, justifying its use. Overlaying the 10 cm long panel with the interaction obtained by Matheis and Hickel [2015] at similar Mach number and shock strength, an inviscid impingement point halfway the panel was selected to position the expected separation shock foot in the unsteady region near the leading edge. To ensure a similar interaction extent, an experimental set-up was designed which yields the same distance between the inviscid shock impingement point and the impingement point of the first PME fan expansion wave. Careful selection of the wedge dimensions resulted in a set-up which should allow tunnel start-up and a quasi-2D interaction at the panel midplane. Based on previous results obtained in the ST-15, a boundary layer thickness Reynolds number  $Re_{\delta,ref}$  and a friction Reynolds number  $Re_{\tau}$  of  $238 \times 10^3$  and 3,552 respectively should be obtained. By selecting the grid distribution based on the well-resolved SWTBLI results by Pasquariello et al. [2017] and the grid extent based on inviscid results, a total amount of 438 million cells was estimated for the LES. Examining the inviscid transients obtained for  $k = 0.15$  and  $k = 0.50$ , a minimum integration-time of 205 flow-through times was estimated in order to resolve at least 10 low-frequency separation shock oscillations.

In short, it can be concluded that based on analytical and inviscid computations, a numerical set-up was obtained which should be feasible both from a computational and experimental point of view. Thus, the goal of the thesis was achieved with success.

# Contents

<b>Preface</b>	<b>iii</b>
<b>Summary</b>	<b>v</b>
<b>Nomenclature</b>	<b>ix</b>
<b>1 Introduction</b>	<b>1</b>
1.1 Motivation . . . . .	1
1.2 Research Question, Aims, and Objectives . . . . .	3
1.3 Experimental Set-up . . . . .	4
<b>2 Governing Equations</b>	<b>7</b>
2.1 Fluid . . . . .	7
2.2 Structure . . . . .	8
2.3 Fluid-Structure Interface Conditions . . . . .	9
<b>3 Shock-Panel Interactions</b>	<b>11</b>
3.1 Inviscid Flow . . . . .	11
3.2 Viscous Flow . . . . .	12
3.2.1 Low Frequency Unsteadiness . . . . .	13
3.2.2 Interaction Length . . . . .	14
3.2.3 Numerical Simulation of SWBLI . . . . .	17
3.2.4 Coupled SWBLI over a Compliant Panel . . . . .	17
3.3 Governing Parameters . . . . .	18
3.3.1 Structural Parameters . . . . .	19
3.3.2 Aerodynamic Parameters . . . . .	20
3.3.3 Initial Conditions and Boundary Conditions . . . . .	22
3.3.4 Other Parameters . . . . .	23
<b>4 Analytical Model for Shock-Panel Interaction</b>	<b>25</b>
4.1 Methodology . . . . .	25
4.1.1 Classic Panel Flutter . . . . .	25
4.1.2 Flutter of a Flat Plate Subject to an Impinging Shock . . . . .	27
4.1.3 Flutter of a Statically Deformed Panel Subject to an Impinging Shock . . . . .	31
4.2 Verification and Validation . . . . .	32
4.2.1 Python Script Outline . . . . .	32
4.2.2 Standard Panel Flutter . . . . .	33
4.2.3 Panel Flutter with Shock Impingement . . . . .	34
4.2.4 Panel Flutter with Deformed Equilibrium . . . . .	37
4.2.5 Discussion . . . . .	43
4.3 Design of Experiment . . . . .	44
<b>5 Numerical Approach</b>	<b>47</b>
5.1 Fluid Discretisation . . . . .	47
5.2 Structure Discretisation . . . . .	48
5.3 Coupling . . . . .	50
5.4 Turbulence Modelling . . . . .	51

<b>6</b>	<b>Two-Dimensional Inviscid Analysis</b>	<b>53</b>
6.1	Numerical Set-up, Boundary Conditions and Grid Distribution. . . . .	53
6.2	Postprocessing Methodology . . . . .	55
6.3	Results . . . . .	56
6.3.1	Effect of Shock Impingement Location. . . . .	56
6.3.2	Parametric Effects . . . . .	59
6.3.3	Effect of Initial Condition . . . . .	61
6.3.4	Adaptive Reduced Order Model . . . . .	61
6.3.5	Validity of $\lambda$ as a Parameter to Characterise Flutter. . . . .	61
<b>7</b>	<b>Selection of a Set-Up for Future Analysis by LES and Experiment</b>	<b>65</b>
7.1	Selection of Values for the Governing Parameters . . . . .	65
7.1.1	Aerodynamic Parameters . . . . .	65
7.1.2	Structural Parameters . . . . .	66
7.1.3	Initial Conditions and Boundary Conditions. . . . .	69
7.2	Numerical Set-Up. . . . .	69
7.3	Boundary Conditions and Grid Distribution . . . . .	71
7.4	Preliminary Experimental Results. . . . .	74
<b>8</b>	<b>Conclusion</b>	<b>77</b>
8.1	Conclusions. . . . .	77
8.2	Recommendations . . . . .	78
<b>A</b>	<b>Four Mode Jacobian Entries at the Flat Plate Equilibrium Solution</b>	<b>79</b>
<b>B</b>	<b>Entries for the Four Mode Routh-Hurwitz Criterion</b>	<b>81</b>
	<b>Bibliography</b>	<b>83</b>

# Nomenclature

## Acronyms

(D)DES	(Delayed) Detached-Eddy Simulation
(I)LES	(Implicit) Large-Eddy Simulation
2D	Two-Dimensional
3D	Three-Dimensional
ALDM	Adaptive Local Deconvolution Method
ALE	Arbitrary Lagrangian Eulerian
AROM	Adaptive Reduced Order Model
BC	Boundary Condition
CFD	Computational Fluid Dynamics
CFL	Courant-Friedrichs-Lewy
CNC	Computer Numerical Control
DF	Digital Filter
DNS	Direct Numerical Simulation
FEM	Finite Element Method
FP	Flutter Parameter
FSI	Fluid-Structure Interaction
FTT	Flow-Through Time
FV	Finite Volume
GP	Geometry Parameter
HIT	Homogeneous Isotropic Turbulence
HLLC	Harten-Lax-van Leer-Contact
IBM	Immersed Boundary Method
IC	Initial Condition
LCO	Limit-Cycle Oscillation
LiPT	Linear Piston Theory
LPT	Local Piston Theory
MTA	Modal Truncation Augmentation
ODE	Ordinary Differential Equation
PDE	Partial Differential Equation

PIV	Particle Image Velocimetry
PME	Prandtl-Meyer Expansion
RANS	Reynolds-Averaged Navier-Stokes
RMS	Root Mean Square
SGS	Subgrid Scale
SSME	Space Shuttle Main Engine
ST-15	Supersonic Tunnel (15x15 cm test section)
SW(T)BLI	Shock-Wave/(Turbulent) Boundary-Layer Interaction
TBL	Turbulent Boundary-Layer
TU(M/D)	Technological University (of Munich/of Delft)
WENO	Weighted Essentially Non-Oscillatory

### Latin symbols

$\bar{p}$	Nondimensional pressure
$\hat{\mathbf{t}}$	Vector of tractions
$\mathbf{D}$	Viscous part of the flux tensor
$\mathbf{d}$	Vector of unknown displacements
$\mathbf{E}$	Green-Lagrange strain tensor
$\mathbf{F}$	Inviscid part of the flux tensor
$\mathbf{f}$	Force
$\mathbf{G}$	Deformation gradient tensor
$\mathbf{I}$	Unit tensor
$\mathbf{K}$	Flux tensor or matrix of internal forces
$\mathbf{M}$	Mass matrix
$\mathbf{n}$	Normal vector
$\mathbf{P}$	First Piola-Kirchoff stress tensor
$\mathbf{S}$	Second Piola-Kirchoff stress tensor
$\mathbf{w}$	State vector containing conserved variables
$\mathcal{M}$	Mass ratio
$\mathcal{W}$	Virtual work
$\mathcal{R}$	Specific gas constant
$c$	Panel edge rotational constraint
$A$	Area or amplitude
$a$	Panel length
$b$	Panel width

---

$C_f$	Skin friction coefficient
$D$	Flexural rigidity
$E$	Total energy
$E_s$	Young's modulus
$f$	Frequency
$g$	Channel height or structural damping coefficient
$g^+$	Nondimensional channel height to wedge width ratio
$H$	Shape factor
$h$	Panel thickness
$J$	Jacobian
$j$	Imaginary number
$k$	Nondimensional shock impingement location
$L$	Distance between inviscid shock and expansion wave impingement points
$l^+$	Viscous lengthscale
$L_{sep}$	Separation extent
$M$	Mach number
$n$	Dynamic pressure ratio
$N_x$	Nonlinear stretching term
$p$	Pressure
$Pr$	Prandtl number
$q$	Dynamic pressure
$q$	Heat flux due to conduction
$r$	Recovery factor
$R_M$	Normalised mass ratio
$R_x$	Nondimensional nonlinear stretching term
$Re$	Reynolds number
$Re_\tau$	Friction Reynolds number
$St$	Strouhal number
$T$	Temperature
$t$	Time
$T_s$	Sampling period
$U$	Freestream velocity
$u_1, u_2, u_3$	Velocity components in $x$ , $y$ and $z$ directions
$u_\tau$	Friction velocity

---

$V$	Volume
$W$	Nondimensional deflection
$w$	Deflection or wedge width
$x, y, z$	Physical coordinates
<b>Greek symbols</b>	
$\alpha$	Damping factor
$\alpha_s$	Coefficient of thermal expansion
$\alpha_{ijk}$	Fluid volume fraction of cut-cell $\Omega_{ijk}$
$\beta$	Prandtl-Glauert factor
$\chi$	Interface exchange term
$\Phi$	Vector of orthonormalized eigenvectors
$\sigma_f$	Fluid stress tensor
$\sigma_s$	Cauchy stress tensor
$\tau$	Viscous stress tensor
$\delta$	Boundary layer thickness
$\delta_{ij}$	Kronecker delta
$\epsilon$	AROM threshold value
$\eta$	Mach number ratio
$\Gamma$	Fluid-structure interface
$\gamma$	Ratio of specific heats
$\kappa_f$	Coefficient of thermal conductivity
$\lambda$	Nondimensional dynamic pressure
$\lambda_{f,s}$	First Lamé parameter
$\mu_f$	Dynamic viscosity
$\mu_s$	Second Lamé parameter or shear modulus
$\nu_f$	Kinematic viscosity
$\nu_s$	Poisson ratio
$\Omega$	Computational domain
$\Omega_{ijk}$	Cut cell
$\phi$	Prony polynomial
$\Psi$	Strain energy density function
$\rho$	Density
$\sigma$	Shock angle
$\tau$	Nondimensional time

---

$\tau_w$	Wall shear stress
$\theta$	Momentum thickness or phase
$\varphi$	Structural free-vibration mode
$\vartheta$	Flow deflection angle
$\xi$	Nondimensional $x$ -coordinate

**Subscripts**

0	Settling chamber quantity
1	Test section quantity
3	Post shock system quantity
$\infty$	Freestream quantity
$c$	Quantity in cavity
$f$	Fluid quantity
$imp$	Quantity at shock impingement point
$in$	Incompressible quantity
$ref$	Reference value, usually defined at computational domain inlet
$s$	Structural quantity
$t$	Total quantity
$w$	Quantity at the wall or wedge quantity

**Superscripts**

*	Non-dimensional quantity
+	Wall unit
$T$	Transpose



# Introduction

In this master thesis, I give an overview of the work performed during my last year at the aerodynamics department of the Delft University of Technology. Most of the work was performed in the field of inviscid shock-panel interactions, using both analytical and numerical approaches. All these computations served as a means to identify a final test case for high fidelity coupled Large Eddy Simulation of a turbulent Shock-Wave/Boundary-Layer Interaction over a compliant panel and corresponding experiments in the ST-15 supersonic windtunnel.

In this chapter, an introduction to the problem at hand and motivation for the research is first given in Section 1.1. Next, the research questions, aims and objectives are introduced in Section 1.2, after which the experimental set-up is illustrated in Section 1.3.

The rest of the report is structured as follows. First, the equations governing the fluid and the structure are given in Chapter 2. Secondly, a concise literature review on inviscid and viscous shock-panel interactions, as well as an overview of the governing parameters, are presented in Chapter 3. Next, the validity of analytical models to predict shock-induced flutter is investigated in Chapter 4, which is followed by Chapter 5 outlining the numerical approach for the high-fidelity computations. Furthermore, the inviscid results are presented in Chapter 6, after which the chosen test case for further analysis by LES and experiments is introduced in Chapter 7. Lastly, conclusions and recommendations for future work are given in Chapter 8 respectively.

## 1.1. Motivation

Ever since the illusion of the sound barrier was broken by the German V2 missiles in the 1940s, supersonic flows have been of strong technological interest. In recent years, the space economy has boomed, sitting at a current global size of around 340 billion USD according to the FAA. Supersonic transport has also seen a recent growing interest, but issues remain with supersonic propulsion [Candel, 2004]. Indeed, the occurrence, and the lack of understanding, of so-called Shock-Wave/Boundary-Layer Interactions (SWBLI) in supersonic air intakes still poses significant challenges in the efficient design of such devices. SWBLI also occurs during the start-up of typical rocket engines. Since the nozzle is designed for maximum efficiency at high altitudes, highly-overexpanded conditions occur at sea level. For typical thrust-optimized parabolic (TOP) nozzles, this implies the occurrence of a shock in the nozzle during start-up and consequent internal flow separation. This is illustrated in Fig. 1.1(a), where the separation shock foot in the Space Shuttle Main Engine (SSME) during start-up can be clearly seen. Strong SWBLI can be observed during this transient process, as shown by a sketch of typical TOP nozzle Free Shock Separation (FSS) in Fig. 1.1(b), which continues until the nozzle flow is fully developed [Pasquariello, 2018]. This can lead to strong asymmetric side-loads in the nozzle, which are known to be very unsteady [Östlund and Muhammad-Klingmann, 2005]. Similar interactions can be found in turbomachinery cascades [Flaszynski et al., 2015] and around hypersonic vehicles, helicopter blades, missiles [Délery and Dussauge, 2009; Pasquariello et al., 2015] or in (sc)ramjet shocktrains [Idris et al., 2014].

SWBLI is well understood from a mean-flow point of view, both in the case of a weak and strong interaction. The latter indicates that mean flow separation occurs due to the adverse pressure gradient imposed by the shock. In this case, complex unsteady interactions involving the separated shear layer, the incident shock and

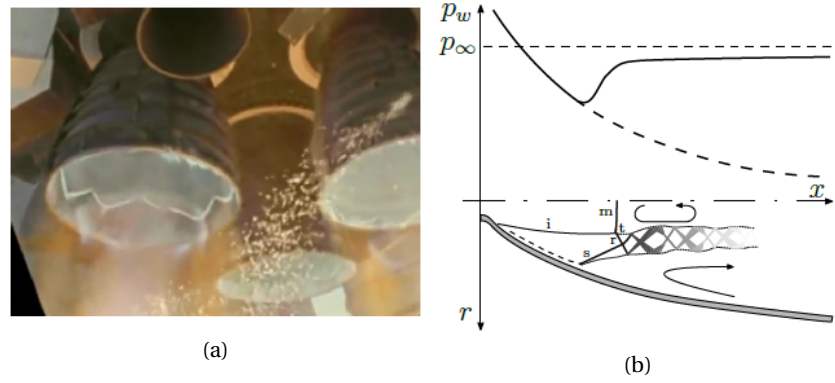


Figure 1.1: Unsteady separation line during SSME start-up (left) and schematic of a TOP nozzle Free Shock Separation (right) [Pasquariello, 2018]

the separation bubble take place. The unsteadiness associated to these interactions still puzzles researchers up to today [Clemens and Narayanaswamy, 2014]. It is well known that the interaction between the impinging shock and a turbulent boundary layer induces low-frequency separation shock motions, which can couple with the eigenmodes of the structure. This can lead to fatigue, and an in-depth understanding of the problem is thus required to ensure safe future designs of high-speed machinery.

The problem in the understanding of SWBLI and its coupling with compliant structures lies in the fact that usually turbulent flows at high Reynolds numbers are involved. Next to that, long integration times are required to capture the entire frequency-spectrum associated to the interaction, leading to extremely high computational cost. Up to today, only one well-resolved Large-Eddy Simulation (LES) of coupled SWTBLI has been performed by Pasquariello et al. [2015], which features a shock being introduced by a moving wedge. The panel response is illustrated in Fig. 1.2, where it can be observed that a damped panel motion is obtained in the corresponding experiment by Daub et al. [2015b], while an oscillatory motion is obtained numerically. This was attributed to 1) the compressed air in the cavity acting as an aerodynamic spring and consequently dampening the panel motion and 2) the cavity not being perfectly sealed from the test-section by the installed layer of soft-rubber foam, which resulted in cavity pressure fluctuations and unknown structural damping due to the foam. Thirdly, additional uncertainty was introduced by post-rotation vibrations of the shock-generator, the frequency of which was very close to the unsteady motion of the shock foot. A strong need thus arises for a high-fidelity computational set-up which can be validated in experimental facilities. Since this thesis is conducted at Delft University of Technology, it would be desirable to design the simulation in such a way that it can be replicated in the local ST-15 supersonic blowdown windtunnel. Therefore, the focus of this thesis will be the identification of a test case which will yield strong unsteady motion in a future coupled LES, while also being reproducible in the ST-15.

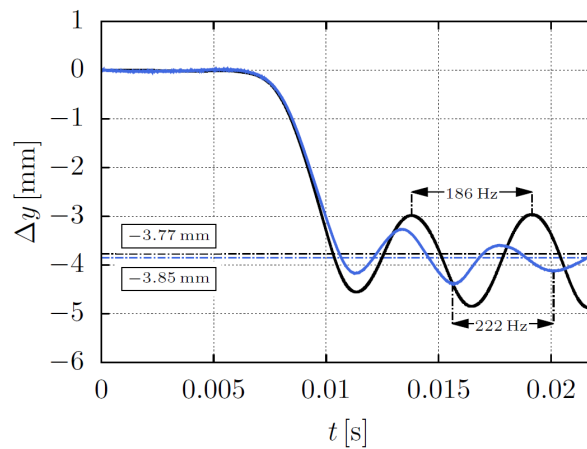


Figure 1.2: Experimental panel response [Daub et al., 2015b] (blue) versus computed panel response [Pasquariello et al., 2015] (black)

## 1.2. Research Question, Aims, and Objectives

In order to guide the research conducted for the thesis, research questions and corresponding research objectives have to be defined. These were identified based on an earlier executed research study, which is partially summarised in Chapter 3.

**Research Question 1:** *Which structural and aerodynamic parameters will ensure shock-induced supersonic panel flutter with amplitudes on the order of the panel thickness in conditions attainable in the ST-15 wind-tunnel?*

- **Sub-question 1:** *What are the structural and aerodynamic parameters governing supersonic panel flutter with shock impingement?*
- **Sub-question 2:** *Based on analytical computations, which aerodynamic and structural parameters will yield unsteady behaviour of the panel?*
- **Sub-question 3:** *Based on 2D Euler computations, which aerodynamic and structural parameters will yield the largest unsteady deformation of the panel, and should therefore be selected for the final LES set-up?*

**Research Question 2:** *Can the designed numerical experiment be replicated in the ST-15 windtunnel, allowing validation of the numerical method?*

- **Sub-question 1:** *Can the numerical boundary conditions be replicated in the ST-15 windtunnel?*
  - **Subsub-question 1:** *Are the panel leading and trailing sufficiently clamped to replicate perfectly clamped boundary conditions?*
  - **Subsub-question 2:** *Are the windtunnel cavity pressure fluctuations small enough to justify prescribing a steady numerical cavity pressure?*
  - **Subsub-question 3:** *Does the windtunnel cavity pressure equal the time-average of the static pressure on the upper panel surface?*
  - **Subsub-question 4:** *Does the wedge trailing edge expansion fan affect the impinging shock?*
- **Sub-question 2:** *Does the initial condition of the windtunnel, i.e. the normal shock generated during wind-tunnel start-up, affect the converged statistically stationary panel response?*
- **Sub-question 3:** *Do the chosen aerodynamic and structural parameters yield an experimental set-up which allows comparison with an LES with assumed homogeneity in the spanwise direction?*

The objective of the research project is to design a numerical experiment which will allow validation of the coupled implicit large-eddy simulation approach first employed by Pasquariello et al. [2015] to resolve coupled shock-wave/turbulent boundary-layer Interaction by being reproducible in the ST-15 supersonic wind-tunnel at Delft University of Technology. Significant Fluid-Structure Interaction (FSI) can be ensured by first identifying the structural and aerodynamic parameters which induce panel flutter in feasible tunnel conditions by employing the analytical model by Ye and Ye [2018] and extending the work by Visbal [2012, 2014] on 2D inviscid shock-panel interactions.

- **Sub-objective 0:** *Identify the structural and aerodynamic parameters which govern panel flutter with shock impingement.*
- **Sub-objective 1:** *Identify the bounds imposed by the ST-15 on these parameters.*
- **Sub-objective 2:** *Implement the analytical model by Ye and Ye [2018] and attempt to replicate the inviscid shock-panel interaction results by Visbal Visbal [2012, 2014] to verify the model.*
- **Sub-objective 3:** *Use the analytical model to identify which feasible structural and aerodynamic parameters will yield unsteady behaviour of the panel.*
- **Sub-objective 4:** *Use the flow solver INCA coupled with the structural solver CalculiX to solve the Euler equations and determine the test case with the largest unsteady behaviour, based on the analytical results and the ST-15 limitations.*
- **Sub-objective 5:** *Compare the inviscid results to the analytical predictions to verify the applicability of the analytical model.*
- **Sub-objective 6:** *Investigate the effect of different initial conditions on the long-time integration panel response using the 2D inviscid set-up.*
- **Sub-objective 7:** *Determine the key differences between the current inviscid and future viscous results, and how these will affect the LES result.*
- **Sub-objective 8:** *Based on literature and the inviscid results, determine the final LES test case which is feasible from a computational point of view, while also being reproducible in the ST-15.*

For the analytical computations, a sufficiently powerful workstation is made available to the author. For the consequent 2D inviscid computations, a significant increase in computational cost is expected due to the long integration times, which is alleviated by using the high performance cluster of the aerodynamics group at Delft University of Technology.

### 1.3. Experimental Set-up

As discussed in the previous sections, the goal of this thesis is to identify a numerical experiment which is reproducible in the ST-15. Therefore, the experimental set-up has to be designed with tunnel limitations in mind. The ST-15 supersonic windtunnel is a blow-down type tunnel and is located at the Faculty of Aerospace Engineering at Delft University of Technology. It was the first supersonic tunnel to be put in use at the faculty, but thanks to the possibility of long running times it is still frequently operated. Its configuration is illustrated in Fig. 1.3.

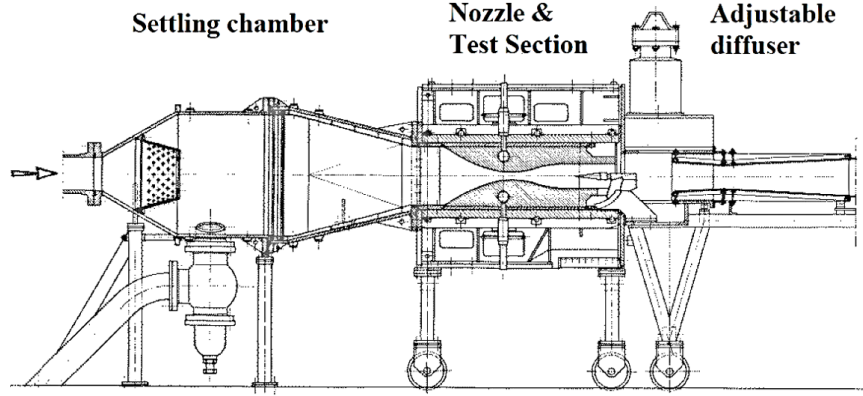


Figure 1.3: Schematic of the ST-15 supersonic windtunnel [Sun, 2014]

Test section Mach numbers of 1.5, 2, 2.5 and 3 can be obtained by installing the appropriate set of liners. Next to that, each Mach number  $M$  requires a minimum total pressure in the settling chamber for the tunnel to start. This is necessary to overcome the backpressure of one bar to guarantee the start-up normal shock is swallowed. Another requirement for tunnel start-up is no choked flow in the test section. Choking of the flow can occur when the shock generator creates a nozzle with an area ratio larger than the critical area ratio at the Mach number behind the start-up normal shock. This will be elaborated on in Section 7.1.2. An overview of the tunnel total pressure range is given in Table 1.1. The test section cross section measures 150 by 150 mm, while panels are more limited in size due to room being required for the panel edge clamps. This effectively limits the length and width of the compliant plate to approximately 100 mm.

$M_1$ [–]	Minimum $p_{t,0}$ [bar]	Maximum $p_{t,0}$ [bar]
1.5	2.4	4.8
2.0	2.4	4.8
2.5	4	8
3.0	6	12

Table 1.1: Total pressure ranges for different Mach numbers in the ST-15 windtunnel

A 2D cross-section of a possible set-up is shown in Fig. 1.4, as employed by Daub et al. [2015b] and replicated numerically by Pasquariello et al. [2015]. Depending on the total pressure  $p_{t,0}$  and temperature  $T_{t,0}$  in the settling chamber, and the chosen set of liners, a certain static pressure  $p_1$ , temperature  $T_1$ , density  $\rho_1$  and freestream Mach number  $M_1$  will be obtained in the test section. Note that settling chamber conditions are indicated by the subscript 0, while test section conditions are indicated by the subscript 1. The computed flowfield will depend on the chosen numerical method, since for the inviscid cases no (turbulent) boundary layer will be simulated. An impinging oblique shock can be generated by a wedge, which spans nearly the entire test section [Kallarail, 2016]. The shock generated by the flow turning angle  $\vartheta_w$  of the wedge will have a certain angle  $\sigma_1$  with respect to the freestream, and, in the inviscid case, will impinge on the flexible panel at the theoretical inviscid impingement point  $x_{imp}$ . After impingement, the shock will reflect, creating the post

shock-system state  $p_3$ . Note that the wedge expansion fan might or might not interact with the shock-system, depending on the relative position of the wedge and the panel. In the viscous case, the shock will interact with the boundary layer, leading to spreading of the pressure jump and complex SWTBLI, as will elaborated on in Section 3.2. The thickness of the TBL at the test section inlet, 2.5cm upstream of the panel leading edge, is defined by  $\delta_{ref}$ , and depends on the flow conditions. Typical freestream and boundary layer properties for Mach 2 experiments in the ST-15 are given in Table 1.2. Note that the boundary layer naturally develops to a turbulent state before the test section is reached.

	$p_{t,0}$ [bar]	$T_{t,0}$ [K]	$U_1$ [m/s]	$\delta_{ref}$ [mm]	$H_{in}$ [-]	$u_\tau$ [m/s]	$C_f$ [-]	$Re$ [1/m]
Sun et al. [2012]	3.20	290	534	6.0	1.20	19.0	2.6E-3	35.0E6
Giepman et al. [2014]	3.20	290	524	5.2	1.23	20.8	1.9E-3	42.2E6
Kallarail [2016]	3.20	278	492	5.2	1.30	19.6	1.9E-3	43.5E6
Nayak et al. [2017]	3.20	278	492	5.2	1.30	19.5	1.9E-3	43.5E6
Tambe et al. [2017]	3.15	267	487	6.0	1.26	19.5	1.9E-3	46.2E6

Table 1.2: Typical boundary layer properties for Mach 2.0 experiments in the ST-15

Concerning the panel, it is assumed the leading and trailing edges are perfectly clamped. The panel has a certain length  $a$ , width  $b$  and thickness  $h$ , and is free at the spanwise edges, promoting 2D motion of the plate and leading to pressure equalisation between the cavity and the testsection. The pressure acting on the lower side of the panel is called the cavity pressure  $p_c$ , analogous to the cavity existing in the windtunnel. Lastly, the panel will be manufactured of a certain metal, with as material properties a Young's modulus  $E_s$ , a Poisson ratio  $\nu_s$ , a yield stress  $\sigma_y$  and a density  $\rho_s$ .

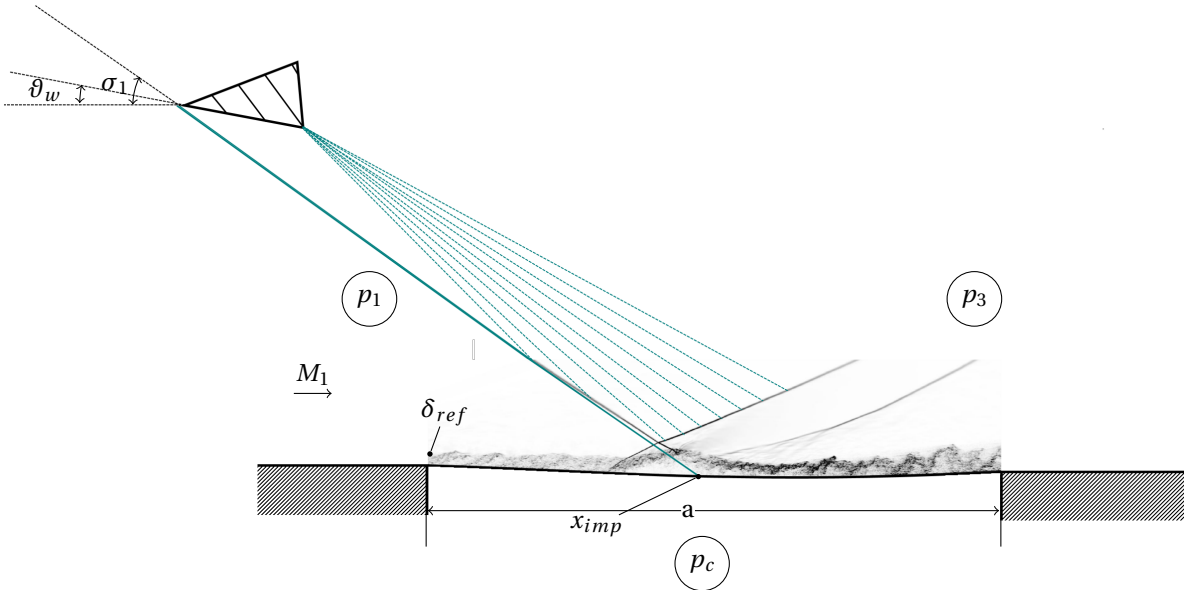


Figure 1.4: 2D view of a possible experimental set-up, adapted from Pasquariello et al. [2015]



# 2

## Governing Equations

Since the interaction between air and a metallic panel is considered, the computational domain  $\Omega$  must be divided in non-overlapping fluid and structural sub-domains, which yields  $\Omega = \Omega_f \cup \Omega_s$ . These domains are separated by a boundary  $\Gamma$ . The general equations governing the physics in the fluid and structural sub-domain are introduced in Section 2.1 and Section 2.2 respectively. Note that, if required, the subscript  $f$  will be used to indicate a fluid quantity, while the subscript  $s$  will be employed to indicate structural quantities.

### 2.1. Fluid

The fluid considered in the domain  $\Omega_f$  is air, which is assumed to behave as a perfect gas with a specific-heat ratio  $\gamma$  of 1.4 and a specific gas constant  $\mathcal{R}$  of 287.05 J/(kg K). It is governed by the three-dimensional Navier-Stokes equations, presented here in conservative form:

$$\frac{\partial \mathbf{w}}{\partial t} + \nabla \cdot \mathbf{K}(\mathbf{w}) = 0, \quad (2.1)$$

where the state vector  $\mathbf{w} = [\rho_f, \rho_f u_1, \rho_f u_2, \rho_f u_3, E]^T$  contains the conserved variables and thus implies the conservation of density  $\rho_f$ , momentum  $\rho_f \mathbf{u}$  and total energy  $E$ . The components of the flux tensor  $\mathbf{K}(\mathbf{w}) = [\mathbf{K}^{(1)}, \mathbf{K}^{(2)}, \mathbf{K}^{(3)}]$  are given by

$$\mathbf{K}^{(i)}(\mathbf{w}) = \mathbf{F}^{(i)}(\mathbf{w}) + \mathbf{D}^{(i)}(\mathbf{w}) = \begin{bmatrix} \rho_f u_i \\ \rho_f u_1 u_i + \delta_{i1} p \\ \rho_f u_2 u_i + \delta_{i2} p \\ \rho_f u_3 u_i + \delta_{i3} p \\ u_i (E + p) \end{bmatrix} - \begin{bmatrix} 0 \\ \tau_{i1} \\ \tau_{i2} \\ \tau_{i3} \\ u_k \tau_{ik} - q_i \end{bmatrix}, \quad (2.2)$$

where  $\mathbf{F} = [\mathbf{F}^{(1)}, \mathbf{F}^{(2)}, \mathbf{F}^{(3)}]^T$  and  $\mathbf{D} = [\mathbf{D}^{(1)}, \mathbf{D}^{(2)}, \mathbf{D}^{(3)}]^T$  are the inviscid and viscous contributions respectively. If viscosity is deemed negligible and therefore an inviscid fluid is assumed, the viscous flux tensor  $\mathbf{D}$  can be omitted. For a Newtonian fluid, the viscous stress tensor  $\tau_{ij}$  is given by

$$\tau_{ij} = \mu_f \left( \frac{\partial u_i}{\partial x_j} + \frac{\partial u_j}{\partial x_i} \right) + \lambda_f \frac{\partial u_k}{\partial x_k} \delta_{ij}. \quad (2.3)$$

Following Stoke's hypothesis, the bulk viscosity is assumed to equal zero, which allows Lamé's first parameter  $\lambda_f$  to be written in function of the dynamic viscosity:

$$\lambda_f = -\frac{2}{3} \mu_f. \quad (2.4)$$

The heat flux  $q_i$  due to conduction can be obtained through Fourier's law, where it is assumed  $q_i$  is proportional to the temperature gradient by the coefficient of thermal conductivity  $\kappa$ :

$$q_i = -\kappa_f \frac{\partial T}{\partial x_i}. \quad (2.5)$$

The state variables pressure  $p$  and temperature  $T$  can be obtained from the density  $\rho_f$  through the ideal-gas equation of state

$$p = \rho_f \mathcal{R} T, \quad (2.6)$$

and the definition of total energy

$$E = \frac{p}{\gamma - 1} + \frac{1}{2} \rho_f u_i u_i. \quad (2.7)$$

The temperature dependence of the dynamic viscosity  $\mu_f$  and the thermal conductivity  $\kappa_f$  is given by Sutherland's law and by assuming a constant Prandtl number  $Pr = 0.72$ .

$$\mu_f = \mu_{f,ref} \frac{T_{ref} + C}{T + C} \left( \frac{T}{T_{ref}} \right)^{3/2} \quad (2.8)$$

$$\kappa_f = \frac{\gamma \mathcal{R}}{(\gamma - 1) Pr} \mu_f \quad (2.9)$$

The reference states are  $T_{ref} = 293.15$  K and  $\mu_{ref} = 18.21 \times 10^{-6}$  Pas, while the constant  $C$  equals 122 K.

## 2.2. Structure

The structural sub-domain  $\Omega_s$  is governed by the local form of the balance of linear momentum, given by:

$$\rho_{s;0} \frac{\partial^2 \mathbf{d}}{\partial t^2} = \nabla_0 \cdot (\mathbf{G} \cdot \mathbf{S}) + \hat{\mathbf{b}}_0, \quad (2.10)$$

which describes an equilibrium between the work done by the inertial forces and the internal and external forces expressed in terms of the undeformed configuration  $\Omega_s$ . In Eq. (2.10),  $\mathbf{d}$  represents the vector of unknown displacements,  $\rho_{s;0}$  is the density of the structural material,  $\nabla_0 \cdot (\cdot)$  denotes the material divergence operator, and  $\hat{\mathbf{b}}_0$  is the vector containing the external material body forces. The unknown internal forces can be computed from the first Piola-Kirchoff stress tensor  $\mathbf{P} = \mathbf{G} \cdot \mathbf{S}$ , where  $\mathbf{G}$  and  $\mathbf{S}$  are the deformation gradient tensor and the second Piola-Kirchoff stress tensor respectively. The latter equals

$$\mathbf{S} = \frac{\partial \Psi}{\partial \mathbf{E}}. \quad (2.11)$$

By assuming a hyperelastic Saint Venant-Kirchoff material model, a constitutive equation for the unknown stresses is obtained. The associated strain energy density function  $\Psi$  is given by

$$\Psi(\mathbf{E}) = \frac{\lambda_s}{2} [\text{tr}(\mathbf{E})]^2 + \mu_s \text{tr}(\mathbf{E}^2), \quad (2.12)$$

where  $\lambda_s$  and  $\mu_s$  denote Lamé's first and second parameter.  $\mathbf{E}$  represents the Green-Lagrange strain tensor, which is given by

$$\mathbf{E} = \frac{1}{2} (\mathbf{G}^T \cdot \mathbf{G} - \mathbf{I}). \quad (2.13)$$

For later use in Section 2.3, the Cauchy stress tensor, or so-called true stress tensor, is defined as

$$\boldsymbol{\sigma}_s = \frac{1}{J} \mathbf{P} \cdot \mathbf{G}^T, \quad (2.14)$$

where  $J$  represents the Jacobian. In order to solve the governing structural equation, boundary conditions have to be specified on  $\partial\Omega_s = \Gamma_{S,D} \cup \Gamma_{S,N} \cup \Gamma$ . Displacements  $\mathbf{d}$  are imposed on the Dirichlet boundary  $\Gamma_{S,D}$ , while tractions  $\hat{\mathbf{t}}_0 = \mathbf{P} \cdot \mathbf{n}_0$  are prescribed on the Neumann segment  $\Gamma_{S,N}$ . For the computation of the traction,  $\mathbf{n}_0$  denotes the unit normal vector in material configuration. Furthermore, initial displacements and velocities have to be specified:

$$\mathbf{d}^0 = \mathbf{d}(t = 0) \quad \text{on} \quad \Omega_s, \quad (2.15)$$

$$\dot{\mathbf{d}}^0 = \dot{\mathbf{d}}(t = 0) \quad \text{on} \quad \Omega_s. \quad (2.16)$$

### 2.3. Fluid-Structure Interface Conditions

Since an interface exists between the fluid and solid subdomains, coupling conditions have to be specified on  $\Gamma$ . In order to ensure dynamic equilibrium, the tractions imposed by the flow and the structure have to be equal:

$$\boldsymbol{\sigma}_f^\Gamma \cdot \mathbf{n}^\Gamma = \boldsymbol{\sigma}_s^\Gamma \cdot \mathbf{n}^\Gamma, \quad (2.17)$$

where  $\boldsymbol{\sigma}_s$  is the Cauchy stress tensor given by Eq. (2.14) and  $\boldsymbol{\sigma}_f$  is the fluid stress tensor. The latter features both a normal inviscid component and a tangential viscous part, i.e.  $\boldsymbol{\sigma}_f = -p\mathbf{I} + \boldsymbol{\tau}$ . Secondly, the kinematic no-slip boundary condition is formulated as follows:

$$\frac{\partial \mathbf{d}^\Gamma}{\partial t} = \mathbf{u}^\Gamma. \quad (2.18)$$

For an inviscid flow, the kinematic boundary condition reduces to matching normal velocities at the interface

$$\frac{\partial \mathbf{d}^\Gamma}{\partial t} \cdot \mathbf{n}^\Gamma = \mathbf{u}^\Gamma \cdot \mathbf{n}^\Gamma. \quad (2.19)$$

Concerning the thermal loads on the structure, the fluid-structure interface is modelled as an adiabatic wall. No heat transfer thus occurs from the fluid to the structure, and the latter can therefore be assumed to be isothermal.



# 3

## Shock-Panel Interactions

Shock-Wave/Turbulent Boundary-Layer Interaction over a compliant structure is a complex problem. SWT-BLI involves the fields of shock reflection/interaction, boundary layer theory and fluid-structure interaction. Inviscid shock reflection is not elaborated on here, as it is well understood for (quasi-)steady flows. For more information on this topic, which includes theory on regular and irregular interactions, and criteria for transition from one to the other, the reader is referred to the work by Ben-Dor [2007] and Shapiro and Shapiro [1987].

To reduce the complexity of the problem, inviscid oblique shock-panel interactions are first introduced in Section 3.1. Next, the state-of-the-art regarding viscous interactions, or shock-wave/boundary-layer Interactions, is elaborated on in Section 3.2.

### 3.1. Inviscid Flow

The interaction between an impinging oblique shock and a flexible panel has been mainly investigated by coupling a nonlinear von Kármán plate to the Euler equations [Boyer et al., 2016, 2018; Visbal, 2012, 2014]. The latter are given by Eq. (2.2) if the viscous part is omitted. A derivation of the von Kármán equations can be found in e.g. Fung [1965], and entails the following assumptions: a thin plate with deflections on the order of the panel thickness, a small panel curvature everywhere, negligible tangential displacements, and small strains which vary linearly with the plate thickness. In all publications, the pressure acting on the lower side of the panel, usually called the cavity pressure  $p_c$  analogous to the cavity present in wind tunnels, is set to the theoretical average of the oblique shock reflection on the flow-side. This boils down to setting

$$p_c = k \cdot p_1 + (1 - k) \cdot p_3, \quad (3.1)$$

where  $p_1$  and  $p_3$  are the static pressure up- and downstream of the shock system respectively, and  $k$  is the nondimensional shock impingement point  $x_{imp}/a$ . Note that  $a$  is the length of the panel. Prescribing this cavity pressure yields a zero net steady pressure difference, and thus a minimal stiffening of the plate. As a result, Visbal [2012, 2014] observed interesting simply-supported panel dynamics with increasing shock strength, which were similar for Mach 2.0 and 2.5. For a theoretical shock-system pressure ratio of  $p_3/p_1 = 1.2$ , a steady deformed solution was obtained, which was attributed to the corresponding stiffening of the plate. When the shock strength was increased to  $p_3/p_1 = 1.4$ , increased flutter amplitudes and frequency were obtained at the same flutter dynamic pressure as the no-shock case, but only if a flat plate initial condition was prescribed. This is illustrated in Fig. 3.1. Note that in literature on flutter the dynamic pressure  $q = 0.5\rho U^2$  is usually nondimensionalised as shown by Eq. (3.4), yielding  $\lambda$ . Initiating the simulation with a previously obtained deformed panel resulted in an elimination of all unsteadiness. This subcritical bifurcation was found to shift to a supercritical instability for higher shock strengths ( $p_3/p_1 \geq 1.8$ ), yielding a strong reduction in flutter dynamic pressure. Visbal [2014] also investigated the effect of shock impingement points forward of the panel midpoint. Moving from  $k = 0.5$  towards the leading edge, more specifically to  $k$  values of 0.43 and 0.18, a monotonic increase in flutter frequency was observed. At  $k = 0.25$  and 0.38 though, the LCO disappeared and a steady deflected solution was obtained.

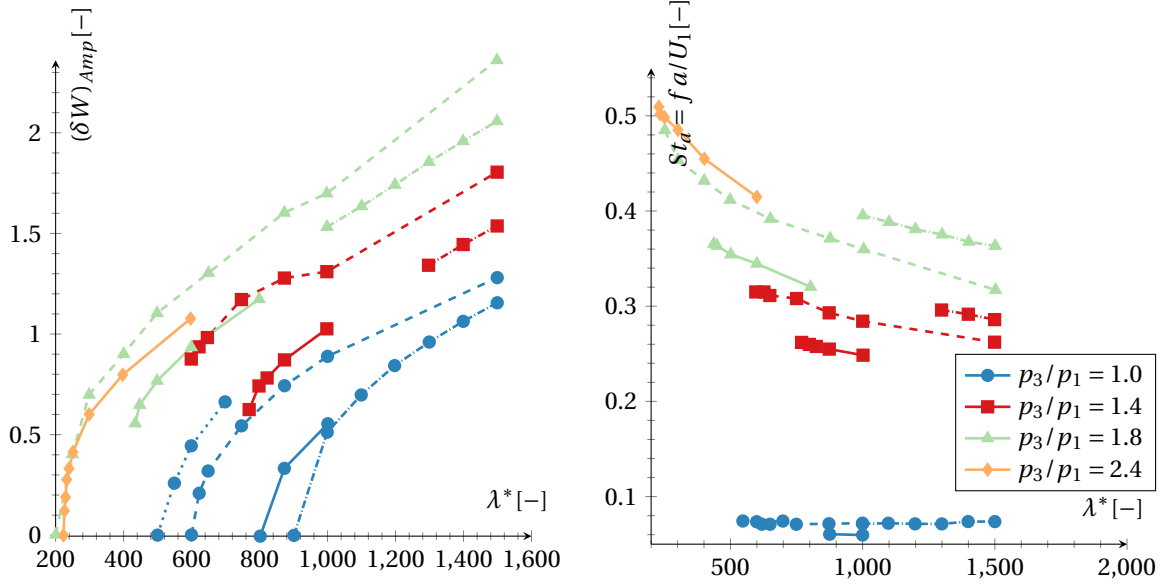


Figure 3.1: Flutter amplitude (left) and frequency (right) versus dynamic pressure for different shock strengths and Mach numbers for simply supported panels (2D:  $\cdots$   $M = 1.8$  [Gordnier and Visbal, 2002]  $-\ -$   $M = 2.0$  [Visbal, 2012]  $—$   $M = 2.5$  [Visbal, 2014], 3D:  $-\ - -$   $M = 2.0$  [Boyer et al., 2018])

In three dimensions, behaviour similar to 2D panels was observed for pinned-pinned rectangular panels by Boyer et al. [2018], although the subcritical bifurcation was found to persist up to the highest considered shock strength  $p_3/p_1 = 1.8$ . This was attributed to the additional stiffness introduced by the spanwise constraints, and it is therefore argued by the authors that supercritical bifurcations will also emerge for stronger shocks. It must be noted that a dominant 3D mode was introduced into the flutter motion, and that significant spanwise bending of the shock was obtained.

In short, it can be concluded that the mean panel deformation induced by shock impingement will yield a completely new aeroelastic instability, which differs strongly from classical panel flutter. The flutter dynamic pressure, amplitudes and frequencies for the latter can be excellently predicted for  $M \geq 2.0$  by coupling Linear Piston Theory, given by Eq. (3.2), to nonlinear structural models, for example a von Kármán plate.

$$p(x, t) = p_\infty + \frac{2q_\infty}{M_\infty} \left( \frac{\partial w}{\partial x} + \frac{1}{U_\infty} \frac{\partial w}{\partial t} \right) \quad (3.2)$$

Classical work by author's such as Dowell and Voss [1965] and Dowell [1966, 1967] is still accurate and computationally cheap, and excellent overviews on the topic are given by Dowell [1970] and Mei et al. [1999]. A similar method was employed by Ye et al. [2018] and Ye and Ye [2018] to analyse the linear stability of a flat plate subject to an impinging shock. The shock was included by simply imposing a dynamic pressure jump at the shock impingement point  $k$ . Transverse loads were thus completely ignored. The methodology behind this low fidelity model and the ability of the method to predict shock-panel interactions are elaborated on in Chapter 4.

### 3.2. Viscous Flow

If the viscosity of the fluid is not neglected, boundary layer theory comes into play. The fluid is then governed by the full Navier-Stokes equations, given by Eq. (2.2). The interaction between an impinging shock and a (turbulent) boundary layer is known as a shock-wave/(turbulent) boundary-layer interaction. The mean-flow structure of Shock-Wave/Boundary Layer Interactions has been extensively researched in the past, and is therefore well understood. An excellent review on the general flow phenomena associated with SWBLI is given by Déleury and Dussauge [2009]. Both laminar and turbulent interactions are considered, but since nearly all real-life occurrences of SWBLI involve turbulent boundary layers [Alder, 2015], focus will be put on the latter. The phenomenon differs depending on whether a weak or a strong interaction is considered. A strong interaction entails that the adverse pressure gradient imposed by the shock is sufficiently strong to induce mean flow separation, in contrast to the incipient separation induced by weak shocks. This sepa-

ration is known to create complex interactions involving the separated shear layer, the incident shock and the separation bubble, which can lead to a low-frequency motion of the separation shock [Clemens and Narayanaswamy, 2014]. This unsteadiness is elaborated on in Section 3.2.1.

As shown in the schematic of a typical strong SWTBLI presented in Fig. 3.2, the adverse pressure gradient imposed by a strong shock will lead to separation upstream of the inviscid shock impingement point. This is known as the upstream influence paradox [Steinrück, 2011; Stewartson and Williams, 1969], and can be attributed to pressure waves being transmitted upstream through the subsonic part of the boundary layer, which in turn leads to a thickening of the TBL. This thickened part of the boundary layer acts as a compression ramp, inducing the formation of compression waves. These coalesce into the separation shock, which consequently interacts with the impinging shock. Thus, in the case of a strong interaction, the field of shock-shock interference adds additional complexity to the problem of SWTBLI. For more information on this topic, the reader is again referred to the book by Ben-Dor [2007]. It has been shown that the strength of the separation shock and the separation-bubble pressure plateau depend only on the upstream conditions, and not on the downstream flow nor the downstream geometry. This "free-interaction" theory was first proposed by Chapman et al. [1957], and has been proven experimentally [Pasquariello, 2018]. Regarding the separated shear layer, it is first inclined upwards at the separation point, after which it is again deflected towards the wall by the action of the expansion fan. The latter originates at the impingement point of the incident shock on the sonic line. The consequent reattachment of the shear layer again induces the formation of compression waves, which can coalesce into a reattachment shock. The results of this entire viscous interaction is a spreading of the shock-system static pressure-jump, as illustrated in Fig. 3.2.

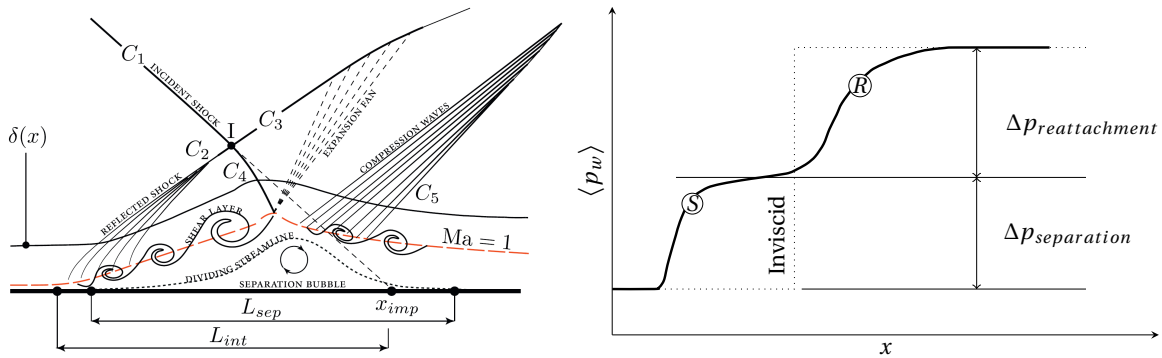


Figure 3.2: Sketch of a typical strong Shock/Wave-Turbulent Boundary-Layer Interaction (left, [Pasquariello et al., 2015]) and the accompanying mean wall pressure distribution (right, adapted from [Délery and Dussauge, 2009])

### 3.2.1. Low Frequency Unsteadiness

From an unsteady point of view, SWTBLI's are much more complex. As stated earlier, SWTBLI with mean separation inherently shows significant low-frequency movement of the separation shock. The dominant frequency of this unsteady motion is typically two or more orders of magnitude lower than the characteristic frequency of the energetic eddies in the incoming boundary layer,  $U_{ref}/\delta_{ref}$ . Over the last decades, a multitude of different explanations for this phenomenon has been postulated. Typically, the shock is seen as a boundary between upstream and downstream conditions, thus the shock motion can be attributed to either downstream or upstream mechanisms. The current consensus seems to move towards an intrinsic mechanism though, driven by a certain forcing originating upstream. A short overview will be given here, while the reader is referred to the work by Clemens and Narayanaswamy [2014] for a more in depth study.

First, **intrinsic mechanisms** are considered. Toubert and Sandham [2011] derived an ODE for reflected shock motion, based on the Navier-Stokes momentum equation and SWTBLI LES results. Mathematically speaking, the results had the characteristics of a low-pass filter, which is similar to what was postulated by Plotkin [1975] and later by Grilli et al. [2012]. The authors argued that shock motion should not necessarily be attributed to up- or downstream mechanism, but that it is in fact an intrinsic property of the coupled system. Note that the model by Toubert and Sandham [2011] was recently modified by Brouwer et al. [2017] to include the effect

of surface deformation. Based on unprecedented well-resolved long-integration time LES data, Pasquariello et al. [2017] found strong support for the intrinsic behaviour of the interaction. It is argued that the mechanism might not be self-sustaining, requiring a certain forcing originating upstream or in the interaction zone itself. A possible continuous coherent forcing could be the observed unsteady Görtler-like vortices, which were linked to streamwise-elongated regions of low and high momentum. A similar explanation was postulated independently by Priebe et al. [2016], increasing the confidence in this result.

An actual **upstream mechanism** was first proposed by Andreopoulos and Muck [1987], who determined the mean shock-crossing time period from wall-pressure measurements under a Mach 3 compression ramp. According to Dolling and Brusniak [1989] though, the measurements executed by Andreopoulos and Muck [1987] were susceptible to a misinterpretation of turbulent motions as a crossing of the shock. A similar relation between upstream pressure fluctuations and shock-foot motion was observed by Erengil and Dolling [1993]. However, they observed correlations between the pressure under the separated flow region and the intermittent region over which the separation shock translates, which led to the belief that the low-frequency shock motion was caused by breathing of the separation bubble. Another possible explanation is the occurrence of long low-velocity superstructures in the turbulent boundary layer. Ganapathisubramani et al. [2009] observed a strong correlation between structures of up to  $40 \delta_{ref}$  length and the instantaneous position of a separation line surrogate. This correlation was not observed by Wu and Martín [2008] though, who used the true separation point instead of a surrogate model. Détery and Dussauge [2009] also argued that the frequency of such long structures is too low to explain the typical unsteadiness of oblique shock reflections, which was confirmed by Toubert and Sandham [2009]. Even more, the LES results obtained by Pasquariello et al. [2017] did not show any evidence for coherent structures of sufficient length. The effect of these superstructures was also investigated in Delft by Humble et al. [2009], who found them to be the cause of high-frequency small-amplitude spanwise wrinkling of the shock.

Although many plausible upstream mechanisms exist, several authors have observed more prominent **downstream mechanisms**. These usually link the motion of the separation shock to the behaviour of the downstream separation bubble. Dolling and Erengil [1991], Thomas et al. [1994] and Dupont et al. [2006] all showed that the wall-pressure fluctuations close to the reflected shock foot and near the reattachment point are correlated at low frequencies. A phase shift is observed, which indicates a breathing motion of the separation bubble, i.e. a periodic expansion and contraction. Piponniau et al. [2009] and Wu and Martín [2008] proposed a simple model based on shear layer entrainment of the low-momentum fluid in the separation bubble. It was argued that the reduction in bubble mass due to this entrainment process (breathing) could be compensated by large-scale transverse motions (flapping) of the shear layer near the reattachment point. For strong shocks, the consensus seems to be that shock motion will be caused by this flapping motion at the reattachment point. Pirozzoli and Grasso [2006] simulated a Mach 2.25 SWTBLI with DNS, which was too short to capture the low-frequency unsteadiness. However, they observed evidence for an acoustic feedback mechanism between the incident shock and the upstream separation point, which would act at higher frequencies than the typical low-frequency motion. Using LES, it was shown by Toubert and Sandham [2009] that acoustic waves can indeed travel upstream within the separation bubble.

### 3.2.2. Interaction Length

Based on literature, three different parameters were found to affect the extent of the separated region observed for strong SWBLI. The correlation between the relative positioning of the wedge trailing edge w.r.t. the shock impingement point and the interaction length is first discussed, after which the effect of Reynolds number is touched upon. Lastly, the effect of panel unsteadiness on the interaction length is elaborated on.

#### Effect of the Wedge Trailing Edge Expansion Fan

An important aspect which should be taken into account when considering the generation of an oblique impinging shock in an experimental facility, is the Prandtl Meyer Expansion (PME) fan inevitably originating at the trailing edge of the shock generator. Depending on the wedge geometry, the expansion fan can interact with the impinging/reflected shock system and affect the SWBLI accordingly. For  $M_1 = 2.0$  and  $\vartheta_1 = 10^\circ$  ( $p_3/p_1 \approx 2.8$ ), Threadgill and Bruce [2017] experimentally observed an interaction length of  $6 \delta_{ref}$ , compared to about  $10 \delta_{ref}$  computed by Matheis and Hickel [2015] ( $Re_{\delta_{ref}} = 48.3 \cdot 10^3$ ). This can most likely be attributed to the different positions of the trailing edge expansion relative to the interaction. Indeed, Grossman

and Bruce [2018] found experimentally that moving the impingement point of the first expansion wave closer to the interaction will reduce the separation extent by moving the separation point downstream, while the reattachment point remains more or less constant. This can be attributed to a stronger pressure rise being required at the reattachment point, thus necessitating a longer separation bubble to provide the required momentum exchange between the freestream and the separated shear layer to ensure reattachment [D elery and Dussauge, 2009]. The distance between the inviscid shock impingement point and the impingement point of the first expansion fan wave  $L$ , illustrated in Fig. 7.2, can thus be identified as a key parameter affecting the interaction length of a SWBLI. The general structure of the interaction was found to be independent of the PME fan distance though. For the most downstream location of the wedge trailing edge, a separation length of about  $12\delta_{ref}$  was observed for a flow deflection angle of  $12^\circ$ . Similar results were obtained in the experiments conducted by Rabey and Bruce [2019] ( $M_1 = 2.0$ ,  $\vartheta = 12^\circ$ ), where the interaction length was found to increase from  $7.2\delta_{ref}$  to  $13.5\delta_{ref}$  by moving the expansion fan more downstream. An alternative parameter to characterise the distance between shock and expansion fan is the channel height to wedge width ratio  $g^+ = g/w$ , as employed for example by Matheis and Hickel [2015].

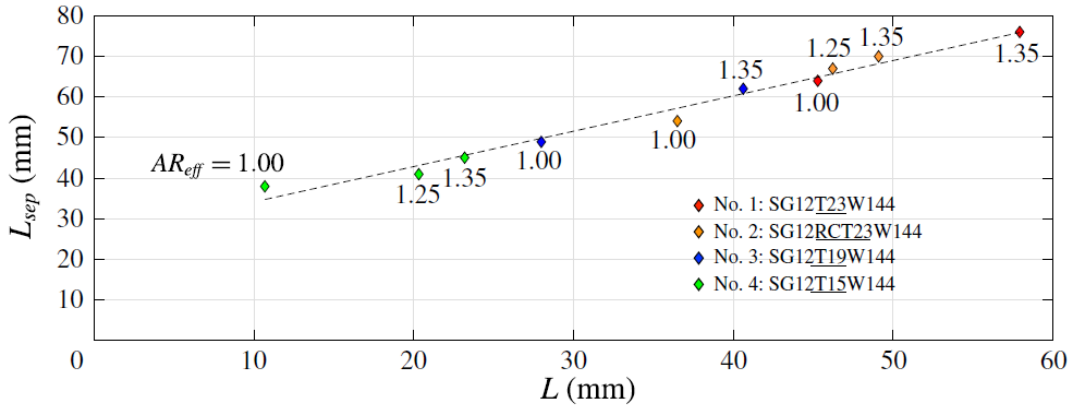


Figure 3.3: Correlation between expansion fan impingement separation  $L$  and separation extent  $L_{sep}$  [Grossman and Bruce, 2018]

Considering the correlation between expansion fan - impinging shock distance and the interaction length, Grossman and Bruce [2018] found that a nearly linear correlation exists up to their maximal attainable expansion fan-SWBLI distance, as shown in Fig. 3.3. A further increase in distance was not possible due to the sudden appearance of a normal shock at the wedge tip, causing a tunnel unstart. According to Li and Ben-Dor [1997], this can occur when a Mach reflection is theoretically possible, but cannot be established due to the reflected incident shock impinging on the wedge, upstream of the expansion fan origin. This can be attributed to the shock reflecting from the wedge onto the subsonic slipstream caused by the Mach reflection, rendering it unstable and thus inducing an upstream push of the Mach stem. Indeed, Matheis and Hickel [2015] observed a pocket of subsonic flow behind the interaction at the given flow deflection angle, indicating the onset of an irregular SWBLI (ISWBLI). The author argues that for a regular SWBLI, thus at a smaller flow deflection angle than approx. 12 degrees, this choking of the tunnel will not occur when the reflected impinging shock does not interact directly with the expansion fan.

Thus, the pressure rise at reattachment and the extent of the separated region strongly depend on the location of the PME fan originating at the shock-generator trailing edge, and care must therefore be taken to ensure simulation and experiment do not differ in this respect.

### Effect of Reynolds Number

The effect of the Reynolds number  $Re_\delta = U_1\delta/\nu_1$  is twofold. For laminar interactions and turbulent interactions at low Reynolds number ( $Re_\delta < 10^5$ ), an increase in Reynolds number will lead to a growth of the interaction length [Babinsky, 2011]. This can be attributed to the decrease in skin friction, which is illustrated for laminar and turbulent boundary layers in Fig. 3.4(a) and Fig. 3.4(b) respectively. This leads to a reduction of the separation pressure jump predicted by the free-interaction theory [Chapman et al., 1957] and as a result, a stronger pressure rise is required at reattachment. Thus, as discussed earlier, the separation point has to move upstream to accommodate a longer separated shear layer which ensures enough momentum

can be transferred from the freestream to the boundary layer. For high Reynolds number turbulent interactions ( $Re_\delta \geq 10^5$ ), the increased boundary layer momentum will outweigh the reduction in  $C_f$ , leading to a reduction in separation extent.

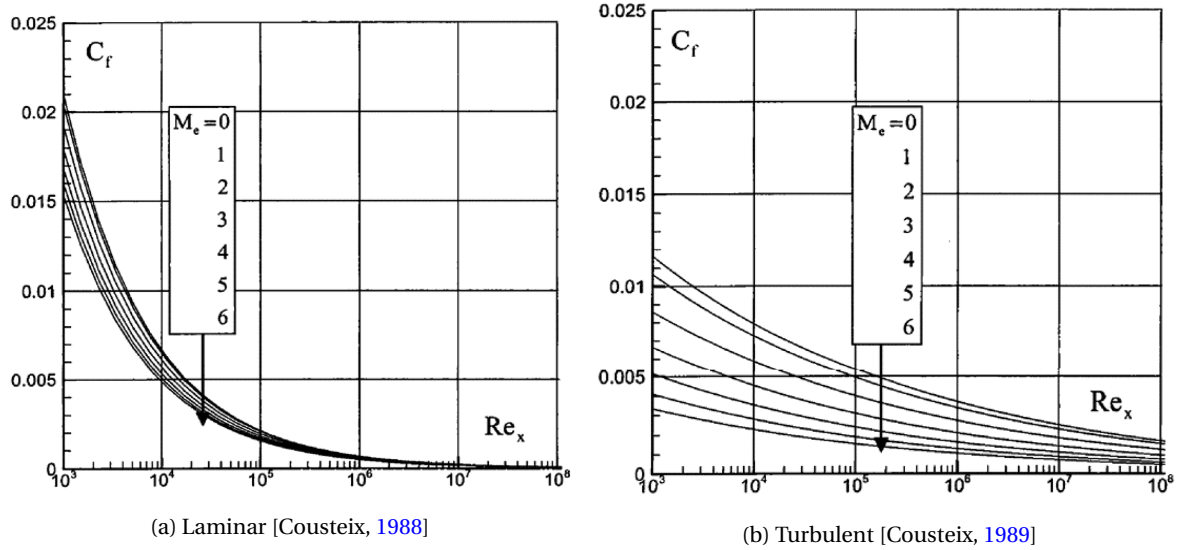


Figure 3.4: Skin friction coefficient versus  $Re_x$  for different Mach numbers for a laminar and a turbulent flat-plate boundary layer

### Effect of Panel Unsteadiness

Panel unsteadiness can significantly affect the extent of the separation bubble. Visbal [2014] investigated the interaction between a simply supported panel and a laminar SWBLI with unsteady RANS and observed a streamwise shrinking of the mean separation bubble by 31%, as illustrated in Fig. 3.5. Pasquariello et al. [2015] also observed a reduction in the separation extent of about 15% compared to the SWTBLI over a rigid flat plate, but no conclusion could be drawn from this result since a weaker shock was considered for the coupled interaction. Brouwer et al. [2017] investigated the effect of surface curvature and unsteady deformation on SWTBLI using a RANS approach. It was found that the behaviour of the separation bubble depends strongly on the plate curvature at the separated region, yielding a minimal reduction in the separation extent for midpoint shock impingement on plates undergoing a second mode deformation (or any other even mode). Indeed, for such motion, the separation bubble is located at an inflexion point, yielding negligible surface curvature underneath the separated region. It must be noted that the separation bubble considered by Brouwer et al. [2017] only spanned about 20% of the panel length in the rigid case.

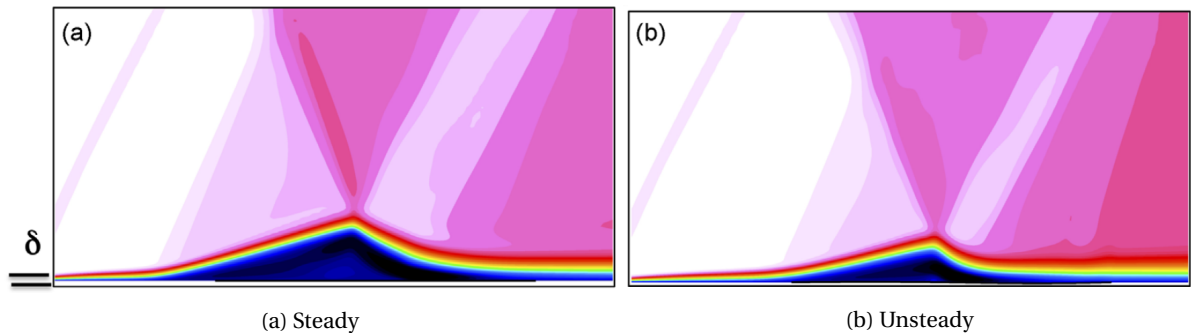


Figure 3.5: Mean streamwise velocity contours for a laminar interaction over a rigid (a) and flexible (b) panel ( $M_1 = 2.0$ ,  $p_3/p_1 = 1.8$ ,  $k = 0.50$ ,  $Re_a = 120,000$ ).

### 3.2.3. Numerical Simulation of SWBLI

The main difficulty in the investigation of coupled SWTBLI lies in the computational cost. In most applications, turbulent flows at high Reynolds number are involved. Since the ratio of smallest to largest scales in 3D problems increases with  $Re^{9/4}$ , resolving all scales in high Reynolds number flows becomes an infeasible task. Two main alternatives exist: Reynolds-Averaged Navier Stokes (RANS) simulations, which model all turbulent scales, or Large-Eddy Simulations (LES), which resolve the most energetic turbulent eddies and model the remaining subgrid scales. It has been clear for many years that LES approaches are required to resolve SWTBLI [Knight and Degrez, 1998]. This requirement stems mainly from the fact that only LES can capture the inherent low-frequency unsteadiness. Indeed, it was found by Knight et al. [2003] that LES produces improved results for both two- and three-dimensional interactions. Morgan et al. [2013] investigated modelling errors of eddy-viscosity and Reynolds-stress-transport RANS approaches. By comparing the RANS results for SWBLI at different shock strengths and Reynolds numbers with an LES-based surrogate model, they observed a strong overestimation of the separation length. A similar error was found by Pirozzoli et al. [2009], which was attributed to the inability of RANS models to predict turbulent transport within the detached shear layer. Next to that, the RANS approaches failed to predict the anisotropic behaviour of turbulence close to the separation point, missing a dominant near-wall one-component turbulence state which in the LES case lifts up the shear layer.

Weak interactions have been thoroughly investigated with DNS [Pirozzoli and Grasso, 2006; Priebe et al., 2009] and LES [Agostini et al., 2012; Aubard et al., 2013; Hadjadj, 2012; Nichols et al., 2016; Pasquariello et al., 2014; Pirozzoli et al., 2010; Toubert and Sandham, 2009], but only low Reynolds numbers ( $Re_{\delta_0} \leq 60 \cdot 10^3$ ) and short integration times were considered. Since it has been shown that the transition to strong interactions can already happen at low shock strength, and that increasing the shock strengths will lead to more intense low-frequency content at increased time-scales [Morgan et al., 2013], it is clear that high Reynolds LES approaches of strong interactions over long integration times are required.

The first well-resolved LES at high Reynolds number ( $Re_{\delta,ref} = 205 \cdot 10^3$ ) was conducted by Pasquariello et al. [2015]. The interaction between a turbulent boundary layer and an oblique shock generated by a wedge creating a flow deflection angle  $\vartheta$  of  $20^\circ$  was simulated over a timespan of  $1900\delta_{ref}/U_\infty$ . This is the numerical counterpart of the experiment conducted by Daub et al. [2015b], and excellent agreement between both set-ups was obtained. The evolution of the mean wall-pressure was reproduced nicely, while the pressure plateau under the separation bubble also showed excellent agreement with the experiment. Significant unsteady motion of the shock foot was obtained in the LES, but it was not possible to validate this due to the absence of a pressure sensor at the mean separation point in the experiment. The same experimental set-up was again reproduced numerically by Pasquariello et al. [2017] two years later, but the integration time of the LES was doubled to  $3805\delta_{ref}/U_\infty$ . This allowed for a more accurate study of the low-frequency unsteadiness. An in-depth analysis of the filtered 3D flowfield showed the development of counter-rotating Görtler-like vortices downstream of the bubble apex, which were found to not be restricted to a certain spanwise location. Instead, a slow meandering motion of the vortices was observed, in contrast to the results by Loginov et al. [2006], which was found to be coupled to separation bubble breathing. Two dominant modes were identified by using sparsity-promoting dynamic mode decomposition. First of all, the typical low-frequency mode ( $St = 0.04$ ) corresponding to a breathing motion of the separation bubble and the accompanying shock-foot motion was observed. Secondly, a medium-frequency mode ( $St = 0.5$ ) was also identified, which was related to a downstream convection of shear-layer vortices, which also induced the formation of Mach waves. This led to a corrugation (wavelike motion) of both the reflected and reattachment shock. Lastly, the Görtler-like vortices were found to cause a large-scale flapping of the reattachment line, in addition to the breathing motion of the separated flow region.

### 3.2.4. Coupled SWBLI over a Compliant Panel

SWBLI over a flexible panel has been mainly investigated with RANS approaches, which fail in predicting the inherent low-frequency content of the interaction. Nevertheless, these results can give an insight in the qualitative mean-flow behaviour. Miller et al. [2012] first investigated the response of a 2D flexible panel to a Mach 3.0 SWTBLI ( $Re_a = 7.4 \cdot 10^5$ ) using RANS, and a dependency of the panel motion on back pressure and dynamic movement of the impingement point was found. Visbal [2014] and Boyer et al. [2016] also used RANS approaches to investigate the coupling between a Mach 2.0 laminar SWBLI ( $Re_a = 1.2 \cdot 10^5$ ,  $p_3/p_1 = 1.8$ ) and a 2D compliant panel (thickness-to-length ratio  $h/a = 0.002$ ). Note that the shock was strong enough to induce mean boundary layer separation. Compared to the inviscid results, significantly more complex

response was observed, which involved a long LCO-like transient, followed by chaotic high-mode motion. A strong variety in active modes with varying shock strength was found, which could be attributed to Tollmien-Schlichting waves coupling with high structural modes for low shock strengths ( $p_3/p_1 = 1.4$ ). No monotonic behaviour with increasing nondimensional dynamic pressure  $\lambda^*$  was obtained either, where the latter is a typical nondimensional parameter employed to characterise flutter and is given by Eq. (3.4). A pressure ratio of  $p_3/p_1 = 1.8$  resulted in increasing transient durations with increasing  $\lambda^*$ , and a complete elimination of all unsteadiness for  $\lambda^*$  exceeding 1,250. Considering the mean deformation, a second mode deformation was observed, which was similar in shape to the inviscid case but one order of magnitude smaller. The mean flow was also altered: a reduction in separation extent was obtained, which could be attributed to the forcing of the flow by the unsteady panel motion, as was proven recently by Brouwer et al. [2017]. This was already elaborated on in Section 3.2.2.

Gogulapati et al. [2015] developed a FSI tool to analyse the coupled flow-structural response of thin panels. The steady surface pressure was obtained with a surrogate RANS model, while pressure fluctuations were estimated with local piston theory. A similar low-cost LPT prediction of the unsteady loads was utilised by Brouwer et al. [2015] for inviscid shock-flexible panel interactions, which yielded flutter boundaries which were close to those obtained by Visbal [2014]. Gogulapati et al. [2015] estimated turbulent boundary layer loads with a semi-empirical model. The fluid model was coupled explicitly to a FEM-based structural solver, and results were compared with experimental Mach 2.0 results obtained in the AFRL RC-19 facility for panels clamped at all edges [Beborniss et al., 2011, 2012; Spottswood et al., 2012, 2013]. Significant discrepancies were observed in the dynamic response, which were later found to be attributable to the thermal boundary conditions and shock unsteadiness [Gogulapati et al., 2015]. The mean displacement and dominant frequency observed in the experiment by Spottswood et al. [2012, 2013] were also obtained by the Delayed Detached Eddy Simulation (DDES) of Gan and Zha [2016].

The only well-resolved LES of coupled SWTBLI is the simulation carried out by Pasquariello et al. [2015], who loosely coupled implicit LES (iLES) to a FEM discretisation of a hyperelastic Saint Venant-Kirchhoff material model. A Mach 3.0 interaction of a sweeping shock with a TBL at a high Reynolds number of  $Re_\delta = 205 \cdot 10^3$  over a compliant Spring steel CK-75 panel was investigated. The shock was generated by wedge rotating from  $\langle \vartheta \rangle = 0^\circ$  to  $\langle \vartheta \rangle = 17^\circ$ , which is similar to (a part of) the experiment conducted by Daub et al. [2015b]. The final shock impingement location was  $k = 0.36$ , and the cavity pressure was set to the freestream static pressure. This makes it impossible to compare the results to the the work by Visbal [2012, 2014] and Boyer et al. [2016, 2018], who employ a cavity pressure given by Eq. (3.1). Secondly, a damped LCO-like motion was observed in the windtunnel, which was not obtained in the experiment. The reasons for this discrepancy were elaborated on in Chapter 1. Next to the mismatch between experiment and simulation regarding unsteady motion, it must be noted that the mean panel deformation was in excellent agreement with the experiment, although overall deflections were small due to the high stiffness of the plate material. It can thus be concluded that the coupling algorithm is robust, but that too much uncertainty was introduced by the boundary conditions.

Recently, the interaction between a compliant panel and a Mach 1.4 normal shock was investigated experimentally by Jinks et al. [2016]. The panel side-edges were free, ensuring unrestricted spanwise movement of the structure. A cavity pressure equal to more or less the average upper surface pressure was obtained, but strong fluctuations related to shock motion were observed. It must be noted that the steady deflection of the panel was large (on the order of 10 times the panel thickness), therefore the author argues that in the case of an oblique shock, static deflections and therefore pressure fluctuations will be much smaller.

### 3.3. Governing Parameters

The interaction between a plate and a supersonic flow is complex and is governed by a multitude of parameters. In order to identify a testcase with strong unsteady behaviour, it is crucial to first determine which parameters should be considered. In this section, based on a thorough literature study, the nondimensional parameters that govern the flutter behaviour will be introduced. Note that the majority has been defined in the context of classical panel flutter, i.e. without shock impingement, since it is a much more mature field. First, the governing structural parameters are listed in Section 3.3.1. Next, the dominant flow parameters are summarised in Section 3.3.2, after which the effect of boundary conditions and initial conditions is touched upon in Section 3.3.3. Lastly, additional factors affecting the flutter behaviour are elaborated on in Section 3.3.4.

### 3.3.1. Structural Parameters

**Dynamic pressure  $\lambda$ :** The nondimensional dynamic pressure is a dominant structural parameter for classical panel flutter, and has thus been adapted as such in recent shock-panel interaction investigations [Boyer et al., 2016, 2018; Visbal, 2012, 2014]. It is given by Eq. (3.4), where  $D$  is the flexural rigidity of the plate, and removes the dependency of classical panel flutter on the panel thickness to length ratio  $h/a$  and the material properties  $E_s$  and  $\nu_s$ . Multiple definitions of the nondimensional dynamic pressure exist, depending on which form of linear aerodynamic theory (piston theory) lies at the basis. For clarity,  $\lambda$  is used if  $f(M) = \beta$  [Hedgepeth, 1957], while the notation  $\lambda^*$  is employed if  $f(M) = 1$  [Visbal, 2012, 2014]. Another option is  $f(M) = M$  [Lighthill, 1953], but this is not frequently employed in recent work.

$$\lambda = \frac{\rho_\infty U_\infty^2 a^3}{f(M)D} \quad (3.3)$$

$$= 2 \frac{q_\infty}{f(M)} \left(\frac{a}{h}\right)^3 \frac{12(1-\nu_s^2)}{E_s} \quad (3.4)$$

$$D = \frac{E_s h^3}{12(1-\nu_s^2)} \quad (3.5)$$

The nondimensional dynamic pressure determines first of all whether the plate is stable or not. Secondly, once the point of instability has been passed, the amplitude of the oscillation usually increases with increasing  $\lambda$ . It is safe to assume this will always occur for inviscid interactions, while for viscous panel flutter with shock impingement more care must be taken. As mentioned earlier, Visbal [2014] and Boyer et al. [2016] both observed an increase in flutter amplitude and a reduction in size of the separation bubble with increasing  $\lambda$ , up to the point that a steady solution suddenly emerged at  $\lambda \geq 1,250$ . Note that this only occurred for relatively strong shocks ( $p_3/p_1 \geq 1.8$ ). It is assumed this can be attributed to the increased mean panel deformation with increasing dynamic pressure, which introduces additional stiffness to the system. To the author's knowledge, for a turbulent SWBLI, no parametric study of flutter behaviour with increasing  $\lambda$  has been performed yet.

Note that in the case of an impinging shock, the author argues that  $\lambda$  does not completely include the effect of  $h/a$ . Large deflections are involved, which depend strongly on the panel thickness. Since the panel steady and unsteady deformations will nonlinearly alter the flowfield, it is very possible that for different  $h/a$ , different nondimensional dynamic flutter pressures will be obtained.

**Length-to-width ratio  $a/b$ :** The panel length-to-width ratio determines the three-dimensionality of the problem. If  $a/b = 0$ , an infinitely wide panel or 2D problem is obtained, which has been investigated extensively for classical inviscid panel flutter. It is therefore well understood for both transonic and high supersonic Mach numbers. If  $a/b$  is increased for panels constrained at all edges (simply supported or clamped), an increase in flutter dynamic pressure is observed [Dowell, 1966, 1967; Laurenson and McPherson, 1977]. This can be attributed to an increased spanwise constraint resulting in an increased panel stiffness. Prediction of eigenfrequencies for panels constrained in the streamwise direction but unconstrained in spanwise direction is rather complicated, and for more information the reader is referred to Leissa [1969]. It can be expected though that assuming the streamwise edges are free will result in a reduced stiffness compared to the fully clamped/pinned case. Considering the 3D flutter behaviour of panels constrained at all edges, results can be expected to be qualitatively similar to the 2D case for  $a/b$  up to 2.0 [Dowell, 1966; Visbal, 2014].

Increasing the panel slenderness will not only affect the geometrical stiffness of the structure though. If a shock impinges on the panel, constrained edge conditions will induce spanwise bending of the shock, significantly changing the aerodynamic loading and introducing a dominant spanwise mode into the flutter motion [Boyer et al., 2018]. Secondly, the supercritical instability observed for high shock strengths and 2D panels by Visbal [2014] is not observed for a 3D panel in the same flow conditions. Boyer et al. [2018] argues the increased stiffness of the panel postpones this phenomenon to higher shock strengths, although this still has to be confirmed.

Considering 3D viscous panel flutter with and without shock impingement, very few publications are available. To the author's knowledge, no publications on high supersonic Mach number classical viscous flutter exist, but it is argued that the difference with 2D results will be small if there are no spanwise panel constraints. Daub et al. [2015b] and Pasquariello et al. [2015] obtained semi-2D results for a clamped-free panel subject to a fast-sweeping impinging shock. It is argued that for a viscous-inviscid interaction, panels

constrained at all edges will lead to a significant increase in complexity [Boyer et al., 2016].

The **air/plate mass ratio**  $\mathcal{M}$ , which is usually defined as  $\mathcal{M} = (\rho_1 a)/(\rho_s h)$ , is a typical governing parameter. Since higher values increase the relative importance of aerodynamic forces, a higher flutter dynamic pressure is expected. Flutter behaviour is in general only weakly dependent on its value though. It was shown by Dowell [1967] that increasing  $\mathcal{M}$  from 0.01 to 0.1 has no significant effect on the flutter behaviour of low  $a/b$  plates at high supersonic  $M$ . Only if frequencies are high or if single-mode flutter is considered,  $\mathcal{M}$  might significantly affect the results [Dowell, 1970]. For typical aerospace applications,  $\mathcal{M} = 0.1$  is generally employed [Boyer et al., 2016, 2018; Dowell, 1967, 1970; Gordnier and Visbal, 2002; Visbal, 2012, 2014].

**Plate thickness  $h/a$ :** As mentioned in the discussion of the nondimensional dynamic pressure, the thickness to length ratio of the plate could nonlinearly affect the flutter behaviour in the case of shock impingement, making it an extra nondimensional governing parameter. This has never been verified though, and could be interesting for further analysis. The introduction of  $h/a$  as an extra parameter becomes clear when examining the equations of motion of a plate subject to a static loading difference, as will be elaborated on in Chapter 4.

**Shock impingement location  $k$ :** The impingement point on the panel has a significant and quite complex effect on panel dynamics. Note that the impingement point can only be accurately defined in the inviscid rigid case, since 1) panel deflection will induce compression/expansion waves which can bend the incident shock, 2) strong panel deformation can induce a leading edge shock which will lead to shock-shock interference, 3) the viscous boundary layer will tend to spread the pressure jump and induce complex shock-shock interaction and unsteady movement of the shock (see also Section 3.2) and 4) vertical movement of the panel can slightly alter the impingement location.

In most publications involving inviscid fluid models, the shock is assumed to impinge on the panel midpoint [Boyer et al., 2016, 2018; Visbal, 2012, 2014]. On the other hand, high fidelity analyses [Gogulapati et al., 2014, 2015; Pasquariello et al., 2015] with the goal of replicating wind tunnel experiment [Daub et al., 2015b; Spottswood et al., 2013] involve more upstream shock impingement, since it was observed experimentally that it triggers an increased instability of the panel. Indeed, a reduction in flutter dynamic pressure was observed by Visbal [2014] and Ye and Ye [2018] for  $k < 0.5$ . On the other hand, Visbal [2014] observed ceasing of the dynamic instability for  $k = 0.38$ , which is close to the impingement point for which Pasquariello et al. [2015] observed a LCO.

As will be discussed in Chapter 4, forward movement of the impingement point will result in a forward movement and reduction of the upward mean deflection, and a strong increase in post-shock downward deflection. This can be attributed to the behaviour of the prescribed average cavity pressure, since it increases with upstream movement of the shock foot.

For viscous interactions, the **distance between shock and expansion fan impingement  $L$**  strongly affects the extent of the separated region in strong SWBLI. This was elaborated on in Section 3.2.2. For inviscid shock-panel interactions, the shock-generator PME fan affects the shock system in a much more direct way, i.e. by bending the reflected and/or impinging shock, depending on the relative positioning of the wedge trailing edge.

### 3.3.2. Aerodynamic Parameters

**Mach number  $M$ :** The Mach number strongly affects the flutter behaviour. Without shock impingement, single-mode flutter will occur for Mach numbers in the transonic regime, while coupled-mode flutter occurs for high supersonic  $M$ . The Mach number thus first of all determines the aerodynamic model that can be applied. For inviscid flow, it can be concluded that if  $M \geq 1.7$ , single-mode flutter will not be possible. Fully linear aerodynamic theory can therefore be safely applied to determine the classical flutter boundary, yielding the same flutter boundaries as nonlinear aerodynamic models. Considering higher fidelity inviscid calculations, the Euler equations will yield an increased flutter dynamic pressure compared to quasi steady models due to the inclusion of flow memory [Mei et al., 2014]. Next to that, the semi-empirical inviscid panel design method presented by Laurensen and McPherson [1977] provides flutter boundaries that are in excellent agreement with Euler results for  $M \geq 2$ . Secondly, increasing the Mach number will increase the flutter dynamic pressure and reduce flutter amplitude and frequency [Dowell and Voss, 1965; Gordnier and Visbal, 2002]. This effect also persists when a shock impinges on the panel [Boyer et al., 2018; Visbal, 2014]. When viscous flow is considered, the Mach number influence becomes more complex. In the transonic regime, the

boundary layer has a stabilising effect, i.e. the flutter boundary shifts to a higher dynamic pressure and the flutter amplitude is decreased [Gordnier and Visbal, 2002; Muhlstein et al., 1968]. This effect peaks around  $M = 1.2$  and decreases significantly up to  $M = 1.4$ . For higher Mach numbers, the boundary layer becomes destabilising. This effect persists up to  $M = 1.6$  according to Alder [2015], and up to  $M = 1.8$  according to Hashimoto et al. [2009]. Around  $M = 2$ , the difference between the viscous and inviscid flutter boundaries is negligible, while increasing the Mach number even further will once again lead to a stabilising effect of the boundary layer [Hashimoto et al., 2009].

With inviscid shock impingement, the effect of increasing the Mach number boils down to an increase in LCO frequency, a reduction in LCO amplitude and a shift of the flutter boundary to higher nondimensional dynamic pressures [Visbal, 2014].

**Shock strength  $p_3/p_1$ :** The strength of the shock, for a given Mach number  $M$ , can be represented by the theoretical pressure jump over the inviscid regular reflection. It can also be given by the shock angle  $\sigma$  or the flow deflection angle  $\vartheta$ . As will be addressed in Chapter 4, the shock strength strongly affects the nature of the panel instability in the inviscid case. This is also strongly coupled to the cavity pressure and the dimensionality of the problem. For a cavity pressure equalling the average of the pre-and post-shock system static pressures, sub or supercritical bifurcation behaviour can be observed depending on the shock strength, as elaborated on in Section 3.1. If the cavity pressure is not set to the average inviscid reflection pressure, Visbal [2014] observed steady deflection solutions for a shock strength of  $p_3/p_1 = 1.4$ . Unstable behaviour of clamped panels with different cavity pressures was observed experimentally by Spottswood et al. [2013] and Daub et al. [2015b] though, but (much) higher shock strengths of 2.3 and 8.36 were imposed. Next to that, inviscid shock impingement locations were close to the 1/3rd panel chord point, while it is also not clear if Spottswood et al. [2013] obtained undamped flutter behaviour. Lastly, it can be stated that in the case of  $p_c = 0.5(p_1 + p_3)$ , increasing the shock strength will increase the asymmetry of the problem, which will increase the importance of asymmetric modes in the flutter motion [Boyer et al., 2018].

Considering viscous flutter, a strong dependence on shock strength was found by Boyer et al. [2016] for the interaction between a laminar boundary layer and a compliant panel subject to an impinging shock, as discussed in Section 3.2.4. Moreover, as discussed in Section 3.2.2, an increase in impinging shock strength will require the pressure jump at reattachment to increase, thus necessitating a longer separated shear layer to transfer the required momentum from the freestream. This leads to an upstream movement of the separation point.

**Cavity pressure  $p_c/p_1$ :** The pressure on the lower side of the panel strongly affects the static panel deformation, while it can also be hard to control experimentally. It is usually nondimensionalised with the freestream static pressure  $p_1$ . In the case of classical panel flutter, steady pressure differences are usually small, but if present, they can strongly increase the stiffness of the panel [Dowell, 1966]. In the case of a flat panel, prescribing the freestream pressure on the bottom of the panel allows an excellent quantification of the dynamic behaviour of the panel [Gordnier and Visbal, 2002].

The cavity pressure becomes a much more dominant parameter when a shock impinges on the panel, since this always creates different steady pressure ratio's over the pre-and post-shock sections of the plate. Completely neglecting these transverse loads and the consequent mean plate deformation, as attempted analytically by Ye et al. [2018] and Ye and Ye [2018], results in flutter behaviour which differs strongly from the more physical uniform cavity pressure. The shortcomings of such linear models are extensively elaborated on in Chapter 4. A "minimal" influence of the static pressure is obtained when the average of the theoretical pressure jump over the inviscid regular reflection is prescribed in the cavity, as given by Eq. (3.1) [Boyer et al., 2016, 2018; Visbal, 2012, 2014]. This results in steady second mode deformations. This boundary condition is not often obtained in windtunnel testing, since usually pressure equalisation between the cavity and upstream [Daub et al., 2015b; Pasquariello et al., 2015] or downstream [Gogulapati et al., 2014; Spottswood et al., 2013] conditions is ensured. Cavity pressures lower or higher than the theoretical average pressure over the flowside were investigated by Visbal [2014], and were found to yield steady deformed solutions for a shock strength of  $p_3/p_1 = 1.4$  and  $\lambda^* = 875$ . Pasquariello et al. [2015] and Spottswood et al. [2013] did observe flutter for the given cavity pressures, but the discrepancy can perhaps be attributed to the following reasons. The first case involved a fast and very strong shock sweep, which could incite the observed (non LCO-like) panel motion, while for the latter is unclear what the actual cavity pressure was. In both cases, a shock impingement point closer to the leading edge was selected ( $k = 0.33$  [Pasquariello et al., 2015] and  $k = 0.36$  [Gogulapati et al., 2014]), which leads to more unstable panel behaviour.

Considering obtaining the average theoretical upper surface pressure in the cavity, three options arise. First of all, clamping of the plate at all edges would allow pressurisation of the test section. Three-dimensional flutter of a 3D edge-restrained panel subject to an impinging shock produces strong spanwise flow variation though, and introduces a dominant spanwise mode into the unsteady motion of the plate [Boyer et al., 2018] (see previous section). A second option to approach an averaged pressure on the bottom of the plate would be to allow flow between the panel edges and the cavity, as done for example by Jinks et al. [2016]. This most likely results in the lowest net static pressure difference over the plate, but  $p_c$  was found to be significantly unsteady and dependent on shock location. The experiment by Jinks et al. [2016] considered a normal shock and a shallow cavity though, which leads to a very strong pressure jump and the compressed air in the cavity acting as an aerodynamic spring [Dowell and Voss, 1965]. Considering the cavity depth of the ST-15, pressure fluctuations are expected to be much smaller. Another benefit of leaving the spanwise edges unrestrained, is that semi 2D behaviour of the panel and the flow can be expected. The third and last option entails sealing of the cavity by adding a thick layer of soft foam rubber to the underside of the panel, as attempted by Daub et al. [2015b]. This could add significant damping to the system though, and it is not clear how this can be modelled numerically [Pasquariello et al., 2015]. Leaving spanwise gaps between the compliant plate and the test section thus seems to be the best option for obtaining an averaged cavity pressure through pressure equalisation.

**Reynolds number  $Re$ :** In literature on viscous panel flutter, different Reynolds numbers are employed. For laminar flows, the panel Reynolds number  $Re_a$ , based on the panel length  $a$ , is often used, while turbulent boundary layers are characterised by  $Re_\delta$ , based on the boundary layer thickness. To the authors knowledge, a sensitivity study of the interaction of an impinging shock with a compliant panel with respect to Reynolds number has only been done for a laminar boundary layer [Visbal, 2014]. A doubling in Reynolds number from  $Re_a = 1.2 \cdot 10^5$  to  $Re_a = 2.4 \cdot 10^5$  resulted in increased pressure fluctuations and a halving of the extent of the separation region. This might be attributed to the increased forcing of the boundary layer. As discussed in Section 3.2.2, the Reynolds number indeed has a strong influence on the interaction length, which is twofold for turbulent SWBLI depending on whether  $Re_\delta$  exceeds  $1 \times 10^5$  or not.

**Boundary layer thickness  $\delta/a$ :** For classical panel flutter, an increase in the boundary layer thickness results in a linear increase of the flutter dynamic pressure, as well as a reduction in growth of both the amplitude and frequency of the flutter response, as long as  $\delta/a < 0.1$  [Alder, 2015; Dowell, 1971, 1973; Gordnier and Visbal, 2002]. For a Mach number of 2, negligible discrepancies were found between inviscid and turbulent panel flutter [Alder, 2015; Hashimoto et al., 2009].

**Laminar VS turbulent:** To the author's knowledge, an explicit comparison between laminar and turbulent panel flutter has only been made by Hashimoto et al. [2007]. For low supersonic Mach numbers, a laminar boundary layer was found to have a more stabilising effect compared to a turbulent one. For SWBLI, the result will most likely be much more complex and Reynolds number dependent.

### 3.3.3. Initial Conditions and Boundary Conditions

**Initial Conditions:** In the case of regular panel flutter, small perturbations are required to incite flutter. If a shock impinges on the panel, a steady pressure difference will automatically develop between the upper surface and the cavity. This is sufficient to excite instabilities, although it was found that strong dependence of the flutter behaviour on the initial shape of the plate exists. This was elaborated on in the previous section, but is quickly outlined here again. For average shock strengths ( $p_3/p_1 = 1.4$ ) for 2D panels and average to strong shocks ( $p_3/p_1 = 1.4 - 1.8$ ) for 3D panels, subcritical bifurcations are observed. If the initial shape of the plate equals the rigid flat plate solution, flutter occurs. If the initial condition is a deformed solution obtained previously at a lower dynamic pressure, a steady deformation arises. For stronger shock strength, supercritical behaviour is again observed for 2D plates, indicating that the dependency on the initial conditions is eliminated.

Regarding matching the experimental initial conditions with the computational ones, it becomes clear that this is simply not possible. If the spanwise edges are left free and the cavity pressure is obtained through pressure equalisation with the test section, the cavity pressure will strongly vary during windtunnel start-up. It would be extremely expensive to model the passing of the normal shock and the consequent cavity response, thus this is not an option. Instead, it should be shown using inviscid computations that large initial disturbances do not affect the statistically stationary panel response, i.e. the converged LCO does not depend

on the initial conditions.

**Plate Boundary Conditions:** In the vast majority of literature, the leading and trailing edges of the panel are either clamped or simply supported (pinned). The general outcome is clear: a simply supported boundary condition will be less constraining on the panel motion, and thus yield a panel with lower stiffness compared to a clamped boundary condition [Alder, 2015]. As touched upon in the discussion of  $a/b$ , 3D clamped-clamped or pinned-pinned plates will not yield different flutter behaviour (without shock impingement) compared to the 2D case for  $a/b < 2$ .

In the case of an impinging shock, the answer might not be so simple. To the author's knowledge, no research has been conducted that isolates the effect of the boundary conditions. The streamwise (leading and trailing edge) constraints will most likely affect the large mean deformations induced by the pressure jump over the shock, which in turn will nonlinearly affect the flowfield. Considering the spanwise constraints, it was also proven by Boyer et al. [2018] that the interaction of a shock and a 3D simply supported panel yields strong spanwise variation of the flow, as well as a dominant spanwise mode. It can therefore be argued that the effect of the boundary conditions is not solely a geometrical stiffening of the panel, but also a strong altering of the flow. Anyhow, as discussed in the section on  $p_c$ , leaving the spanwise edges free is most likely the best option to obtain an averaged cavity pressure. Thus, the plate is expected to behave two-dimensionally, and no extra geometrical stiffening is expected.

### 3.3.4. Other Parameters

**Thermal loads** can significantly affect panel flutter behaviour. Elevated material temperatures, due to for example aerodynamic heating during sustained supersonic flight, can induce a reduction in strength, while thermal stresses induced by temperature gradients can alter the material stiffness. In general, the aerothermal and aeroelastic aspects of the problem are considered separately, since the coupling between them is usually negligible [Houbolt, 1958]. While discussing the aeroelastic aspect in this chapter, it was always assumed no heat transfer occurs from the fluid to the structure. If the flow is inviscid, the boundary layer and the corresponding viscous dissipation is removed. In that case, the adiabatic wall temperature corresponds to the freestream temperature, since no kinetic energy is dissipated. As a result, no aerodynamic heating of the structure will occur. On the other hand, if the boundary layer is taken into account, the adiabatic wall temperatures can reach several multiples of the freestream temperature for high supersonic Mach numbers. It can be questioned if the assumption of zero heat transfer at the structure is then physical. The validity of an adiabatic boundary depends strongly on the scenario under consideration. If sustained supersonic flight is considered, timescales are sufficiently long for the structure to heat up, as for example the Concorde (Mach 2) and the Quiet Supersonic Platform (Mach 2.4) experienced skin panel temperatures of 108°C and 189°C respectively [Guo and Mei, 2006]. Ignoring the elevated material temperature in such an environment would not yield accurate results. In rocket nozzles, flow conditions are much more extreme. The hot gasses flowing through the nozzle usually exceed 3,000K, which can lead to nozzle temperatures of 2,000K after long burn times [Guobiao et al., 2007]. The high temperatures of the gas induce chemical reactions and severe heat-transfer [Hadjadj et al., 2015]. It must be noted though that in the context of SWBLI, only the initial start-up of the rocket engine is under consideration. This means time-scales are short, especially when considering the characteristic time-scales of the fluid and the structure. The thermal response time is usually an order of magnitude larger [Culler and McNamara, 2011], reducing the importance of considering the heat flux to the structure. Secondly, nearly all current studies involving high-fidelity computations of SWBLI induced flutter or asymmetric nozzle loads assume adiabatic wall conditions and low (100-300K) flow temperatures to allow comparison with wind-tunnel experiments or other literature [Baars et al., 2015; Boyer et al., 2016; Miller et al., 2012; Pasquariello et al., 2015; Visbal, 2014; Zauner, 2015]. Chaudhuri and Hadjadj [2012] did investigate high temperature (2,500K) 2D transient nozzle flow during engine start-up, but they also assumed adiabatic conditions. Thirdly, regenerative cooling and/or film cooling is often used to protect the nozzle from the extreme flow temperatures, as employed for example in the SSME and Vulcain-1 [Shine and Nidhi, 2018]. This again reduces structural temperatures, but it must be noted that the inclusion of film cooling can greatly affect side-loads [Boccaletto et al., 2007; Wang and Guidos, 2009]. Regarding the complexity of the phenomena at work and the subject of the thesis, the author is convinced adiabatic and wind-tunnel temperature conditions should be used in the current study, to focus on the pure aeroelastic phenomena and to compare with recent work on Shock Wave Turbulent Boundary Layer Interaction.

**One- or two-sided flow:** In some high speed applications, such as scramjets or nozzles, high speed flow can

occur at two sides of the panel. This was studied by Zhou et al. [2012] using von Kármán large deflection theory and first order piston theory. It was found that a panel becomes more prone to instability when both surfaces are subject to aerodynamic loading. A similar result was obtained by Ye et al. [2018] for one side of the panel subject to an impinging shock.

Since mainly the conditions in a rocket nozzle at start-up are under consideration here, it is assumed the dynamic pressure on the outside is negligible. Next to that, to the author's knowledge, no high fidelity work on a panel with flow on both sides is currently available. One-sided flow is therefore assumed considering the scenario under consideration and to facilitate comparison with other work.

# 4

## Analytical Model for Shock-Panel Interaction

In this chapter the sensitivity of the flutter boundary of 2D simply supported plates with respect to the parameters discussed in Chapter 3 is investigated analytically. To the author's knowledge, only two publications exist on the analytical investigation of the flutter behaviour of flexible panels subject to an impinging shock. First of all, Ye et al. [2018] employ a typical Type III method, i.e. a linear aerodynamic model coupled to a nonlinear structure as categorised by Dowell [1970], to analyse the response of a 2D simply supported panel to an oblique shock impinging on the plate midpoint. Next to that, the effect of thermal stress due to an increased panel temperature, as well as the possibility to account for flow on both sides of the panel, is included. Routh-Hurwitz stability analysis is employed in order to obtain an explicit closed-form solution of the stability boundaries of the plate. The Routh-Hurwitz stability criterion boils down to arranging the coefficients of the characteristic polynomial of the linear system into a square Hurwitz matrix, after which stability of the polynomial can be determined based on the properties of the determinants of the principal submatrices [Hurwitz, 1895; Routh, 1877].

The method was extended by Ye and Ye [2018] to also include the effect of a different shock impingement location. It was decided to implement this version, since including the varying shock location does not pose a significant increase in complexity. Note that the thermal effect and the two-sided flow are also incorporated for the sake of completeness, although it was decided in Chapter 3 that they are not relevant for the current analysis. Following the steps outlined by Ye and Ye [2018] though, implementing these should be trivial and it might prove useful for future research. As a possible model improvement, the capability of including a steady pressure difference was added to the method. Lastly, for verification purposes, the semi-empirical method by Laurenson and McPherson [1977] to predict classic panel flutter is implemented as well. The latter features an empirical correction for three-dimensionality of the panel, which is also examined to perhaps predict unsteady behaviour of 3D panels subject to impinging shocks.

First, the methodology is introduced in Section 4.1. Secondly, the validity of the analytical approach is verified and validated in Section 4.2. Lastly, the results of the sensitivity study and important keypoints to keep in mind during further CFD analysis are presented in Section 4.3.

### 4.1. Methodology

In this section the methodology behind the the implemented models is outlined. First, the analytical/semi-empirical model for classic panel flutter by Laurenson and McPherson [1977] is introduced in Section 4.1.1. Next, the analytical model for panel flutter with shock impingement by Ye and Ye [2018] is elaborated on in Section 4.1.2. Lastly, the addition of a steady pressure term is explained in Section 4.1.3.

#### 4.1.1. Classic Panel Flutter

The design procedure for flutter-free surface panels by Laurenson and McPherson [1977] is mainly based on curve-fitting of well converged modal solutions. The effects of in-plane loading, flow angularity, plate pressure differential and edge boundary condition are incorporated using empirical corrections. Due to the

method being partially based on experimental data, a nominal structural damping is already included, which corresponds more or less to a damping coefficient  $g$  of 0.01. This is a widely used value for linear models. Based on the governing parameters selected in Section 3.3, the following effects are implemented here: static pressure differential over the plate, Mach number, plate length-to-width ratio, and panel boundary conditions.

The flutter boundary is expressed as a flutter parameter  $FP$ . It is a function of a geometry parameter  $GP$  and the panel edge rotational restraint  $E_C$ :

$$FP = \frac{E_C}{5 + 2(GP)^2 + 0.018(GP)^3} \quad (4.1)$$

For an isotropic panel with no inplane load, the geometry parameter simply equals the length-to-width ratio of the panel. The edge rotational restraint depends both on the type of boundary condition (simply supported/clamped) and the value of  $GP$ , as shown in Eq. (4.3).

$$GP = \frac{a}{b} \quad (4.2)$$

$$E_C = \begin{cases} 0.016 & \text{Clamped, } GP \geq 0.1 \\ 0.0157 & \text{Clamped, } GP < 0.1 \\ 0.027 & \text{Simply supported, } GP \geq 0.1 \\ 0.0292 & \text{Simply supported, } GP < 0.1 \end{cases} \quad (4.3)$$

Since the flutter parameter is also defined as

$$FP = \frac{Df(M)}{qa^3} \quad (4.4)$$

and the nondimensional dynamic pressure is given by

$$\lambda = \frac{2qa^3}{Df(M)}, \quad (4.5)$$

both the dimensional and nondimensional flutter dynamic pressures can be calculated as a function of  $FP$ :

$$q = \frac{Df(M)}{FPa^3}, \quad (4.6)$$

$$\lambda = \frac{2f(M)}{FP}. \quad (4.7)$$

In this case,  $f(M)$  is defined as the Prandtl-Glauert factor for  $M \geq 2$ , since results are partially based on piston theory. For  $M < 2$ , empirical correction factors are provided, but it is decided to only focus on high supersonic Mach numbers to steer away from any single-mode flutter occurrences. Finally, the effect of a static pressure differential over the plate can be taken into account as follows. For an isotropic panel, a nondimensional pressure parameter can be defined as:

$$p_f = \frac{\Delta p a^4}{Dh}, \quad (4.8)$$

where  $\Delta p$  is the out-of-plane pressure jump over the plate. Based on experimental data, Laurenson and McPherson provide a relation between the pressure correction factor  $Q_p$  and  $p_f$  for three different length-to-width ratio's. The curves for  $a/b = 0.46$  and  $a/b = 2.18$  were implemented in Python, after which 6th degree polynomials were least-squares fitted to the data points. For a certain length-to-width ratio and pressure parameter, the closest implemented  $a/b$  value is selected and the corresponding  $Q_p$  is returned. The dynamic pressure is then corrected by multiplying it with the obtained pressure correction factor.

### 4.1.2. Flutter of a Flat Plate Subject to an Impinging Shock

As stated earlier, the method implemented by both Ye et al. [2018] and Ye and Ye [2018] is based on a type III analysis. This entails first of all that the structural model is nonlinear. In this case, the equation of motion for a 2D plate under cylindrical bending is derived using Hamilton's principle, resulting in

$$D \frac{\partial^4 w}{\partial x^4} - (N_x - N_x^T) \frac{\partial^2 w}{\partial x^2} + \rho h \frac{\partial^2 w}{\partial t^2} + p(x, t) = 0. \quad (4.9)$$

Assuming the von Kármán formulation for the strain leads to the following stabilising force due to stretching of the plate:

$$N_x = \frac{E_s h}{2a(1 - \nu_s^2)} \int_0^a \left( \frac{\partial w}{\partial x} \right)^2 dx \quad (4.10)$$

The von Kármán plate thus clearly yields a nonlinear governing equation for the structure. The thermal stress is included by assuming a uniform temperature distribution over the entire panel, resulting in the following expression for  $N_x^T$ :

$$N_x^T = E_s h \alpha_s (T - T_0), \quad (4.11)$$

where  $\alpha$  is the coefficient of thermal expansion. Considering the determination of the aerodynamic pressure, first-order local piston theory is used, which is also typical for a Type III method. Ye and Ye [2018] utilise a modified version, which allows to include the pressure jump over the incident-reflected shock system. The incident shock, reflected shock and panel divide the flow in different regions, each with different Mach numbers, static pressures and densities. This is illustrated in Fig. 4.1, which is adapted from Ye and Ye [2018]. Note that the nomenclature of Ye and Ye [2018] is used here for the sake of reproducibility, in contrast to the conventions employed elsewhere in the report.

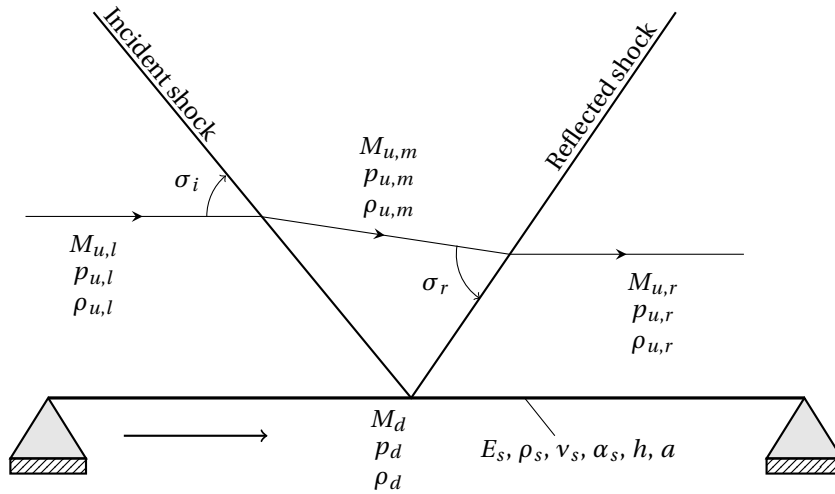


Figure 4.1: Schematic of the flow and structure considered by Ye and Ye [2018]

The total aerodynamic pressure on the upper left, upper right and lower side of the panel can be written respectively as:

$$p_{u,l} = p_{s(u,l)} + \frac{2q_{u,l}}{M_{u,l}} \left[ \frac{\partial w}{\partial x} + \frac{1}{U_{u,l}} \frac{\partial w}{\partial t} \right] \quad (4.12)$$

$$p_{u,r} = p_{s(u,r)} + \frac{2q_{u,r}}{M_{u,r}} \left[ \frac{\partial w}{\partial x} + \frac{1}{U_{u,r}} \frac{\partial w}{\partial t} \right] \quad (4.13)$$

$$p_d = p_{s(d)} + \frac{2q_d}{M_d} \left[ \frac{\partial w}{\partial x} + \frac{1}{U_d} \frac{\partial w}{\partial t} \right], \quad (4.14)$$

where  $p_s$  is the steady, static pressure. To focus on unsteady effects, it is assumed the steady pressure on the top side ( $p_{s(u,l)}$  or  $p_{s(u,r)}$ ) always equals the steady pressure on the bottom ( $p_{s(d)}$ ) for all locations on the

plate. This ensures the steady pressure drops out when the pressure difference over the plate is considered. The governing equation, i.e. Eq. (4.9), is put in nondimensional form as follows:

$$\frac{\partial^2 W}{\partial \tau^2} - (R_x - R_x^T) \frac{\partial^2 W}{\partial \xi^2} + \frac{\partial^4 W}{\partial \xi^4} + \bar{P} = 0, \quad (4.15)$$

where the parameters are nondimensionalised as given below. Note that in this case the nondimensional dynamic pressure  $\lambda$  is normalised with the Prandtl-Glauert correction factor  $\beta$ , in contrast to  $\lambda^*$  which is typically used to nondimensionalise high fidelity results, as outlined in Section 3.3.

$$\begin{aligned} \xi &= \frac{x}{a}, \quad \tau = t \sqrt{\frac{D}{\rho h a^4}}, \quad \lambda_{u,l(r)} = \frac{2q_{u,l(r)} a^3}{DM_{u,l(r)}}, \quad \lambda_d = \frac{2q_d a^3}{DM_d}, \quad W = \frac{w}{h} \\ \mu_{u,l(r)} &= \frac{\rho_{u,l(r)} a}{\rho h}, \quad \mu_d = \frac{\rho_d a}{\rho h}, \quad R_x^T = \frac{N_x^T a^2}{D}, \quad R_x = \frac{N_x a^2}{D} = 6 \int_0^1 \left( \frac{\partial W}{\partial \xi} \right)^2 d\xi \\ R_{Mu,l(r)} &= \frac{\mathcal{M}_{u,l(r)}}{M_{u,l(r)}}, \quad R_{Md} = \frac{\mathcal{M}_d}{M_d}, \quad \bar{p} = \frac{a^4}{Dh} p \end{aligned}$$

Eq. (4.15) is then solved using a Galerkin method. A Fourier expansion of the deflection can be obtained by expanding it in terms of sinusoidal basis functions:

$$W(\xi, \tau) = \sum_{i=1}^{\infty} q_i(\tau) \sin(i\pi\xi). \quad (4.16)$$

Note that the time-dependent amplitudes  $q_i$  are not related to the dynamic pressure  $q$ . Executing the Galerkin method by multiplying with the basis function and integrating over the domain, i.e. the panel length, the governing PDE can be rewritten to a system of nonlinear ODE's. Note that the pressure term has to be split in a pre- and post-shock part:

$$\int_0^1 \bar{p} = \int_0^k (\bar{p}_{u,l} - \bar{p}_d) + \int_k^1 (\bar{p}_{u,r} - \bar{p}_d), \quad (4.17)$$

where  $k = x_i/a$  is the nondimensional shock impingement location. In short, the resulting nonlinear ODE's can be written as:

$$\ddot{q}_j(\tau) + [(j\pi)^4 - R_x^T (j\pi)^2] q_j(\tau) + 3(j\pi)^2 q_j(\tau) \sum_{i=1}^N (i\pi)^2 q_i^2(\tau) - q^* = 0, \quad (4.18)$$

where  $q^*$  equals  $q_1 + q_2 + q_3 + q_4 + q_5$ , which are given by a slightly modified version of the expressions employed by Ye and Ye [2018], since it was observed a shorter notation was possible:

$$\begin{aligned} q_1 &= \lambda_{u,l} \left( q_j(\tau) \left[ \frac{1}{2} \cos(2j\pi k) - \frac{1}{2} \right] + \sum_{i \neq j}^{\infty} q_i(\tau) i \left[ \frac{\cos(j\pi k + i\pi k)}{j+i} + \frac{\cos(j\pi k - i\pi k)}{j-i} - \frac{1}{j+i} - \frac{1}{j-i} \right] \right) \\ q_2 &= \lambda_{u,r} \left( q_j(\tau) \left[ \frac{1}{2} \cos(2j\pi) - \frac{1}{2} \cos(2j\pi k) \right] + \sum_{i \neq j}^{\infty} q_i(\tau) i \left[ \frac{\cos(j\pi + i\pi)}{j+i} + \frac{\cos(j\pi - i\pi)}{j-i} - \frac{\cos(j\pi k + i\pi k)}{j+i} - \frac{\cos(j\pi k - i\pi k)}{j-i} \right] \right) \\ q_3 &= \lambda_d \left( q_j(\tau) \left[ \frac{1}{2} \cos(2j\pi) - \frac{1}{2} \right] + \sum_{i \neq j}^{\infty} q_i(\tau) i \left[ \frac{\cos(j\pi + i\pi) - 1}{j+i} + \frac{\cos(j\pi - i\pi) - 1}{j-i} \right] \right) - \sqrt{R_{Md} \lambda_d} \dot{q}_j(\tau) \\ q_4 &= \sqrt{R_{Mu,l} \lambda_{u,l}} \left( \dot{q}_j(\tau) \left[ -k + \frac{\sin(2j\pi k)}{2j\pi} \right] + \sum_{i \neq j}^{\infty} \dot{q}_i(\tau) \left[ -\frac{\sin(j\pi k - i\pi k)}{j\pi - i\pi} + \frac{\sin(j\pi k + i\pi k)}{j\pi + i\pi} \right] \right) \\ q_5 &= \sqrt{R_{Mu,r} \lambda_{u,r}} \left( \dot{q}_j(\tau) \left[ -1 + k - \frac{\sin(2j\pi k)}{2j\pi} \right] + \sum_{i \neq j}^{\infty} \dot{q}_i(\tau) \left[ \frac{\sin(j\pi k - i\pi k)}{j\pi - i\pi} - \frac{\sin(j\pi k + i\pi k)}{j\pi + i\pi} \right] \right). \end{aligned} \quad (4.19)$$

These are once again not to be confused with the dynamic pressure  $q$  or with the modal coefficients  $q_i(\tau)$ . In the paper by Ye and Ye [2018], only a two-mode Routh-Hurwitz solution of the flutter boundary is derived. Some results for four and six modes are presented as well, but no derivation is provided. Four to six modes are required for fully converged results though, as stated by Dowell [1966]. From the results by Ye and Ye [2018] it is clear that six modes only provide a small increase in accuracy compared to four, and mainly only for significantly aft shock impingement locations. Therefore, an attempt is made to implement a four mode Routh-Hurwitz stability analysis of Eq. (4.15). Selecting four modes, i.e.  $1 \leq i \leq 4$  and  $1 \leq j \leq 4$ , results in eight unknowns:

$$\left\{ \begin{array}{l} x_1 = q_1 \\ x_2 = q_2 \\ x_3 = q_3 \\ x_4 = q_4 \\ x_5 = \dot{q}_1 \\ x_6 = \dot{q}_2 \\ x_7 = \dot{q}_3 \\ x_8 = \dot{q}_4 \end{array} \right. \quad (4.20)$$

Note that assuming two modes results in four unknowns, as shown by Ye and Ye [2018]. Writing out Eq. (4.15) and Eq. (4.19), an equation for each  $\ddot{q}_j(\tau)$  can be obtained in function of the other  $q_j(\tau)$  and  $\dot{q}_j(\tau)$ . The stability of the system can be investigated by linearising the governing equations and evaluating them at the plate equilibrium solution. With no steady pressure difference over the plate, it can be easily shown that the equilibrium solution equals the flat plate shape ( $q_1, q_2, q_3$  and  $q_4 = 0$ ). Conveniently, this ensures the nonlinear term in Eq. (4.18) drops out. Therefore, the governing equations can be written in the form  $\dot{\mathbf{x}} = \mathbf{A}\mathbf{x}$ , where  $\mathbf{A}$  is the Jacobi matrix evaluated at the flat plate position:

$$\begin{pmatrix} \dot{x}_1 \\ \dot{x}_2 \\ \dot{x}_3 \\ \dot{x}_4 \\ \dot{x}_5 \\ \dot{x}_6 \\ \dot{x}_7 \\ \dot{x}_8 \end{pmatrix} = \begin{bmatrix} 0 & 0 & 0 & 0 & 1 & 0 & 0 & 0 \\ 0 & 0 & 0 & 0 & 0 & 1 & 0 & 0 \\ 0 & 0 & 0 & 0 & 0 & 0 & 1 & 0 \\ 0 & 0 & 0 & 0 & 0 & 0 & 0 & 1 \\ a_{51} & a_{52} & a_{53} & a_{54} & a_{55} & a_{56} & a_{57} & a_{58} \\ a_{61} & a_{62} & a_{63} & a_{64} & a_{65} & a_{66} & a_{67} & a_{68} \\ a_{71} & a_{72} & a_{73} & a_{74} & a_{75} & a_{76} & a_{77} & a_{78} \\ a_{81} & a_{82} & a_{83} & a_{84} & a_{85} & a_{86} & a_{87} & a_{88} \end{bmatrix} \begin{pmatrix} x_1 \\ x_2 \\ x_3 \\ x_4 \\ x_5 \\ x_6 \\ x_7 \\ x_8 \end{pmatrix}. \quad (4.21)$$

The entries of  $\mathbf{A}$  can all be written in function of  $\lambda_{u,l}$  by substituting

$$n = \lambda_{u,r} / \lambda_{u,l}, \quad (4.22)$$

$$m = \lambda_d / \lambda_{u,l}. \quad (4.23)$$

Note that the dynamic pressure ratio  $n$  can be obtained for an impinging shock with angle  $\sigma$  by assuming a regular reflection and employing the oblique shock relations [Shapiro and Shapiro, 1987]. The entries of the Jacobian matrix at the flat plate equilibrium are given in Appendix A. First, the characteristic equation of the linear adjoint system is calculated:

$$|A - \Omega I| = 0, \quad (4.24)$$

where  $\Omega = \Omega_R \pm i\Omega_I$ . For the system to become unstable, the real part of  $\Omega$  has to move to the positive axis, i.e.  $\Omega_R > 0$ . For the four-mode case, the characteristic equation was calculated using Maple, which yielded the following 8th order polynomial:

$$|A - \Omega I| = \Omega^8 + A_7\Omega^7 + A_6\Omega^6 + A_5\Omega^5 + A_4\Omega^4 + A_3\Omega^3 + A_2\Omega^2 + A_1\Omega + A_0, \quad (4.25)$$

where

$$\begin{aligned}
A_0 &= A_{04}\lambda_{u,l}^4 + A_{03}\lambda_{u,l}^3 + A_{02}\lambda_{u,l}^2 + A_{01}\lambda_{u,l} + A_{00} \\
A_1 &= A_{14}\lambda_{u,l}^{7/2} + A_{13}\lambda_{u,l}^{5/2} + A_{12}\lambda_{u,l}^{3/2} + A_{11}\lambda_{u,l}^{1/2} \\
A_2 &= A_{23}\lambda_{u,l}^3 + A_{22}\lambda_{u,l}^2 + A_{21}\lambda_{u,l} + A_{20} \\
A_3 &= A_{33}\lambda_{u,l}^{5/2} + A_{32}\lambda_{u,l}^{3/2} + A_{31}\lambda_{u,l}^{1/2} \\
A_4 &= A_{42}\lambda_{u,l}^2 + A_{41}\lambda_{u,l} + A_{40} \\
A_5 &= A_{52}\lambda_{u,l}^{3/2} + A_{51}\lambda_{u,l}^{1/2} \\
A_6 &= A_{61}\lambda_{u,l} + A_{60} \\
A_7 &= A_{71}\lambda_{u,l}^{1/2}.
\end{aligned} \tag{4.26}$$

The coefficients in Eq. (4.26) ( $A_{04}, A_{03}, \dots, A_{71}$ ) are all functions of the entries of the Jacobian matrix. Since they are already quite extensive and implemented in the Python code, they are not shown here. Finally, to determine the stability of the system, the Routh-Hurwitz criterion is applied to Eq. (4.25). This was done numerically in Maple, which yielded multiple (8) inequalities. These have to be satisfied to guarantee the plate is stable. Flutter is not the only instability though, as divergence can also occur. Many of the obtained inequalities can be proven to be satisfied for physical values of the mass ratio's and dynamic pressures [Ye and Ye, 2018]. Since only the flutter boundary is of interest here, the corresponding Routh-Hurwitz criterion was identified after some trial and error:

$$t_1 - \frac{t_2}{t_3 - \frac{t_4}{t_5}} > 0. \tag{4.27}$$

The unknowns  $t_{1..5}$ , are extensive functions of the coefficients of the characteristic equations, as shown in Appendix B. Eq. (B.1) to Eq. (B.5) can be rewritten as polynomials in  $\lambda_{u,l}$  to reduce their size and aid Maple in computing the result of Eq. (4.27). This gives:

$$\begin{aligned}
t_1 &= \frac{(t_{1c1}\lambda_{u,l}^7 + t_{1c2}\lambda_{u,l}^6 + t_{1c3}\lambda_{u,l}^5 + t_{1c4}\lambda_{u,l}^4 + t_{1c5}\lambda_{u,l}^3 + t_{1c6}\lambda_{u,l}^2 + t_{1c7}\lambda_{u,l} + t_{1c0} + t_{1c8})\sqrt{\lambda_{u,l}}}{t_{1c9}\lambda_{u,l}^4 + t_{1c10}\lambda_{u,l}^3 + t_{1c11}\lambda_{u,l}^2 + t_{1c12}\lambda_{u,l} + t_{1c13}} \\
t_2 &= \left( t_{2c2}\lambda_{u,l}^6 + t_{2c3}\lambda_{u,l}^5 + t_{2c4}\lambda_{u,l}^4 + t_{2c5}\lambda_{u,l}^3 + t_{2c6}\lambda_{u,l}^2 + t_{2c7}\lambda_{u,l} + t_{2c1} + t_{2c8} \right) \\
&\quad \cdot \frac{(A_{04}\lambda_{u,l}^4 + A_{03}\lambda_{u,l}^3 + A_{02}\lambda_{u,l}^2 + A_{01}\lambda_{u,l} + A_{00})\sqrt{\lambda_{u,l}}}{t_{2c9}\lambda_{u,l}^4 + t_{2c10}\lambda_{u,l}^3 + t_{2c11}\lambda_{u,l}^2 + t_{2c12}\lambda_{u,l} + t_{2c13}} \\
t_3 &= -\frac{t_{3c1}\lambda_{u,l}^5 + t_{3c2}\lambda_{u,l}^4 + t_{3c3}\lambda_{u,l}^3 + t_{3c4}\lambda_{u,l}^2 + t_{3c5}\lambda_{u,l} + t_{3c6}}{t_{3c7}\lambda_{u,l}^2 + t_{3c8}\lambda_{u,l} + t_{3c9}} \\
t_4 &= \frac{(t_{4c1}\lambda_{u,l}^7 + t_{4c2}\lambda_{u,l}^6 + t_{4c3}\lambda_{u,l}^5 + t_{4c4}\lambda_{u,l}^4 + t_{4c5}\lambda_{u,l}^3 + t_{4c6}\lambda_{u,l}^2 + t_{4c7}\lambda_{u,l} + t_{4c8})\sqrt{\lambda_{u,l}}}{t_{4c9}\lambda_{u,l}^2 + t_{4c10}\lambda_{u,l} + t_{4c11}} \\
t_5 &= -\frac{(t_{5c2}\lambda_{u,l}^6 + t_{5c3}\lambda_{u,l}^5 + t_{5c4}\lambda_{u,l}^4 + t_{5c5}\lambda_{u,l}^3 + t_{5c6}\lambda_{u,l}^2 + t_{5c7}\lambda_{u,l} + t_{5c1} + t_{5c8})\sqrt{\lambda_{u,l}}}{t_{5c9}\lambda_{u,l}^4 + t_{5c10}\lambda_{u,l}^3 + t_{5c11}\lambda_{u,l}^2 + t_{5c12}\lambda_{u,l} + t_{5c13}}.
\end{aligned}$$

The coefficients  $t_{1c1}, t_{1c2}, \dots, t_{5c13}$  are very extensive functions of  $A_{04}, A_{03}, \dots, A_{71}$ , and are therefore not shown in the report. Instead, the reader is referred to the "Ye\_4\_mode.py" Python file, where all coefficients are readily available. As a final step, the simplified  $t$ -coefficients were fed into Eq. (4.27), resulting in an expression with in the numerator a 24th order Polynomial multiplied by  $\sqrt{\lambda_{u,l}}$ . Note that the arithmetic was once again performed in Maple, yielding:

$$\begin{aligned}
&C_{24}\lambda_{u,l}^{24} + C_{23}\lambda_{u,l}^{23} + C_{22}\lambda_{u,l}^{22} + C_{21}\lambda_{u,l}^{21} + C_{20}\lambda_{u,l}^{20} + C_{19}\lambda_{u,l}^{19} + C_{18}\lambda_{u,l}^{18} + C_{17}\lambda_{u,l}^{17} + C_{16}\lambda_{u,l}^{16} \\
&+ C_{15}\lambda_{u,l}^{15} + C_{14}\lambda_{u,l}^{14} + C_{13}\lambda_{u,l}^{13} + C_{12}\lambda_{u,l}^{12} + C_{11}\lambda_{u,l}^{11} + C_{10}\lambda_{u,l}^{10} + C_9\lambda_{u,l}^9 + C_8\lambda_{u,l}^8 + C_7\lambda_{u,l}^7 \\
&+ C_6\lambda_{u,l}^6 + C_5\lambda_{u,l}^5 + C_4\lambda_{u,l}^4 + C_3\lambda_{u,l}^3 + C_2\lambda_{u,l}^2 + C_1\lambda_{u,l} + C_0 > 0.
\end{aligned} \tag{4.28}$$

Coefficients  $C_0, C_1, \dots, C_{24}$  are also available in the Python file (once again, very extensive), where they are implemented in function of the  $t$ -coefficients. Finding the roots of Eq. (4.28) is trivial in e.g. Python or Matlab, and one of the 24 roots yields the flutter dynamic pressure.

The stability of the system can also be analysed without the Routh-Hurwitz criterion. The eigenvalues of the  $A$ -matrix can be obtained by calculating the roots of the characteristic equation, after which the dynamic pressure can be increased until one of the eigenvalues becomes unstable ( $\Omega_R > 0$ ). The dynamic pressure at which this occurs will equal the flutter dynamic pressure, as long as the shock strength is not too high. When the shock strength is increased above a certain critical value, the lower stability boundary will suddenly shift downwards from a flutter instability to a buckling instability. This is indicated by the most unstable eigenvalue becoming real instead of complex, and this will be elaborated on in Section 4.2. Using this approach is slower and less accurate than employing the Routh-Hurwitz criterion, since the eigenvalues have to be recomputed several times before the flutter boundary is found. On the other hand, implementing the Routh-Hurwitz criterion is not straightforward for  $N$  exceeding four, while the eigenvalue analysis can be executed for an arbitrary number of modes.

### 4.1.3. Flutter of a Statically Deformed Panel Subject to an Impinging Shock

Assuming a flat plate equilibrium solution is only valid if there is no net steady pressure difference over the plate. In reality, this will never be the case if a shock impinges on the panel. Instead, the presence of steady pressure forces will induce a static deformation of the plate, such as observed by Visbal [2012, 2014]. Therefore, the linearised stability of the plate around this new equilibrium solution is investigated here as well. Several simplifications are made. First of all, it is assumed the change in shock impingement location due to plate deformation is negligible. Secondly, the change in slope at the impingement point is assumed to not alter the strength of the reflected shock significantly. Therefore,  $k$  and  $n$  are not changed according to the steady plate deformation. Whether this yields reasonable results will be discussed in Section 4.2.4.

It is assumed the steady pressure on the bottom of the plate equals the average of the steady pressure on the upper surface, similar to the boundary conditions defined by Visbal [2012, 2014]. For a variable shock impingement point this gives:

$$p_{s(d)} = kp_{s(u,l)} + (1-k)p_{s(u,r)}, \quad (4.29)$$

which is equal to Eq. (3.1) with a different notation. Assuming a perfect gas, the steady pressure upstream of the impinging shock can be written in function of the nondimensional dynamic pressure and the Mach number:

$$p_{s(u,l)} = \frac{\lambda_{u,l} D}{\gamma a^3 M_{u,l}}. \quad (4.30)$$

Employing the same nondimensionalisation as for the unsteady pressure results in the introduction of only one extra nondimensional parameter, i.e. the thickness to length ratio  $h/a$ :

$$\bar{p}_{s(u,l)} = \frac{a}{h} \frac{\lambda_{u,l}}{\gamma M_{u,l}}. \quad (4.31)$$

Similarly, the nondimensional pressure downstream of the incident-reflected shock system can be written as

$$\bar{p}_{s(u,r)} = \frac{a}{h} \frac{n}{\eta} \frac{\lambda_{u,l}}{\gamma M_{u,l}}, \quad (4.32)$$

where  $\eta$  is the Mach number ratio  $M_{u,r}/M_{u,l}$ . The latter can be obtained from the oblique shock relations. Going back to Eq. (4.29), the nondimensional steady pressure on the bottom equals

$$\bar{p}_{s(d)} = \frac{a}{h} \frac{\lambda_{u,l}}{\gamma M_{u,l}} \left( k + (1-k) \frac{n}{\eta} \right). \quad (4.33)$$

Carrying out the integration introduced by the Galerkin decomposition as shown in Eq. (4.17) results in the following steady pressure term which has to be added to the governing equation:

$$\bar{p}_{s,j} = \frac{a}{h} \frac{\lambda_{u,l}}{\gamma M_{u,l}} \frac{1}{j\pi} \left( 1 - \frac{n}{\eta} \right) [1 - \cos(j\pi k) - k(1 - \cos(j\pi))]. \quad (4.34)$$

The equilibrium amplitudes  $q_{eq,i}$  can be obtained by setting all time derivatives in Eq. (4.18) equal to zero. The only unknowns in the  $N$  resulting nonlinear steady equations are the  $N$   $q_{eq,i}$ , and they can therefore be readily obtained for a given set of input parameters. The steady governing equation is now given by

$$[(j\pi)^4 - R_x^T(j\pi)^2] q_{eq,j}(\tau) + 3(j\pi)^2 q_{eq,j}(\tau) \sum_{i=1}^N (i\pi)^2 q_{eq,i}^2(\tau) - q^* + \bar{p}_{s,j} = 0, \quad (4.35)$$

where the  $q^*$  term now equals  $q_1 + q_2 + q_3$ , as shown in Eq. (4.19), due to the time dependent terms dropping out. Note that the  $\sqrt{\lambda_d}$  term in  $q_3$  also reduces to zero. Once the equilibrium amplitudes are known, the linear stability of the system around the new static equilibrium can be investigated. Note that due to the addition of the steady pressure term, the governing equation is now non-homogenous and of the form  $\dot{\mathbf{x}} = A\mathbf{x} + \mathbf{b}$ . The stability of the system can be assessed by considering the stability of the homogenous form though. The procedure boils down to calculating the equilibrium amplitudes, evaluating the Jacobian matrix at those amplitudes and lastly determining the most unstable eigenvalue of the system. Note that an explicit calculation of the flutter boundary using the Routh-Hurwitz criterion is not attempted here. In contrast to the flat plate solution, the nonlinear term  $f_j$  in the Jacobian matrix does not drop out and must therefore be linearised as follows.

$$f_j = 3(j\pi)^2 q_j(\tau) \sum_{i=1}^N (i\pi)^2 q_i^2(\tau) \quad (4.36)$$

$$\frac{\partial f_j}{\partial \mathbf{x}} = \sum_{p=1}^N \frac{\partial f_j}{\partial q_p(\tau)} \quad (4.37)$$

The nonlinear term can therefore be approximated by the following Taylor expansion:

$$\tilde{f}_j = \mathbf{x} \frac{\partial f_j}{\partial \mathbf{x}} \Big|_{\mathbf{x}=\mathbf{x}_{eq}} = \sum_{p=1}^N q_p(\tau) \frac{\partial f_j}{\partial q_{p,eq}} \Big|_{\mathbf{x}=\mathbf{x}_{eq}} \quad (4.38)$$

Thus, the following governing dynamic linear ODE's are obtained:

$$\ddot{q}_j(\tau) + [(j\pi)^4 - R_x^T(j\pi)^2] q_j(\tau) + 3(j\pi)^2 \sum_{p=1}^N \left[ q_p(\tau) \frac{\partial}{\partial q_{p,eq}} \left( q_{j,eq}(\tau) \sum_{i=1}^N (i\pi)^2 q_{i,eq}^2(\tau) \right) \right] - q^* = 0. \quad (4.39)$$

## 4.2. Verification and Validation

In this section, it is verified if the method Ye and Ye [2018] is implemented correctly, and whether or not it results in the expected flutter behaviour. Note that unless mentioned otherwise, the mass ratio's  $\mu$  are set to 0.1, identical to the values used by Visbal [2012, 2014].

### 4.2.1. Python Script Outline

First of all, a quick outline of the written Python script is appropriate. The eigenvalue analysis is employed here instead of the Routh-Hurwitz criterion, since this allows the inclusion of at least six modes. As a first step, the software checks if the entries of the Jacobian matrix, Eq. (4.21), are available in symbolic form. If not, command-line Maple is started and both the  $A$ -matrix entries and characteristic coefficients are computed for the desired mode number. Next, these are fed into python and evaluated for the user-specified inputs  $M$ ,  $k$ ,  $n$ ,  $m$ , air density  $\rho_\infty$ , plate density  $\rho$ , mass ratio's  $R_{Mu,l}$ ,  $R_{Mu,r}$  and  $R_{Md}$ , and a thermal stretching force  $R_x^T$ . If a steady deformed solution is required, also the plate length  $a$  and thickness  $h$  are to be specified. Considering  $n$  and the mass ratio's, different possibilities are included, indicated by the variable 'INPUTMODE':

- **HARDCODED:** The dynamic pressure ratio  $n$  and the mass ratio's are prescribed by the user. The Mach number ratio  $\eta$  for the deformed equilibrium solution is computed.
- **PHYSICAL:** The dynamic pressure ratio  $n$  and the Mach number ratio  $\eta$  are computed from what is specified by 'SHOCK STRENGTH' using the oblique shock relations. This shock strength can be defined in multiple ways, for which the variable 'SHOCK TYPE' is employed:

- **SIG**: The incident shock angle is specified.
- **PHI**: The flow deflection angle over the incident shock is specified.
- **PRAT**: The pressure ratio over the entire shock system is specified.

Secondly, the mass ratio's are computed from the given panel length, panel density, panel thickness and freestream density.

- **MIX**: A mix from the first two options. The post-shock states are calculated from the oblique shock relations, while the mass ratio's are prescribed. This option is used most often for the verification process, since the mass ratio's are always prescribed in literature.

The software can calculate  $R_x^T$  based on an absolute temperature difference or a critical temperature ratio, depending on whether 'ABS' or 'RAT' is selected for the 'T TYPE' parameter. Considering the relation between  $n$ ,  $p_3/p_1$  and  $\sigma$ , a slight discrepancy was found with the values presented by Ye and Ye [2018]. This is illustrated in Table 4.1, where values for  $\vartheta$  and  $\eta$  are presented as well for completeness. No explanation for the difference was found, and no mistake in the oblique shock calculations was discovered either. Next to that, the values for shock angle, post-shock Mach number and flow deflection angle associated to a certain pressure ratio presented by Boyer et al. [2018] were replicated exactly. Therefore, it is assumed the computations by the author are correct, and the values by Ye and Ye [2018] will only be used for verification with the results of the paper itself.

$\sigma$ [deg]	$\vartheta$ [°]	$p_3/p_1$ [-]	$p_3/p_1$ [-] [Ye and Ye, 2018]	$n$ [-]	$n$ [-] [Ye and Ye, 2018]	$\eta$ [-]
18	2.064	1.4269	1.4862	1.3260	1.3802	0.9293
20	4.7663	2.1991	2.0758	1.8557	1.8050	0.8439
22	7.254	3.1669	3.2955	2.440	2.5969	0.7704
24	9.5716	4.3298	4.1695	3.0530	3.1095	0.7051
27	12.797	6.4241	6.3622	3.9670	4.2560	0.6175
29	14.812	8.0381	8.2788	4.5340	5.1492	0.5641

Table 4.1: Relation between post-and pre-shock states for  $M = 3.5$  as computed with the author's Python code versus the values given by Ye and Ye [2018]

Returning to the Python script, once the inputs are computed, the Jacobian entries and consequently the coefficients of the characteristic equation can be evaluated using the Python library Sympy. If a deformed steady solution is desired, the equilibrium modal amplitudes are first calculated (also from a maple-python coupling). This process yields a very compact characteristic equation, with as only unknown  $\lambda$ . As a result, the flutter dynamic pressure can be calculated rapidly using eigenvalue analysis, i.e. ramping up the dynamic pressure until flutter is observed. If desired, the steady solution and/or the eigenvalues can also be calculated for a given dynamic pressure.

#### 4.2.2. Standard Panel Flutter

Moving on to the verification and validation process, the impinging shock is first left out, yielding a dynamic pressure ratio  $n$  of 1. The flutter behaviour with Mach number for a 2D flat plate without shock as obtained by the methods by Laurenson and McPherson [1977] and Ye and Ye [2018] is compared to results from literature. The accuracy of the Routh-Hurwitz approach is investigated as well. The flutter boundaries are shown in Fig. 4.2. A couple of things can be observed. First of all, it is clear that the difference between the two mode and four mode solution is significant, while the six mode solution ensures a converged result. Secondly, the flutter boundary obtained with the eigenvalue (EV) analysis of the method by Ye and Ye [2018] yields identical results to the Routh-Hurwitz (RH) approach. The two-and four mode LiPT results by Dowell [1966] agree nicely with the results by Ye and Ye [2018], since the small discrepancy can be attributed to the different mass ratio's ( $R_{Mu} = 0.01$  and  $R_{Mu} = 0.1/M$  respectively). Also the LiPT flutter dynamic pressure obtained by

Mei et al. [2014] shows only a tiny deviation, again attributable to a different mass ratio ( $R_{Mu} = 0.02$ ). Finally, both implemented methods by Ye and Ye [2018] and Laurenson and McPherson [1977] are in good agreement as well. The latter predicts a slightly lower flutter dynamic pressure, which might be again due to a different mass ratio. This cannot be verified though, since it is not mentioned which value is assumed.

It can be concluded that the mass ratio does not strongly affect the result, as stated earlier [Dowell, 1967, 1970]. Secondly, looking at the result obtained by Dowell [1967], who employed potential flow in combination with a nonlinear structural model (Type 4), linear piston theory and potential flow theory methods yield nearly identical flutter boundaries for  $M > 2$ .

Considering the Euler results, excellent agreement with the lower fidelity methods is observed for the results obtained by Visbal [2014]. Especially the six mode solutions seem to agree very well, as expected. Mei et al. [2014] and Davis and Bendiksen [1993] observed a slight increase in flutter dynamic pressure with respect to piston theory, while Visbal [2014] did not. Since the flutter dynamic pressures obtained by Visbal [2014] were verified by Alder [2015], and the results are clearly in better agreement with LiPT, potential flow theories and the semi-empirical result of Laurenson and McPherson [1977], it is assumed the Visbal and Alder results are correct.

The effect of panel three-dimensionality is examined in Fig. 4.3 for simply supported and clamped panels. Note that it is assumed the edge constraint applies to *all* edges, including the spanwise ones. Since the method by Ye and Ye [2018] does not include 3D effects, only the semi-empirical method by Laurenson and McPherson [1977] can be validated. Concerning pinned panels, the model agrees quite well with the analytical results of Dowell [1966] for panel length-to-width ratio's of 0 and 1, while a deviation of about 10% is observed for  $a/b = 2.0$ . High fidelity verification data is scarce, as only the von Kármán - Euler results by Boyer et al. [2018] were available at the time of writing. Good agreement exists between the three methods though, verifying that the implemented method is able to predict the stiffening effect of plates with moderate length-to-width ratio's for classic supersonic panel flutter. For clamped panels, results are similar: for low  $a/b$ , good agreement is obtained with the Type I results, i.e. a linear structure coupled to a linear aerodynamic model, of Dowell and Voss [1965] and the Euler results of Hashimoto et al. [2009]. For more slender panels though, the results by Dowell start to deviate significantly from the semi-empirical method. It could be the case though, that the flutter boundary obtained with the method by Laurenson and McPherson [1977] is actually more accurate, since comparison with experiments proved that the Type I method significantly underestimated the flutter dynamic pressure at Mach 2 [Dowell and Voss, 1965]. Sadly, no high fidelity inviscid data was found by the author to confirm this.

### 4.2.3. Panel Flutter with Shock Impingement

Considering verification of the method by Ye and Ye [2018] with an impinging shock, it is first checked if the eigenvalue approach captures all panel instabilities. Therefore, the instability boundary is plotted versus increasing shock strength in Fig. 4.4. It becomes clear that care must be taken when employing eigenvalue analysis for strong shocks. It can be observed that a static buckling instability occurs at lower dynamic pressures than the flutter instability for strong enough shocks, which can also be captured by the Routh-Hurwitz analysis if the corresponding stability criterion is derived. The first unstable eigenvalue is now real, since it represents a static instability. If the flutter boundary is desired, the dynamic pressure has to be increased more till the first unstable complex eigenvalue is obtained.

Secondly, it can be seen that the four and six mode solutions predict a much later transition from dynamic to static instability compared to the two mode solution. Next to that, it can be observed that the six mode solution starts to diverge from the four mode one for high shock strengths. It is therefore shown once again that six modes are crucial for a converged flutter boundary.

It must be noted that for the given Mach number of 3.5, the maximum attainable dynamic pressure ratio over an oblique I-R system is about 5.8. Indeed, a regular reflection at  $M = 3.5$  will only be possible up to a flow deflection angle  $\theta_i$  of about 23 degrees, since for steady inviscid flow the detachment criterion for weak reflections holds [Ben-Dor, 2007]. This flow deflection corresponds to an incident shock angle of 38.1 degrees, or a dynamic pressure ratio of 5.8. Therefore, examining again Fig. 4.4, the six and four mode solutions predict that this static instability will never occur for a physical oblique shock reflection.

The flutter dynamic pressure versus **shock strength** can be validated with the results of Visbal [2014]. Flutter boundaries for Mach numbers 2.0 and 2.5 are plotted in Fig. 4.5. Note that only the unstable branch of the subcritical Hopf bifurcations are plotted here. Results for shock pressure ratio's of 1 and 1.4 match rather well,

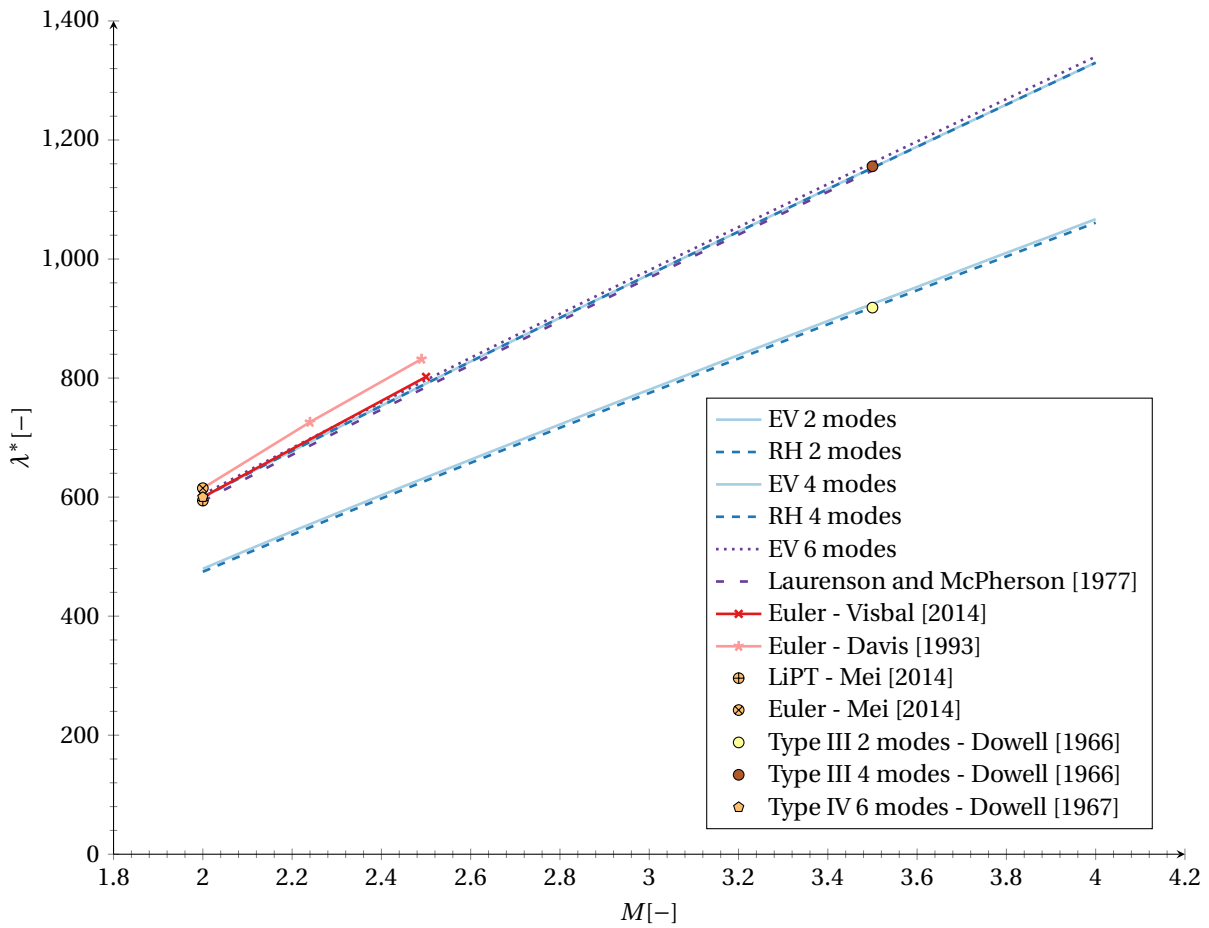


Figure 4.2: Flutter dynamic pressure versus Mach number

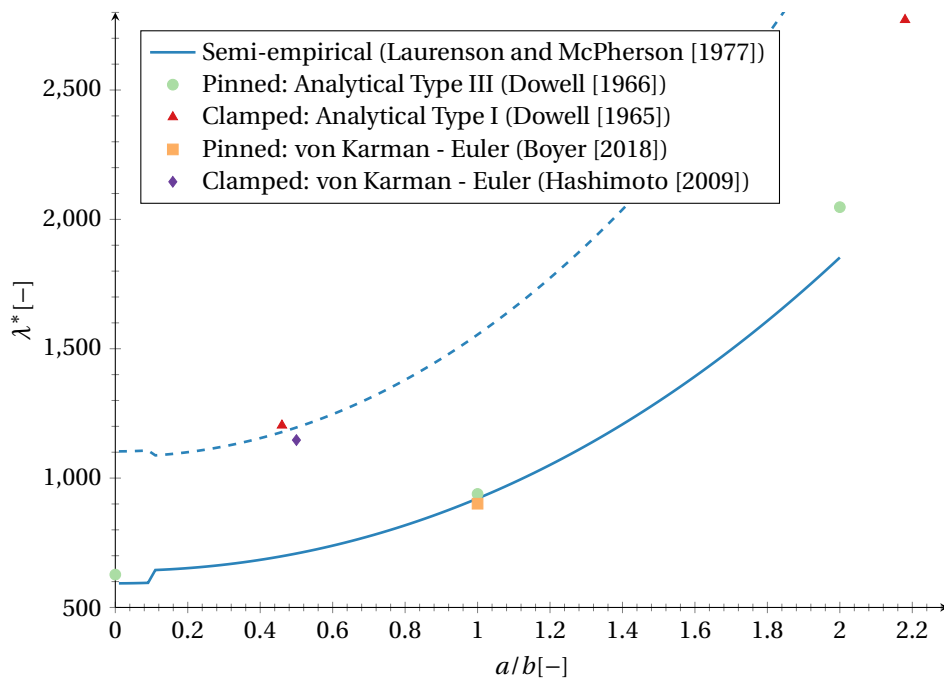


Figure 4.3: Flutter dynamic pressure versus panel length-to-width ratio for simply supported (—) and clamped (- - -) panels at  $M = 2.0$

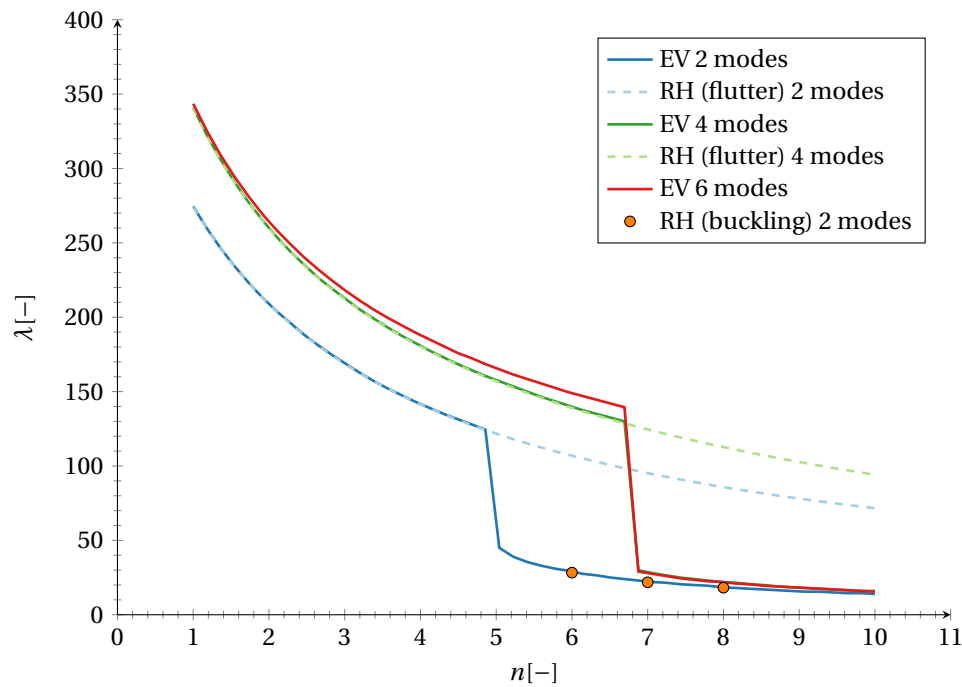


Figure 4.4: Flutter dynamic pressure versus dynamic pressure ratio

but a large discrepancy can be observed for a pressure ratio of 1.2. As explained in Section 3.1, this can be attributed to a stiffening of the plate due to the steady pressure difference between the upper side and the cavity. Naturally, this is not taken into account by the Type III method by Ye and Ye [2018], since a linearised solution around the flat plate equilibrium position is examined.

When the shock strength is increased beyond 1.4, the panel becomes severely more unstable. This behaviour is not captured by the LiPT method either, strongly over-predicting the flutter dynamic pressure. It is argued that inclusion of the panel steady deformation could improve the results, which is therefore attempted next.

It would be desirable to have an analytical method to estimate the flutter dynamic pressure of 3D clamped panels, since this boundary condition is the easiest to replicate experimentally [Dowell and Voss, 1965]. This will be elaborated on in Section 4.3. Sadly, to the authors knowledge, only one study exists on 3D inviscid panel flutter with shock impingement, and only simply square supported panels are considered. The results obtained by Boyer et al. [2018] were already discussed in Section 3.1, and are presented here in a different format. Looking at Fig. 4.6, it can be seen that increasing  $a/b$  from 0 to 1 for different shock strengths does not result in monotonous behaviour. It is clear the semi-empirical method by Laurenson and McPherson [1977] can only predict the geometrical stiffening of the plate without shock impingement. For  $p_3/p_1 = 1.4$ ,  $\lambda^*$  for the 2D panel more or less equals the flutter dynamic pressure for the shockless panel, which can be attributed to the subcritical behaviour of the 2D panel at that shock strength (flutter amplitude and frequency are increased as shown in Fig. 3.1). Increasing the panel length-to-width ratio to 1 results in a strong increase in  $\lambda^*$ , which would be severely underpredicted by the semi-empirical method. A different story unfolds for the stronger shock ( $p_3/p_1 = 1.8$ ), where the 2D flutter dynamic pressure is only 1/3th of the one obtained without shock, while in the 3D case an increase in  $\lambda$  is still obtained. This can be attributed to the 2D panel experiencing a supercritical instability, while the 3D panel is still subcritically unstable. As discussed by Boyer et al. [2018], it is expected that the 3D panel will follow the same behaviour as the 2D panel, but higher shock strengths are required to incite the supercritical instability.

A different view is presented in Fig. 4.7. The transition from sub to supercritical instability for the 2D plate entails a drop in  $\lambda^*$  of about 67%. Therefore, the author argues that for high enough shock strengths, the 3D panel flutter boundary will dip under the 2D boundary predicted by Ye and Ye [2018]. That way, the analytical boundary could serve as an upper boundary for the 3D flutter point, as it does for the 2D panel for shock strengths above  $p_3/p_1 = 1.4$ . This has never been confirmed before though [Boyer et al., 2018].

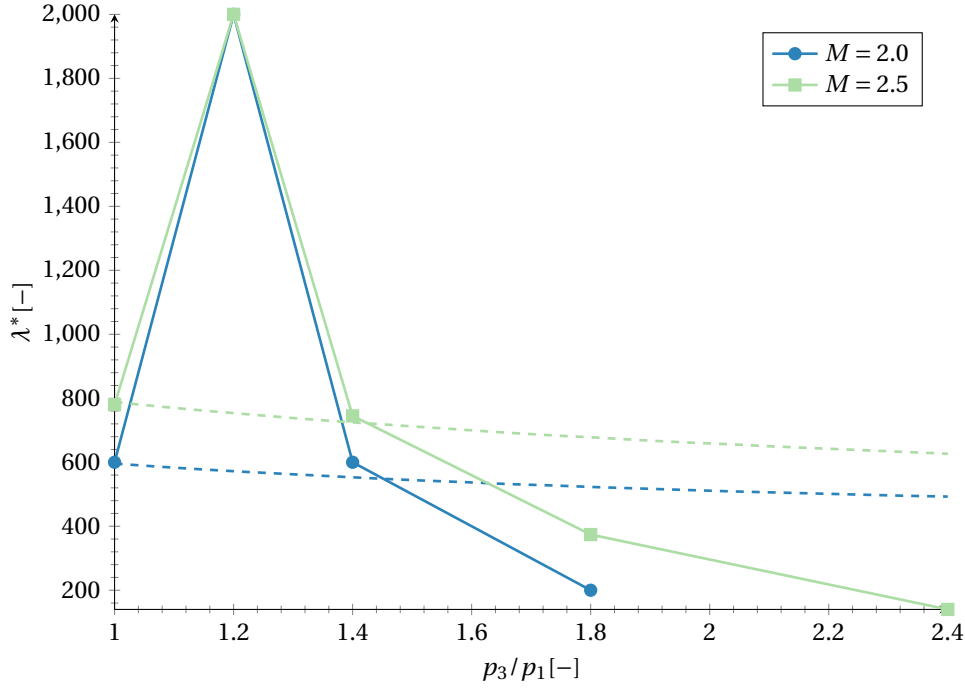


Figure 4.5: Flutter dynamic pressure versus shock strength for different Mach numbers (— Unsteady Euler - von Kármán [Visbal, 2014] - - LiPT - von Kármán (6 modes) [Ye and Ye, 2018])

The behaviour of the flutter dynamic pressure with **varying shock impingement location** is also investigated. Looking at Fig. 4.8, it becomes clear that six modes predict in general a slight increase in flutter dynamic pressure compared to the four mode solution, especially for shock locations close to the leading and trailing edge. This discrepancy does not seem to depend on shock strength. The implemented results match those of Ye and Ye [2018] and are therefore deemed verified. No validation is possible though, since no flutter boundaries for different shock positions are available in literature. The general trend observed by Visbal [2014] differs strongly from the one observed here, as discussed in Section 3.3.

#### 4.2.4. Panel Flutter with Deformed Equilibrium

First of all, it is checked if the deformed equilibrium solution is obtained correctly. Note that unless mentioned otherwise, a thickness to length ratio  $h/a$  of 0.002 is employed, similar to Visbal [2012, 2014]. In Fig. 4.9, the steady deformed equilibrium deflection of a panel subject to a shock impinging at the midpoint is shown for an increasing amount of modes. It is clear that six modes yield a converged solution, with eight or ten modes not yielding a visible increase in accuracy. Secondly, it can be seen that the typical steady deformed shape for a panel subject to a shock impinging at the midpoint is obtained: an asymmetric mainly second mode shape with the strongest deformation near the leading edge.

Next, the steady solution is verified with the results by Visbal [2014] for different shock locations in Fig. 4.10 and for different dynamic pressures and shock strengths in Fig. 4.11. First of all, looking at Fig. 4.11, it becomes clear that for a weak reflected shock system with pressure ratio  $p_3/p_1 = 1.2$ , the steady deflections obtained with piston theory match the mean deflections by Visbal quite nicely. The corresponding pressure distributions are given in Fig. 4.12 and Fig. 4.13. For the linear piston theory model, these were obtained exactly by writing the pressure terms Eq. (4.12) and Eq. (4.13) in nondimensional form and by substituting the freestream steady pressure as given by Eq. (4.30). This yields:

$$\frac{\bar{p}_u}{\bar{p}_{s,(ul)}} = \begin{cases} 1 + \frac{h}{a} \gamma M_{u,l} \frac{\partial W}{\partial \xi} & \xi < k \\ \frac{\bar{p}_{s,(ur)}}{\bar{p}_{s,(ul)}} + \frac{h}{a} \gamma n M_{u,l} \frac{\partial W}{\partial \xi} & \xi \geq k \end{cases} \quad (4.40)$$

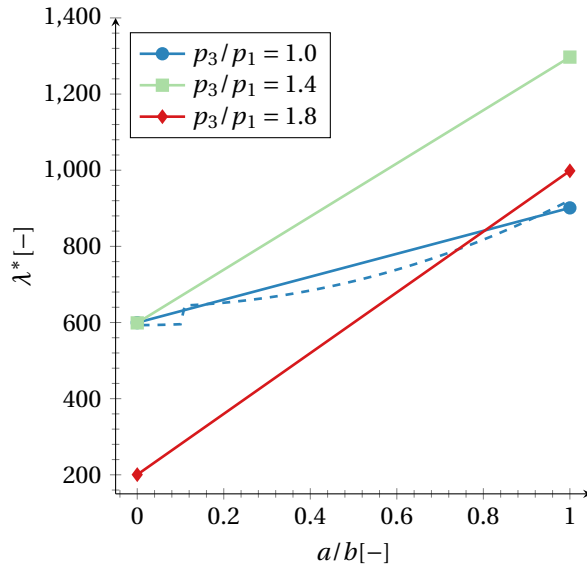


Figure 4.6: Flutter dynamic pressure versus panel length-to-width ratio for different shock strengths at  $M = 2.0$  (— Euler - von Kármán:  $a/b = 0.0$  [Visbal, 2014],  $a/b = 1.0$  [Boyer et al., 2018]. - - semi-empirical [Laurenson and McPherson, 1977])

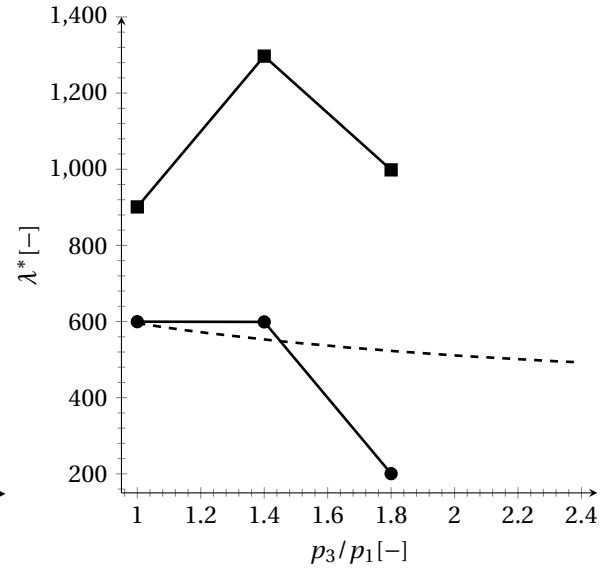


Figure 4.7: Flutter dynamic pressure versus shock strength for 2D and 3D simply supported panels at  $M = 2.0$  (- - LiPT - von Kármán [Ye and Ye, 2018], ● 2D Euler - von Kármán [Visbal, 2014], ■ 3D Euler - von Kármán [Boyer et al., 2018])

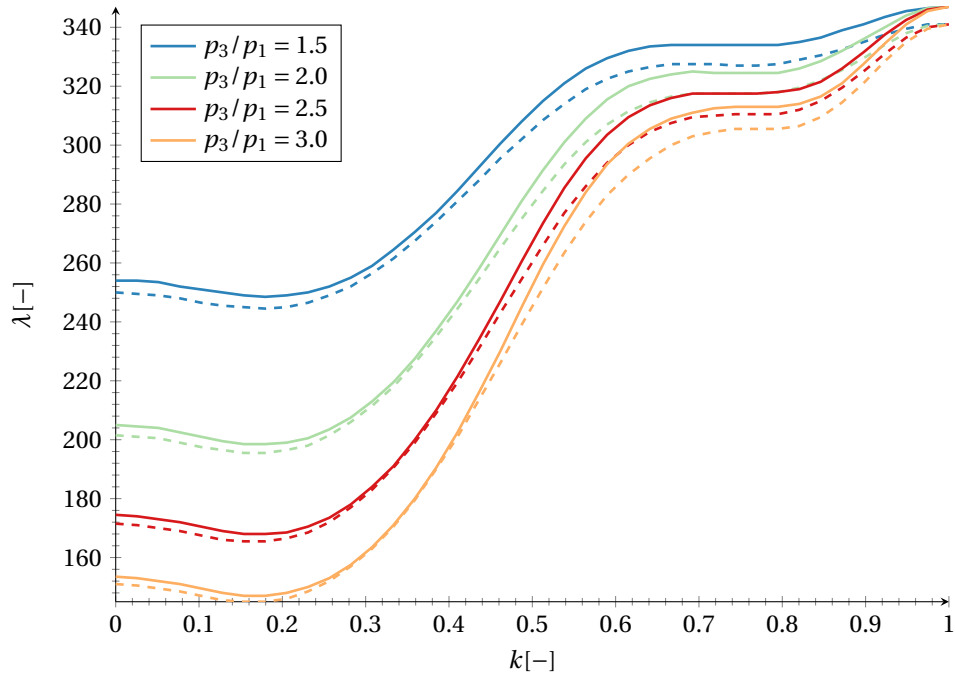


Figure 4.8: Flutter dynamic pressure versus shock impingement location for different shock strengths (— 6 modes - - 4 modes)

where the slope of the deformed solution is readily obtainable in function of the modal amplitudes:

$$\frac{\partial W}{\partial \xi} = \sum_i^N q_{i,eq} i\pi \cos(i\pi\xi). \quad (4.41)$$

Thus, the pressure distribution over the plate can be easily obtained once the equilibrium amplitudes have been computed. Returning to Fig. 4.12, it can be seen that the pressure jump due to the leading edge shock is nicely predicted by the LiPT. Also the consequent expansion of the flow is predicted rather well, although increasing the dynamic pressure seems to yield a larger error. A significant discrepancy can be observed around the shock location, where the Euler results yield a more smeared-out shock. Compression start around  $\xi \approx 0.4$  and continues in a rather steep fashion up to  $\xi \approx 0.65$ . This yields a higher pressure right in front of the shock and a lower pressure just after the shock. Next to that, a stronger compression can be observed downstream of the shock (around  $0.6 \leq \xi \leq 0.8$ ), which the author argues could be contributed to the Euler equations predicting a stronger compression in the convex part of the plate. Both methods converge again towards the trailing edge.

For a stronger shock, the discrepancies between the two methods increase. LiPT predicts a significantly larger deflection, which can be observed for all shock locations. Surprisingly, this yields a reduced expansion in front of the shock and a reduced compression downstream of the shock, as shown in Fig. 4.13. The author argues this can be attributed to flow nonlinearities not being taken into account, underestimating the flow expansion and compression due to the plate curvature. Most likely, better results would be obtained with the inclusion of higher order piston theory terms. On the other hand, velocity gradients seem to be large enough to argue that the locality of piston theory is not valid anymore, i.e. the Mach number at each piston location now depends on the Mach number of the previous station. Thus, using linear piston theory with  $\beta$  based on the freestream Mach number everywhere could introduce a significant error. Looking at Fig. 4.10, similar errors can be observed for varying shock locations: the deflection obtained with LiPT is a vertically stretched version of the Euler results.

Looking at Fig. 4.11, it can be observed that the x-location of the upward peak seems to move towards the leading edge with increasing shock strength. Looking again at Fig. 4.10, this seems to correspond to the shock impingement point moving towards the leading edge. To verify if this is the case, some preliminary shock-shock interaction calculations are done. This boils down to solving an Edney Type 1 shock-shock interference [Ben-Dor, 2007]. It is decided to have a closer look at the  $p_3/p_1 = 1.8$  case, as a significant discrepancy is obtained there. The resulting shock system is illustrated in Fig. 4.14, where the dashed lines indicate the shocks without any interference effects. Note that the deflection of the plate has been scaled by a factor 10 to make the drawing more clear and that  $p_3$  no longer represents the post shock system state, but rather the post incident shock state. Key values associated to Fig. 4.14 are summarised in Table 4.2, where the values for a shock system pressure ratio of 1.2 are added as well. These have been obtained as follows. The strength  $p_1/p_\infty$  and angle  $\sigma_1$  of the leading edge shock are determined from the panel slope at the leading edge, while the incident shock characteristics correspond to the shock that would generate the desired pressure ratio in a perfect regular reflection shock system. The angles  $\sigma_4$  and  $\sigma_3$  of the refracted leading edge and incident shocks respectively can be obtained by noting that the flow angles and static pressures in states 3 and 4 must match. These requirements can be written as:

$$\vartheta_1 + \vartheta_3 = \vartheta_2 + \vartheta_4, \quad (4.42)$$

$$\frac{p_1}{p_\infty} \frac{p_3}{p_1} = \frac{p_2}{p_\infty} \frac{p_4}{p_2}. \quad (4.43)$$

Therefore the correct refracted shock angles can be obtained by iterating over the unknown flow deflection angle  $\vartheta_3$ , which dictates  $\vartheta_4$ , until the pressure ratio's match. Since the flow velocities in 3 and 4 are not identical, a slip line exists (dotted line). Note that all interactions of shocks with the slip line have been ignored here.

First of all, it can be observed that due to a compression in region 1, the impingement shock is refracted towards the leading edge of the panel, moving the impingement point from  $k = 0.5$  to  $k = 0.475$ , a change of 5%. The pressure ratio over the incident shock is not altered significantly though, increasing by about 0.6%. Secondly, if the actual intersection point with the deformed plate is calculated, instead of the flat plate representation, an extra forward shift of 0.6 percent is observed. This is most likely negligible, but since it is very easy to implement in the Python code, it is retained for extra accuracy. Thirdly, it can be seen that the incident shock impinges on a region of the plate where the deflection is significantly downwards. In fact,

the impingement point nearly coincides with the point of maximum negative slope. This alleviates the compression required over the reflected shock, reducing its pressure ratio and angle. To evaluate the significance of this effect, three different levels of detail are considered: reflection assuming no interference effects ('o'), refraction of the incident shock and assuming the shock is reflected on a flat plate ('f'), and lastly refraction of the incident shock and shock reflection on the deformed plate ('d'). It becomes clear that only including the refracted incident shock already yields a reduction in pressure increase over the reflected shock of 9% ( $p_5/p_3|_f = 1.209$  VS  $p_5/p_3|_o = 1.330$ ), while including the deflected state of the panel yields a 16 percent reduction in relative pressure increase. Therefore, the static pressure jump over the entire system is reduced from 1.8 to 1.5. This is not negligible. It must be noted though that in reality the Mach number right in front of the shock reflection will be higher due to the flow being expanded over the concave part of the plate, which will slightly increase the strength of the reflected shock again.

A couple of things can be concluded. First of all, shock movement due to shock-shock interference is negligible considering its effect on the impinging shock. The reflected shock strength does respond strongly to this small difference, significantly lowering the pressure jump over the reflected shock. It must be noted though that in reality the shift in  $x_{imp}$  will be smaller due to expansion waves curving the leading edge shock down, lowering the location of the shock-shock interference point. Secondly, the pressure jump at the predicted shock impingement location was found to depend strongly on local plate deflection, with as a result a strong reduction in discrete pressure jump at the impingement point. All these effects tend to change the pressure distribution over the panel, and therefore also the local pressure difference (since the bottom pressure is dictated by the theoretical pressure jump over the IR system).

	$\frac{p_3}{p_1} [-]$		$\frac{p_5}{p_3} [-]$			$k [-]$			$\frac{p_5}{p_1} [-]$	
	'o'	'd'	'o'	'f'	'd'	'o'	'f'	'd'	'f'	'd'
$\left(\frac{p_5}{p_1}\right)_o = 1.8$	1.353	1.345	1.330	1.209	1.114	0.500	0.475	0.472	1.626	1.500
$\left(\frac{p_5}{p_1}\right)_o = 1.2$	1.096	1.095	1.094	1.029	1.019	0.500	0.483	0.479	1.127	1.116

Table 4.2: Pressure ratio's and shock impingement locations obtained with different simplifications of the shock system ( $\lambda^* = 875$ ). 'o': shock reflection without shock-shock interference, 'f': only leading edge plate deflection taken into account, 'd': full deformed plate taken into account

Since it is now clear how the steady deformation and its resulting pressure distribution behaves, the **behaviour of the flutter boundary** can be verified and explained. Looking at Fig. 4.15, it becomes clear that linearising around the steady deformed solution yields a rapid increase in flutter dynamic pressure with increasing shock strength. For very small shock strengths up to about  $p_3/p_1 = 1.05$ , a smooth but fast increase in  $\lambda_{flut}$  is observed. If the pressure ratio over the shock system is increased, a more linear behaviour of the flutter boundary is obtained. The author believes this sudden shift in trend can be attributed to the deformed shape shifting from a first mode deformation to a deformation with more second mode participation. This is illustrated in Fig. 4.16, where each line corresponds to a flutter point, indicated by the dots in Fig. 4.15. Indeed, from the fifth point on, the deflection close to the trailing edge starts to decrease instead of increase, which could explain the different flutter behaviour.

Interestingly, the mean solution at the flutter point differs significantly from the one obtained by Visbal for flutter around those pressure ratio's, as shown for example in Fig. 4.11. This can be attributed to LiPT predicting flutter at much higher dynamic pressures. Since  $\lambda$  is significantly higher and the shock strength is identical, the mean deflections obtained with LiPT contain much more first mode content. This behaviour increases with dynamic pressure. It can thus be concluded that the effect of a higher shock strength is to increase steady second mode participation, while a higher dynamic pressure will result in more first mode content.

Considering the earlier observed behaviour of the plate steady deformation, it comes as no surprise that the linear stability of the deformed mean state yields an erroneous flutter dynamic pressure. The author argues that due to the nonlinear behaviour of the flow and the large amplitudes associated with flutter, the linear method cannot possibly predict the flutter point. As a result, the mean upward peak keeps growing with increased dynamic pressure, continuously increasing the stiffness of the system. This yields an ever increasing flutter dynamic pressure with increasing shock strength, proving that the sudden drop of the flutter

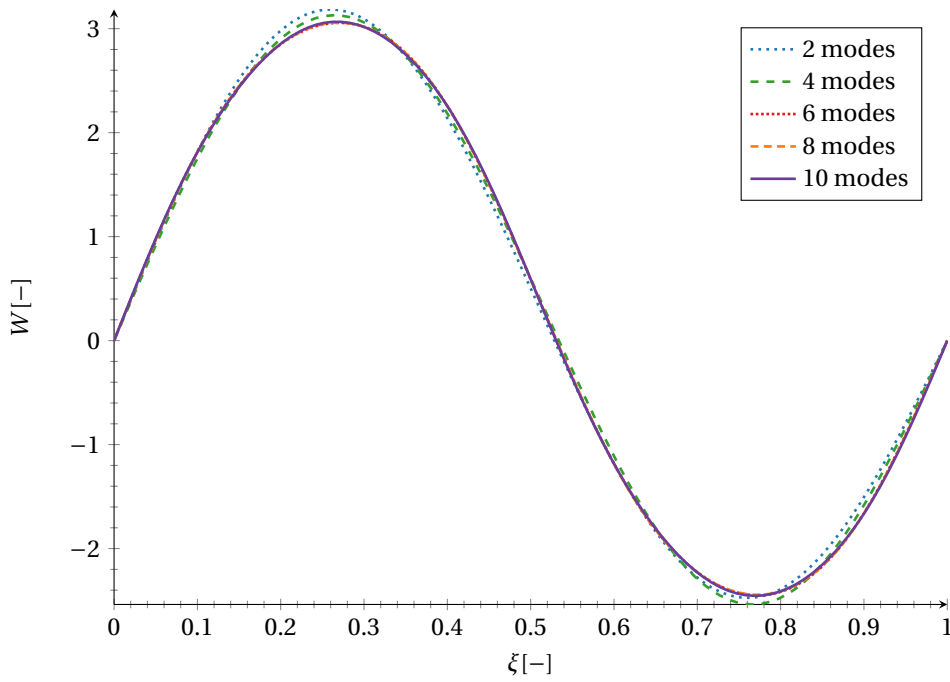


Figure 4.9: Deformed equilibrium solutions for different amounts of modes ( $k = 0.5$ ,  $p_3/p_1 = 1.8$ ,  $M = 2.0$ ,  $\lambda^* = 875$ )

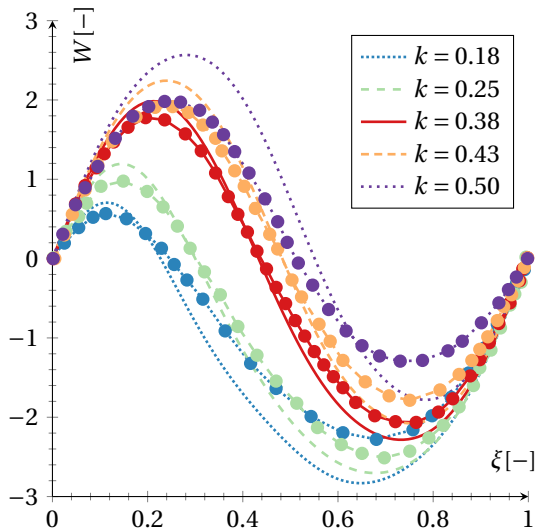


Figure 4.10: Deformed equilibrium solutions for different shock impingement points ( $p_3/p_1 = 1.8$ ,  $M = 2.0$ ,  $\lambda^* = 875$ , —LiPT - von Kármán —●—Euler - von Kármán [Visbal, 2014])

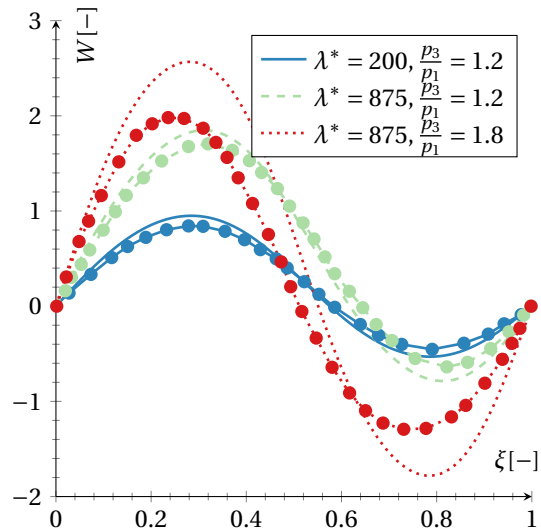


Figure 4.11: Deformed equilibrium solutions for different dynamic pressures and shock strengths ( $k = 0.5$ ,  $p_3/p_1 = 1.2$ ,  $M = 2.0$ , —LiPT - von Kármán —●—Euler - von Kármán [Visbal, 2014])

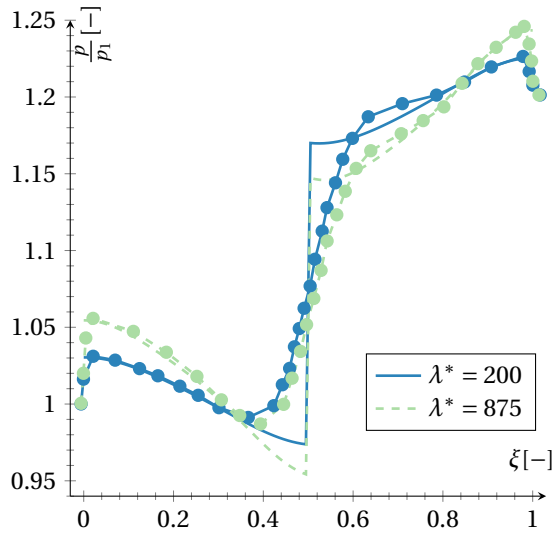


Figure 4.12: Equilibrium upper pressure distribution for  $p_3/p_1 = 1.2$ ,  $M = 2.0$  and  $k = 0.5$ . — LiPT - von Kármán — Euler - von Kármán (Visbal, 2014)

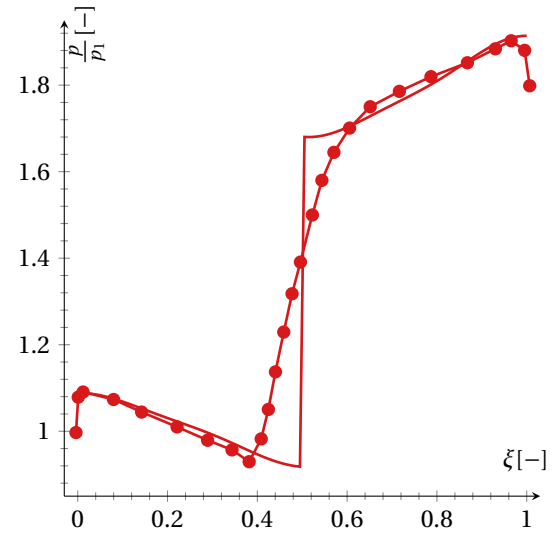


Figure 4.13: Equilibrium upper pressure distribution for  $p_3/p_1 = 1.8$ ,  $\lambda^* = 875$ ,  $M = 2.0$  and  $k = 0.5$ . — LiPT - von Kármán — Euler - von Kármán (Visbal, 2014)

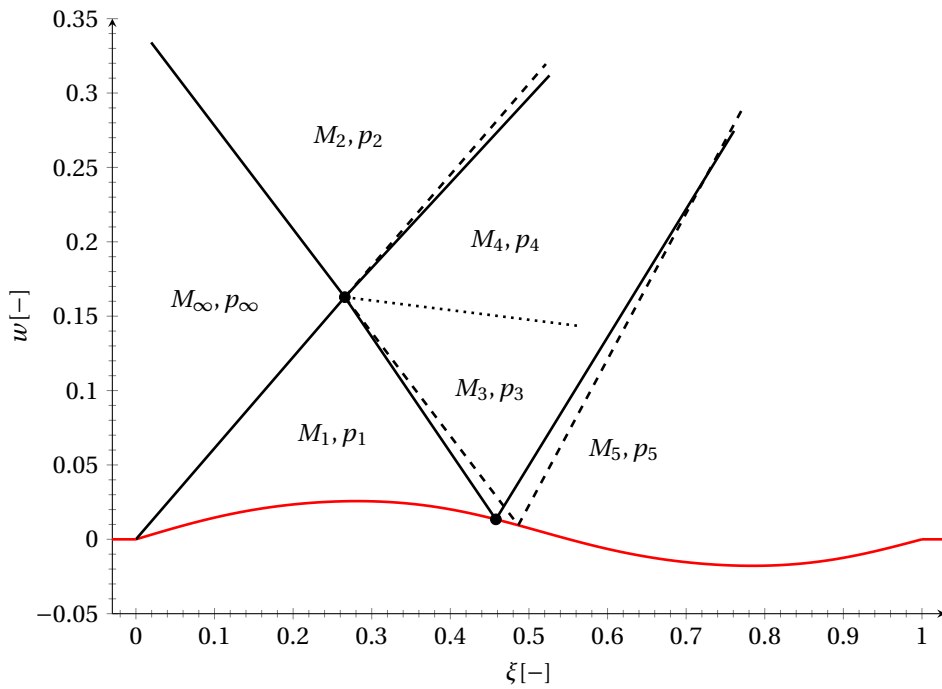


Figure 4.14: Effect of shock-shock interference on shock impingement location

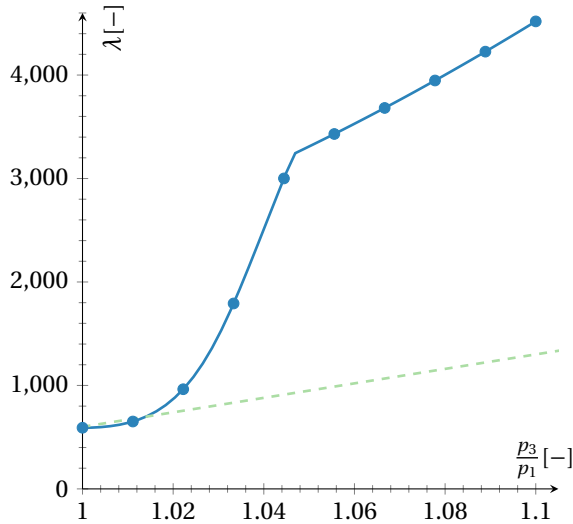


Figure 4.15: Flutter dynamic pressure for a steady deformed solution versus shock strength for  $M = 2.0$  and  $k = 0.5$  (—LiPT - von Kármán - - -Euler - von Kármán [Visbal, 2014])

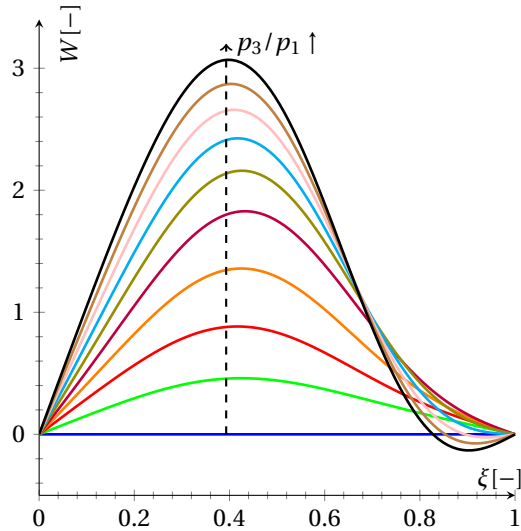


Figure 4.16: Mean deformed panel shapes at the flutter point for different shock strengths ( $k = 0.5$ ,  $M = 2.0$ )

boundary is an inherently nonlinear effect.

On the other hand, the current LiPT method of starting from the flat plate solution, increasing the dynamic pressure with a certain step, calculating the steady deformed solution, calculation the stability of the deformed shape, and repeating this till flutter is observed, corresponds to one of the two initial conditions employed by Visbal, i.e. increasing lambda from a previous steady-deflected solution. For this initial condition, Visbal also did not obtain a dynamic instability for  $p_3/p_1 = 1.4$ . Flutter was only observed by starting from the rigid plate initial condition. This initial condition cannot be implemented correctly using LiPT though, since consequent steady deformations will not be resolved. Thus, it is impossible to replicate the subcritical instability observed by Visbal [2014]. A supercritical instability at  $p_3/p_1 = 1.8$  was proven to exist by Visbal though, and this behaviour was also not captured by the linear piston theory. This indicates that the method lacks accuracy, and that the error cannot (solely) be attributed to the initial conditions.

#### 4.2.5. Discussion

Looking at the results presented in the previous sections, a couple of things can be concluded. First of all, the critical dynamic pressure for classical panel flutter can be predicted excellently with both implemented methods, showing good agreement with inviscid CFD results. Stiffening effects introduced by 3D simply-supported and clamped panels can also be estimated accurately with the semi-empirical method of Laurenson and McPherson [1977]. Secondly, the method by Ye and Ye [2018] yields a good prediction of the flutter dynamic pressure for a shock-system pressure ratio of 1.4. For lower shock strengths, the method fails to predict panel stiffening due to a mean, mainly first mode deformation. For higher shock strengths, the sudden supercritical drop in flutter dynamic pressure is completely missed as well. Both errors can be attributed to the mean deformation of the plate not being taken into account, which appears to be the critical difference with classical panel flutter. Looking at the stability of the flat plate with a simple pressure jump at the impingement point is thus not accurate, although it does provide a trend in the correct direction. Since it currently provides the best estimate of the flutter dynamic pressure at low computational cost, the method by Ye and Ye [2018] will be used in the next section to investigate flow parameters for further high fidelity analysis.

Secondly, it is clear that shock impingement leads to mean panel deformations which are too large to justify the use of linear models. Steady deflections on the order of multiple panel thicknesses are observed, which lead to the following nonlinear effects. First of all, a permanent leading edge shock interacts with the impinging shock, causing upstream movement of the shock foot which increases with increased panel deflection. Secondly, the shock impinges on the plate around the point of maximum downward slope, strongly reducing the strength of the reflected shock. This effect seems to be the most significant. Thirdly, for strong shocks, the Mach number variation along the plate is too large to justify the locality of linear piston theory. Therefore,

using only a pre- and post-shock section with constant Mach number results in inaccurate flow compression and expansion. This strong sensitivity of the flowfield on panel deflection means that linear stability analysis based on the eigenvalues of the coupled system is not justified, since the flowfield changes in a nonlinear fashion when deviating from the equilibrium point. Thus, time integration of the governing equation could perhaps provide more insight.

### 4.3. Design of Experiment

As discussed earlier, the goal of this thesis is to provide a validatable set-up for SWTBLI over a flexible plate. Thus, the parameters for the CFD simulation should be chosen such that the case is reproducible in the ST-15 supersonic windtunnel of the TU Delft faculty of Aerospace Engineering. An introduction to the windtunnel characteristics was already given in Section 1.3. Based on those specifications and analytical results, preliminary insights considering the choice of flow and structural parameters are given here.

Looking at Section 1.3, it becomes clear that a large range of total pressure can be handled in the ST-15 wind-tunnel. It must be noted though that the maximum total pressure for PIV measurements is 4.0 bar, since higher pressures in combination with oil-based bubbles could be dangerous. Since for classical panel flutter it is known that the flutter behaviour becomes more complex when  $M < 2.0$ , it is decided to go for a **Mach number** of 2.0. This will steer away from single mode flutter and ensures an acceptable  $P_0$  for PIV. Next to that, as can be clearly seen in Fig. 3.1, higher Mach numbers will lead to higher flutter dynamic pressures, smaller flutter amplitudes and reduced flutter frequencies. An increased flutter dynamic pressure is undesirable, since the dynamic pressure in the test section is limited by the total pressure in the settling chamber. Secondly, the reduction in flutter amplitude could pose problems for wind tunnel measurements. Another reason for this choice of Mach number is the possibility to compare computations with the results of Visbal [2012], Visbal [2014] and Boyer et al. [2018].

As discussed in Section 3.3, the spanwise panel edges should be left free to ensure semi-2D behaviour of the panel and pressure equalisation with the test section. Thus, the **cavity pressure** is set to the spatial average of the theoretical oblique shock reflection on the upper surface, i.e Eq. (3.1). Since it was shown that the analytical model cannot predict the sudden damping of all panel motion for certain shock positions upstream of the panel midpoint,  $k = 0.50$  is assumed for now.

The dominant structural parameter  $\lambda$ , which is the output of the analytical model, can be transformed back to the dimensional dynamic pressure  $q$  by assuming several parameters, as shown by Eq. (3.4). It becomes clear that two material parameters define the dimensional dynamic pressure: Young's modulus  $E_s$  and the Poisson ratio  $\nu_s$ . Both are determined by selecting a certain **material**. The author argues that Aluminium Al7075-T6 is a good choice, since it provides a relatively flexible plate at a high yield stress of  $503 \times 10^6$  Pa. This should provide larger deflections and a lower flutter dynamic pressure compared to stiffer materials used in previous similar wind tunnel tests and high fidelity computations, e.g. CK 75 spring steel [Daub et al., 2015b; Pasquariello et al., 2015] or ANSI 4130 Alloy Steel [Gan and Zha, 2016; Gogulapati et al., 2014; Spottswood et al., 2013].

Using the implemented analytical model, a strong dependency of the dimensional flutter dynamic pressure was found on panel **thickness-to-length** ratio, as shown in Fig. 4.17 for varying **shock strength** and along with the estimated available dynamic pressure in the tunnel for different total pressures in the settling chamber. The original Euler results by Visbal [2014] have been included as well, indicated by the blue circular markers. The Euler results have first of all been scaled to a higher  $h/a$  as well, indicated by the green line. As discussed before, some error might be introduced here since it is argued the effect of  $h/a$  is not completely encapsulated in the nondimensional dynamic pressure anymore. Secondly, The high-fidelity flutter boundaries have also been scaled to account for clamped B.C. (dashed lines), based on the results by Laurenson and McPherson [1977]. They observed a 77% increase in flutter dynamic pressure for all  $a/b$ . Whether this is extrapolatable to the case with an impinging shock remains unclear, but it was argued earlier in this chapter that nonlinear flow effects will most likely introduce more complex behaviour than predicted in the classical case. Lastly, analytical flutter boundary predictions are indicated by the solid black lines.

After discussions with a fellow thesis student and investigation of earlier experiments conducted in the ST-15, a feasible range of panel thicknesses was established:  $0.2\text{mm} \leq h \leq 0.5\text{mm}$ . Smaller thickness will be

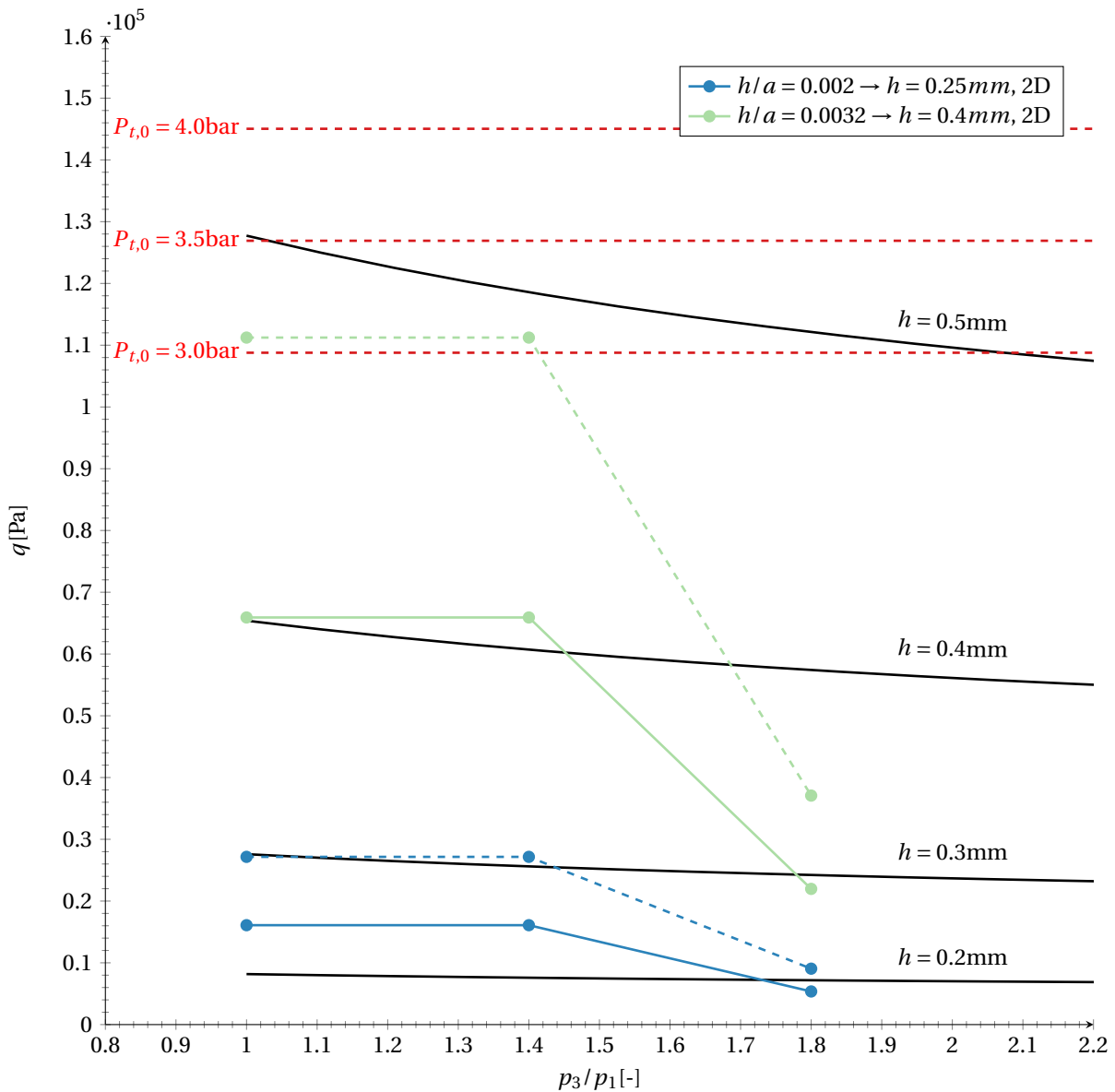


Figure 4.17: Dimensional dynamic pressure versus shock strength for different  $h/a$  ( $M = 2.0$ , — Simply supported, - - - Clamped)

difficult to manufacture if clamped conditions are desired, since the flexible platen has to be CNC'ed out of a solid block of metal. Next to that, thinner panels could yield during tunnel start-up, due to the passing of the normal shock, or during shut-down, due to the strong temperature drop. Thickness's larger than 0.5 mm will most likely damp all panel motion.

In short, it can be concluded that, if  $p_c$  equals the average of the upper surface pressure, flutter can be expected in the ST-15 tunnel for clamped panels with a thickness of 0.25mm (resembling the conditions investigated by Visbal [2014]). It is argued that if the thickness is increased to 0.4 mm, the 2D clamped high fidelity flutter boundary will also remain under the 3.0 bar line. Both the analytical model and the Euler results indicate the same trends: shock strength should be maximised and panel thickness should be minimised to ensure unstable behaviour. Lastly, it is clear that the total pressure should be kept as high as possible, preferably at 3.5 bars.



# 5

## Numerical Approach

In order to solve the governing equations introduced in Chapter 2, they have to be discretised. The numerical approaches to achieve this goal are highlighted for the fluid and the structure in Section 5.1 and Section 5.2 respectively. Furthermore, the approach to turbulence modelling is touched upon in Section 5.4. Lastly, the coupling algorithm is elaborated on in Section 5.3.

### 5.1. Fluid Discretisation

In order to compute the flow, the flow solver INCA is employed. This is a general-purpose multi-physics CFD solver for high-fidelity DNS and LES, developed at the Technical University of Munich (TUM) and the Technical University of Delft (TUD). It operates on Cartesian grids and discretises the compressible Navier-Stokes equations with a finite volume method. In order to account for the fluid-structure interaction when the fluid is represented on an undeformable cartesian grid, the cut-element Immersed Boundary Method (IBM) of Örley et al. [2015] and Pasquariello et al. [2016] is used. IBM circumvents the typical large structural deformation problems associated with classical Arbitrary Lagrangian Eulerian (ALE) methods and strongly simplifies the CFD mesh generation. To accurately capture shocks, the method by Örley et al. [2015] ensures conservation by reshaping the cut FV cells such that sub-cell resolution of the wetted surface is obtained. This will be elaborated on later in this section. A drawback of IBM is the possible occurrence of arbitrarily small cut-cells, which can lead to numerical instabilities with explicit time integration schemes or to excessively small timesteps. This problem is omitted by employing a stabilisation method based on a conservative mixing procedure [Hu et al., 2006; Meyer et al., 2010; Örley et al., 2015].

In Fig. 5.1, a 2D sketch of a typical cut-cell  $\Omega_{i,j,k}$  is shown. Considering Eq. (2.1) and applying the Gauss theorem, the integral form of the governing equation for the flow through such a cut-cell can be written for a single time step  $\Delta t = t^{n+1} - t^n$  as

$$\int_{t^n}^{t^{n+1}} \int_{\Omega_{i,j,k} \cap \Omega_f} \frac{\partial \mathbf{w}}{\partial t} dV dt + \int_{t^n}^{t^{n+1}} \int_{\partial(\Omega_{i,j,k} \cap \Omega_f)} \mathbf{K}(\mathbf{w}) \cdot \mathbf{n} dS dt = 0. \quad (5.1)$$

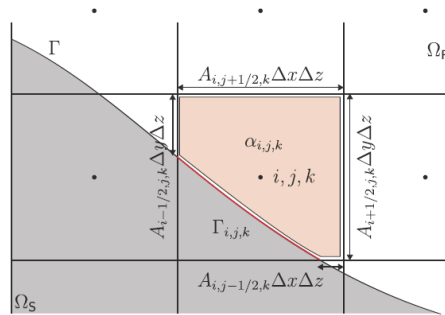


Figure 5.1: Two-dimensional sketch of a typical cut-cell [Pasquariello et al., 2016]

Since the integral is taken over  $\Omega_{i,j,k} \cap \Omega_f$ , only the part of cut-cell  $\Omega_{i,j,k}$  belonging to the fluid sub-domain is considered. Therefore,  $\partial(\Omega_{i,j,k} \cap \Omega_f)$  indicates the wetted surface of  $\Omega_{i,j,k}$ .  $0 \leq \alpha_{i,j,k}$  indicates the fluid volume fraction, while the effective fluid wetted cell face apertures are indicated by  $A_{i,j,k-\frac{1}{2}} \leq 1$ . These values are computed by first triangulating each structural interface element  $\Gamma_s^{(e)}$  as shown in Fig. 5.2 for a quadratic hexahedral element. The resulting individual structural surface elements  $\Gamma_{tri}$  are used as an input for the IBM algorithm, yielding the fluid-solid interfaces  $\Gamma_{ele} = \Gamma_{tri} \cap \Omega_{i,j,k}$ . Since several surfaces can intersect a certain fluid cell, the complete interface is given by  $\Gamma_{i,j,k} = \sum_{ele} \Gamma_{ele}$ . The volume average of the conserved variables for a single cut-cell is given by:

$$\bar{\mathbf{w}}_{i,j,k} = \frac{1}{\alpha_{i,j,k} V_{i,j,k}} \int_{\Omega_{i,j,k} \cap \Omega_f} \mathbf{w} dx dy dz, \quad (5.2)$$

which indicates a forward Euler time integration scheme yields the following discrete form of Eq. (5.1). Note that this corresponds to one sub-step of the employed explicit third-order Runge-Kutta scheme [Gottlieb and Shu, 1998].

$$\begin{aligned} \alpha_{i,j,k}^{n+1} \bar{\mathbf{w}}_{i,j,k}^{n+1} = & \alpha_{i,j,k}^n \bar{\mathbf{w}}_{i,j,k}^n + \frac{\Delta t}{\Delta x_i} \left[ A_{i-1/2,j,k}^n \mathbf{k}_{i-1/2,j,k}^{(1)} - A_{i+1/2,j,k}^n \mathbf{k}_{i+1/2,j,k}^{(1)} \right] \\ & + \frac{\Delta t}{\Delta y_j} \left[ A_{i,j-1/2,k}^n \mathbf{k}_{i,j-1/2,k}^{(2)} - A_{i,j+1/2,k}^n \mathbf{k}_{i,j+1/2,k}^{(2)} \right] \\ & + \frac{\Delta t}{\Delta z_k} \left[ A_{i,j,k-1/2}^n \mathbf{k}_{i,j,k-1/2}^{(3)} - A_{i,j,k+1/2}^n \mathbf{k}_{i,j,k+1/2}^{(3)} \right] \\ & + \frac{\Delta t}{V_{i,j,k}} \chi_{i,j,k} \end{aligned} \quad (5.3)$$

$V_{i,j,k}$  indicates the total volume of cell  $\Omega_{i,j,k}$ . Considering the fluxes,  $\mathbf{k}^{(1)}$ ,  $\mathbf{k}^{(2)}$  and  $\mathbf{k}^{(3)}$  indicate the face-averaged numerical fluxes across the regular cell faces in  $x$ ,  $y$  and  $z$  direction respectively, while in cut-cells the flux over the fluid-structure interface  $\Gamma_{i,j,k}$  is accounted for by an interface exchange term  $\chi_{i,j,k}$ . The latter includes the fluid stresses and the resulting work due to pressure, viscous effects and heat transfer effects, denoted  $\chi^p$ ,  $\chi^v$  and  $\chi^{ht}$  respectively. Accounting for multiple cut-elements, the exchange term can be written as

$$\chi_{i,j,k} = \sum_{ele} \left( \chi_{ele}^p + \chi_{ele}^v + \chi_{ele}^{ht} \right). \quad (5.4)$$

For a more in-depth description of the cut-element IBM method and the exchange term contributions, the reader is referred to the work by Örley et al. [2015] and Pasquariello et al. [2016].

In order to avoid modifying the interpolation stencils in the FV reconstruction scheme, uncut fluid cells in the solid subdomain near the FSI interface contain ghost fluid states. These are employed to impose boundary conditions at the interface. The ghost-cell methodology for stationary and moving boundary compressible cut-cell methods by Pasquariello et al. [2013, 2016] is used, which is an extended version of the incompressible method by Mittal et al. [2008].

The spatial fluxes are computed using either the Adaptive Locals Deconvolution Method (ALDM) or a 3<sup>rd</sup>-order Weighted Essentially Non-Oscillatory (WENO) scheme based on the HLLC Riemann solver. The former is outlined in Section 5.3 and is employed to solve the full Navier-Stokes equations, while the latter is used for the 2D inviscid computations.

## 5.2. Structure Discretisation

The free three-dimensional structural Finite Element program Calculix is selected to solve Eq. (2.10) with the Finite Element Method (FEM). The governing equation is cast in its weak form using the principle of virtual work. Assuming virtual displacements  $\delta \mathbf{d}$ , integrating over the solid and employing Gauss's theorem yields:

$$\int_{\Omega_s} (\rho_{s,0} \dot{\mathbf{d}} \cdot \delta \mathbf{d} + \text{tr}(\mathbf{S} \cdot \delta \mathbf{E}) - \hat{\mathbf{b}}_0 \cdot \delta \mathbf{d}) dV_0 - \int_{\Gamma_{s;N}} \hat{\mathbf{t}}_0 \cdot \delta \mathbf{d} dA_0 - \partial \mathcal{W}_s^\Gamma = 0. \quad (5.5)$$

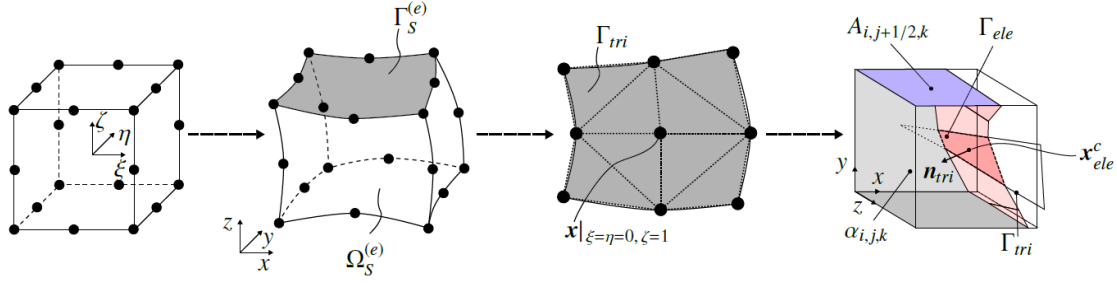


Figure 5.2: Sketch of the triangulation procedure of a structural interface elements  $\Gamma_S^{(e)}$  and the consequent use of the interface triangles  $\Gamma_{tri}$  by the cut-algorithm [Thari et al., 2017]

In Eq. (5.5),  $dA_0$  and  $dV_0$  represent infinitesimal volume and surface elements respectively, while  $\delta \mathcal{W}_S^\Gamma$  denotes the virtual work at the fluid-solid interface.  $\delta \mathbf{E}$  can be obtained from the Green-Lagrange strain tensor, given by Eq. (2.13), resulting in

$$\delta \mathbf{E} = \frac{1}{2} [(\nabla_0 \delta \mathbf{d})^T \cdot \mathbf{G} + \mathbf{G}^T \cdot \nabla_0 \delta \mathbf{d}]. \quad (5.6)$$

The FEM is employed to discretise Eq. (5.5) in space. The structural sub-domain is decomposed into  $n^e$  solid elements  $\Omega_S^{(e)}$ , each with associated constant shape functions to allow an approximation of the displacement field. Assembling the contributions of all elements  $\Omega_S^{(e)}$  yields the following semi-discrete form of Eq. (5.5):

$$\mathbf{M} \ddot{\mathbf{d}} + \mathbf{f}_{s,int}(\mathbf{d}) - \mathbf{f}_{s,ext}(\mathbf{d}) - \mathbf{f}_s^\Gamma = \mathbf{0}, \quad (5.7)$$

where  $\mathbf{M}$  is the mass matrix and  $\ddot{\mathbf{d}}$  and  $\mathbf{d}$  are the discrete acceleration and displacement vectors respectively. The forces acting on the structure are split into internal forces, external forces and interface forces resulting from the fluid, denoted by  $\mathbf{f}_{s,int}$ ,  $\mathbf{f}_{s,ext}$  and  $\mathbf{f}_s^\Gamma$  accordingly. To integrate Eq. (5.7) in time, it is discretised with the Hilbert-Hughes-Taylor  $\alpha$ -method [Hilber et al., 1977]. A coupled set of non-linear equations is obtained, which is solved iteratively using the Newton-Raphson method.

### Adaptive Reduced Order Model

In order to reduce the computational cost of solving the structural balance equations, the Adaptive Reduced Order Model (AROM) by Thari et al. [2017] can be employed. It features a repeated linearisation of the governing equations with respect to a full FEM solution, which, based on Eq. (5.7), can be written as

$$\mathbf{M} \delta \ddot{\mathbf{d}} + \mathbf{K}(\mathbf{d}_{ref}) \delta \mathbf{d} = \mathbf{f}_{s,ext} + \mathbf{f}_s^\Gamma - \mathbf{f}_{s,int}(\mathbf{d}_{ref}). \quad (5.8)$$

In Eq. (5.8),  $\delta \mathbf{d} = \mathbf{d} - \mathbf{d}_{ref}$  is the deflection with respect to the reference state  $\mathbf{d}_{ref}$ , obtained with the FEM. The Jacobian of the internal forces  $\mathbf{K}$  is given by

$$\mathbf{K}(\mathbf{d}_{ref}) = \frac{\partial \mathbf{f}_{s,int}(\mathbf{d}_{ref})}{\partial \mathbf{d}}. \quad (5.9)$$

In order to further increase computational efficiency, the order of the model is reduced by shrinking the system of equations based on the mode superposition method [Dowell and Hall, 2001]. To achieve this, Eq. (5.8) is transformed from physical to modal space using

$$\delta \mathbf{d} = \Phi \delta \mathbf{q}, \quad (5.10)$$

where  $\delta \mathbf{q}$  indicate the vector of perturbations expressed in modal amplitudes and  $\Phi$  denotes the vector of orthonormalized eigenvectors obtained by solving

$$\mathbf{K}(\mathbf{d}_{ref}) \Phi = \mathbf{M} \Phi \Omega^2. \quad (5.11)$$

For more information on how to solve the resulting equations, the reader is referred to the work by Thari et al. [2017]. Note that in this work, 10 eigenmodes are always used to ensure convergence. The Modal Truncation Augmentation (MTA) method [Dickens et al., 1997] is also employed to improve the representation of the spatial load vector in the modal domain. This is achieved by adding pseudo eigenvectors to the original modal

basis  $\Phi$  in order to minimize the projection error from the physical to the modal domain.

Since a linearised model is used, the structural properties computed by the FEM are only valid for small deflections. In order to account for large nonlinear deformations, the reference FEM solution has to be updated accordingly. Thari et al. [2017] proposed a threshold value  $\epsilon$ , based on a certain maximum absolute deflection  $|\delta d_{max}|$  with respect to the most recent reference frame, after which a new FEM discretisation has to be computed. It is given by

$$\epsilon = \frac{|\delta d_{max}|}{a}. \quad (5.12)$$

Thus, if a re-computation of the reference state is desired after  $x$  panel thicknesses, the non-dimensional parameter can be written as

$$\epsilon = x \frac{h}{a}. \quad (5.13)$$

### 5.3. Coupling

The fluid and structure are loosely coupled using a conventional serial staggered algorithm, as shown in Fig. 5.3. It follows the classical Dirichlet-Neumann partitioning, where in this case the fluid imposes tractions on the FSI interface  $\Gamma$  as a Neumann boundary condition, while the solid takes the Dirichlet part by enforcing kinematic constraints. Loosely coupled approaches are often employed in the field of compressible aeroelasticity [Cirak et al., 2007; Farhat and Lesoinne, 2000; Farhat et al., 2006; Karagiozis et al., 2011], since the added mass effect is negligible due to the small mass ratio  $\mathcal{M}$  [Causin et al., 2005]. The steps taken to advance the system from time  $t^n$  to  $t^{n+}$  can be summarised as follows:

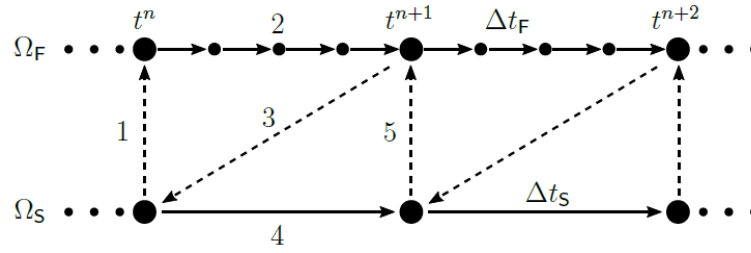


Figure 5.3: Schematic of the staggered coupling algorithm with optional fluid subcycling [Pasquariello, 2018]

1. First, the structural displacements  $\mathbf{d}^{\Gamma;n}$  and velocities  $\dot{\mathbf{d}}^{\Gamma;n}$  at timestep  $t^n$  are transferred to INCA as a Dirichlet boundary condition. The cut-cell geometry is updated accordingly, yielding new triangulated surface elements  $\Gamma_{tri}$ . These are used as an input for the IBM-algorithm.
2. The flowsolver advances the fluid, i.e. Eq. (5.3), to the next timestep  $t^{n+1}$ , with optional subcycling. The given structural velocities  $\dot{\mathbf{d}}^{\Gamma;n}$  at the previous timestep  $t^n$  are used by the interface exchange terms  $\chi_{i,j,k}$  and the ghost-cell method. Since these velocities are required at the face centroids of the cut-elements, interpolation is necessary.
3. The fluid interface tractions  $\boldsymbol{\sigma}_f^{\Gamma;n+1} \cdot \mathbf{n}^{\Gamma;n}$  computed in step 2 are transferred to CalculiX. Again, interpolation is required.
4. The structural solver advances the structural system, Eq. (5.7), in time. The fluid tractions projected in step 3 are imposed on the solid as additional Neumann boundary conditions.
5. Repeat steps 1-4 for the next timestep.

Since the staggered algorithm introduces a one timestep lag between the structural and fluid subdomains, the coupling algorithm is first-order accurate in time [Farhat et al., 1995]. As mentioned in steps 2 and 3, the cut-cell IBM inevitably leads to non-matching grids at the FSI interface, thus requiring interpolation methods for the load transfer between the structure and the fluid. The simple but efficient projection-based method

by Farhat et al. [1998] is employed, which uses the FE shape functions to interpolate the fluid loads on the nearest structural nodes. The transfer of the solid motion to the fluid is implicitly accounted for by the cut-cell IBM, thus eliminating the need for explicit interpolation in that step. It has been proven recently by Thari et al. [2017] that accurate results can be obtained with this projection-based approach when applied to the FSI test-cases presented by Pasquariello et al. [2016], including classic panel flutter.

## 5.4. Turbulence Modelling

As discussed in Chapter 1, LES entails a spatial filtering of the velocity field. Large energetic eddies are fully resolved, while small turbulent structures are modelled. The latter can be justified by noting that small scales depend less on the geometry, and thus tend more towards isotropic, universal behaviour. When the Navier-Stokes equations are solved numerically, scale separation is inherently introduced by a finite computational grid and the discretisation of continuous operators. The latter introduces a numerical discretisation error, which can interfere with the represented non-resolved scales [Garnier et al., 2009]. From a mathematical point of view, separating the scales boils down to convoluting the governing equations with a filter kernel [Leonard, 1975]. A filtering of the nonlinear terms of the Navier-Stokes equations yields unclosed subgrid scale tensors, which thus have to be modelled.

The introduction of unclosed terms leads to two possible SGS models. In *explicit* LES, explicit model terms are added to the underlying conservation law to account for the effect of the subgrid scales on the resolved flow, after which the equations are discretised. A major assumption made here is that artificial numerical dissipation does not interfere with the turbulence model. Often, this does not hold, as Vreman et al. [1995] and Kravchenko and Moin [1997] have proven that even the truncation error of high-order centred discretisations can be on the order of magnitude of the subgrid terms. This problem can be circumvented by employing *implicit* LES (ILES), which solves the unmodified governing equations in such a way that the numerical dissipation introduced by the truncation error acts as an explicit SGS model.

A general systematic framework for ILES is the Adaptive Local Deconvolution Method (ALDM), developed for incompressible [Adams et al., 2004; Hickel et al., 2006] and compressible turbulence [Hickel et al., 2014]. ALDM is a nonlinear finite-volume scheme which replicates the essential elements of explicit LES, i.e. filtering and convolution, by employing a numerical flux function and a solution-adaptive deconvolution operator. The latter is nonlinear, in contrast to other explicit deconvolution-type SGS models [Domaradzki and Adams, 2002; Geurts, 1997; Kuerten et al., 1999; Stolz and Adams, 1999]. The numerical flux function accounts for compressibility effects and ensures good shock-capturing properties. The model parameters of ALDM, i.e. deconvolution parameters and flux regularization parameters, are selected in such a way that the discretisation error behaves as a physically motivated explicit SGS model. Based on the hypothesis that the main task of a SGS model is to yield the correct dissipation and diffusion spectra of the resolved scales by interaction with the modelled SGS stresses, *a posteriori* analysis of freely decaying Homogenous Isotropic Turbulence (HIT) has been employed to calibrate the deconvolution parameters [Hickel and Larsson, 2008; Hickel et al., 2006, 2007].



# 6

## Two-Dimensional Inviscid Analysis

Since well-resolved long time-integration viscous simulations of shock-panel interactions are extremely expensive [Pasquariello et al., 2015, 2017], two-dimensional inviscid interactions are first examined. This allows to identify the aerodynamic and structural parameters at which flutter in the ST-15 windtunnel can be expected. Indeed, it has been shown that in the case of a laminar boundary layer, flutter will occur if it does in the inviscid sense, albeit with a reduced mean deflection [Boyer et al., 2016; Visbal, 2014]. No correlation between inviscid interactions and coupled SWTBLI is available in literature, but it was found that the shock-wave/turbulent boundary-layer interaction adapts passively to the panel motion [Pasquariello et al., 2015]. It is therefore argued that flutter will also occur when a turbulent boundary layer is present, if it has been shown that the plate is unstable when subject to an inviscid flow at identical conditions.

First, the computational set-up is illustrated in Section 6.1, after which the postprocessing methodology is introduced in Section 6.2. Next, the results for the inviscid shock-panel interactions are presented in Section 6.3, after which values for the governing parameters described in Chapter 3 are selected for further high fidelity analysis by LES in Section 7.1.

### 6.1. Numerical Set-up, Boundary Conditions and Grid Distribution

The setup employed for the 2D inviscid simulations is shown schematically in Fig. 6.1. Note that the extent of the computational domain is indicated by the dashed lines. A flexible plate of thickness  $h$  and length  $a$  is constrained at both the leading and trailing edge, and is subject to an inviscid flow entering the domain at a Mach number  $M_1$  of 2.0. Note that  $a = 0.5$  m is selected here, corresponding to the set-up employed by Thari et al. [2017]. This does not correspond to the ST-15 maximum panel length of  $10 \times 10^{-2}$  m, but since nondimensional results will be presented, this does not matter for the inviscid results. The test section variables specified at the inlet depend on the chosen settling chamber conditions, which again depend on the limits of the ST-15 windtunnel, as introduced in Section 1.3. The test section static pressure  $p_1$  and density  $\rho_1$  are given in Table 6.1 for different feasible settling chamber total pressures  $p_{t,0}$ . Note that a settling chamber total temperature  $T_{t,0}$  of 288.15 K is assumed, yielding a test section static temperature  $T_1$  of 160.08 K. Secondly, it must be noted that a total pressure above 4.0 bar is undesirable, since future PIV measurements could become dangerous when combining such high pressures with oil-based bubbles. Considering the plate material, Aluminium 7075-T6 is selected for a high yield strength of  $\sigma_y = 503 \times 10^6$  Pa in combination with a relatively low Young's modulus of  $E_s = 71.7 \times 10^9$  Pa. Furthermore, the panel has a Poisson's ratio of  $\nu_s = 0.33$  and a density of  $\rho_s = 2.800 \text{ kgm}^{-3}$ .

The aerodynamic boundary conditions are specified as follows. Since supersonic flow is expected in the entire fluid domain (oblique shocks only), inflow conditions only have to be specified at the inlet and at upper boundary where the impinging shock and wedge trailing edge expansion fan are generated. The shock and expansion fan are imposed at the boundary as if generated by a wedge with a chosen wedge angle  $\vartheta_w$  and a length  $L_w$  at a given test section Mach number  $M_1$ . The wedge trailing edge is placed specifically above the panel trailing edge in order to prevent any interaction with the impinging shock and the flowfield above the flexible panel in general. Thus, the wedge length can be defined in order to ensure the shock impinges at the

$p_{t,0}$ [bar]	$p_1$ [Pa]	$\rho_1$ [kg/m <sup>3</sup> ]
3.5	45,324	0.9863
4.0	51,799	1.1272
4.5	58,274	1.2681

Table 6.1: Test section static conditions for different settling chamber total pressures ( $T_0 = 288.15\text{K}$ ,  $M_1 = 2.0$ )

desired nondimensional impingement point  $k$ . This is illustrated in Fig. 6.1. The shock is imposed by prescribing the appropriate Rankine-Hugoniot conditions, while Prandtl-Meyer expansion theory is employed to create the expansion fan. In this work, the flow deflection over the incident shock is set to  $\vartheta_1 \approx 10.66^\circ$  in order to obtain an inviscid shock-system static pressure jump of 3.0 and a shock angle  $\sigma_1$  of  $40.04^\circ$ . This is close to the maximum incident shock angle which still yields a regular reflection for  $M = 2.0$ , as Matheis and Hickel [2015] already obtained a pocket of subsonic air downstream of the interaction for a flow deflection angle of  $\vartheta = 12^\circ$ . At the outflow patch, linear extrapolation is used. As stated earlier, Riemann Invariant boundary conditions are specified at the upper boundary, while symmetry boundary conditions are employed for the spanwise domain boundaries. Finally, adiabatic slip-wall boundary conditions are prescribed on the remaining boundaries. Loads on the upper side of the panel are obtained from the fluid, while on the bottom side a cavity pressure  $p_c$  is prescribed. The latter is set to the average of the theoretical pressure distribution on the panel upper surface, as given by Eq. (3.1). Considering the boundary conditions of the structure, clamped leading and trailing edges are obtained by constraining both translation and rotation of the boundaries in all dimensions.

Regarding the initial conditions of the structure, two different options are explored. In both cases, an initially flat plate is considered and the appropriate cavity pressure is prescribed on the lower surface of the compliant panel. According to Visbal [2012, 2014], this should always yield the most unstable response. Option one entails immediately releasing the panel while the impinging shock still has to develop from the pressure jump imposed at the upper boundary of the domain. Since the static pressure at the top of the plate will initially equal  $p_1$ , this leads to a relatively long transient involving strong upward deflections of the panel. The second option attempts to reduce the duration of the transient by constraining the flexible panel in all dimensions until the shock system has fully developed. This limits the magnitude of the initial panel deflections, possibly reducing the transient period.

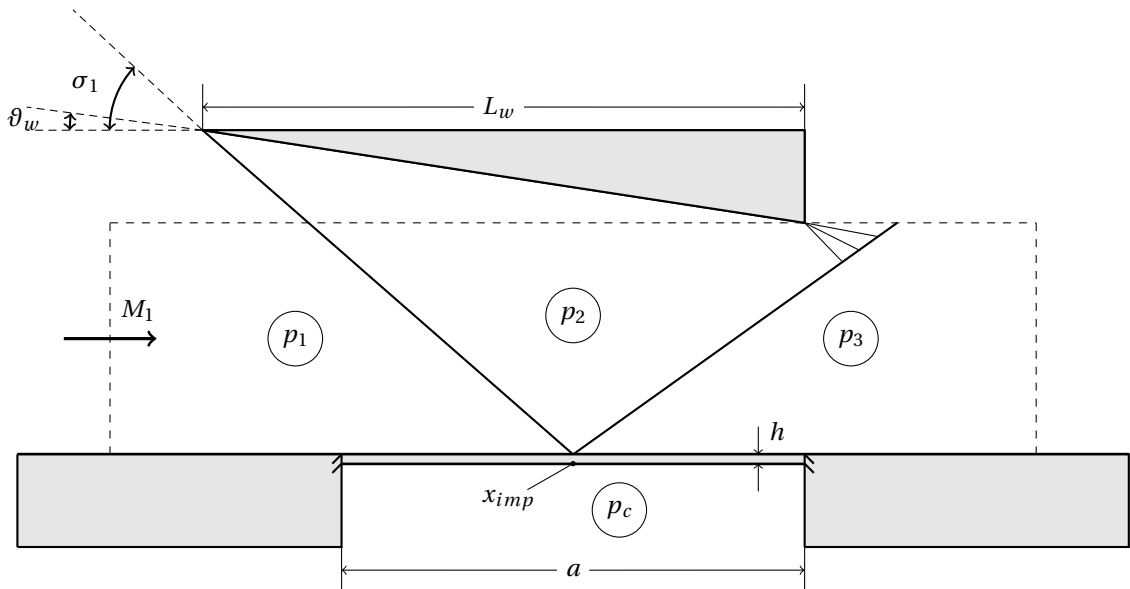


Figure 6.1: Sketch of the 2D inviscid set-up

The fluid and structural subdomains are discretised as illustrated in Fig. 6.2. A uniform spacing in  $x$ -direction consisting of 352 elements, of which 180 above the compliant panel, is employed, yielding  $\Delta x = 2.84 \times 10^{-3}$  m. Close to the panel, a fine uniform spacing with cell size  $\Delta y = 4.81 \times 10^{-4}$  m is selected. Further away from the plate surface, a hyperbolic spacing is prescribed up to the upper domain boundary. Note that the fine mesh below the plate is extended up to  $y = -0.05$  m to account for the panel motion in the IBM framework. The structure is discretised with 196 quadratic hexahedral elements in the  $x$ -direction and two elements in  $y$ -direction. Due to the two-dimensionality of the problem, only one cell in  $z$ -direction is employed for both the structure and fluid meshes.

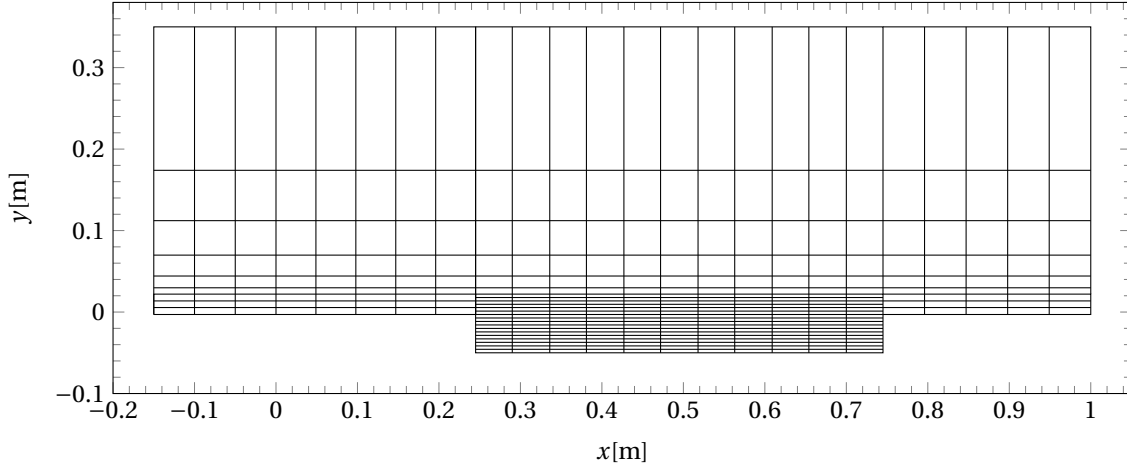


Figure 6.2: Sketch of the fluid mesh - grid lines only to illustrate spacing. Figure adapted from Thari et al. [2017]

## 6.2. Postprocessing Methodology

In order to visualise the results in a concise way and to analyse them, different postprocessing techniques are employed. First of all, the Prony method [Prony, 1795] is employed to analyse the frequency content of the quarter-chord point panel motion. The aim of the method is to represent the temporal signal as a linear sum of damped sines, each with their own initial amplitude  $A_k$ , damping factor  $\alpha_k$ , frequency  $f_k$  and phase  $\theta_k$ . The Prony method attempts to approximate a discrete signal  $x$  based on  $N = 2p$  uniform samples, where in this work  $N$  is always set to the maximum amount of samples available in order to resolve as much frequency content as possible. Note that due to the CFL number affecting the fluid timestep, linear interpolation of the data is performed in order to obtain uniform samples. Numerically, the signal is reconstructed as follows:

$$x[n] = \sum_{k=1}^p A_k e^{j\theta_k} \cdot e^{(\alpha_k + j2\pi f_k)T_s(n-1)}, \quad (6.1)$$

where  $n = 1, \dots, N$  and  $T_s$  is the sampling period. The classical Prony method entails solving a linear system of equations based on an autoregressive model of order  $p$  to obtain the Prony polynomial  $\phi(z)$ . The roots of the characteristic polynomial then yield the damping factors  $\alpha_k$  and frequencies  $f_k$ . Based on the obtained values, the original linear equations can then be solved to obtain the amplitudes  $A_k$  and phase angles  $\theta_k$ . Note that the Prony method only yields accurate results if the sampled signal has converged statistically, thus the transient is always skipped. For an excellent step-by-step guide, the reader is referred to Rodríguez et al. [2018]. Another helpful tool to analyse the panel response is modal analysis. To obtain the relative modal content of the panel deflection in the temporal domain, the eigenmodes of a clamped-clamped Euler-Bernoulli beam are projected on the deflected shape using a least-squares fit. The free-vibration modes are given by [Nilsson and Liu, 2015]:

$$\varphi(x) = \frac{1}{\sqrt{2}} \left[ \cosh \kappa_n x - \cos \kappa_n x - \frac{\cos \kappa_n L - \cosh \kappa_n L}{\sin \kappa_n L - \sinh \kappa_n L} (\sinh \kappa_n x - \sin \kappa_n x) \right], \quad (6.2)$$

where the  $\kappa_n L$  can be obtained from

$$\cos \kappa_n L - \frac{1}{\cosh \kappa_n L} = 0. \quad (6.3)$$

### 6.3. Results

In this section the results obtained with the set-up presented in Section 6.1 are elaborated on. First, the effect of shock impingement location is shown in Section 6.3.1, after which a sensitivity analysis of the response with respect to panel thickness and windtunnel total pressure is executed in Section 6.3.2. Next, the effect of the initial condition on the panel response and suitable settings for the adaptive reduced order model are investigated in Section 6.3.3 and Section 6.3.4 respectively. Lastly, the validity of the nondimensional dynamic pressure as a parameter to characterise the flutter behaviour is discussed in Section 6.3.5.

#### 6.3.1. Effect of Shock Impingement Location

In order to investigate the effect of the inviscid impingement point on the panel response, it is varied from  $k = 0.05$  to  $k = 0.95$  in steps of  $\Delta k = 0.05$ . All other aerodynamic and structural parameters are kept constant at the values given in Section 6.1. The resulting flutter amplitudes and frequencies are given in Fig. 6.3; i.e. the amplitudes and frequencies of the dominant sinusoidal function originating from the Prony decomposition. Note that the panel response at the three-quarter chord point is shown here, analogous to classic panel flutter. In the remainder of the report, this will always be the case unless mentioned otherwise. It becomes clear that two unsteady regions can be identified: close to the panel leading edge, i.e. from  $k = 0.05$  till  $k = 0.20$ , and at and slightly upstream of the panel midpoint, i.e. at  $k = 0.45$  and  $k = 0.50$ . Moving the shock more aft or in between both regions results in damping of all unsteady motion, which was also observed by Visbal [2014] for simply supported panels. In the region close to the leading edge, it can be observed that a more upstream shock impingement point will induce a significant increase in flutter amplitude and a reduction in oscillation frequency. Close to the panel midpoint, the opposite holds: moving the shock closer to the panel leading edge reduces the amplitude of the motion and increases its frequency.

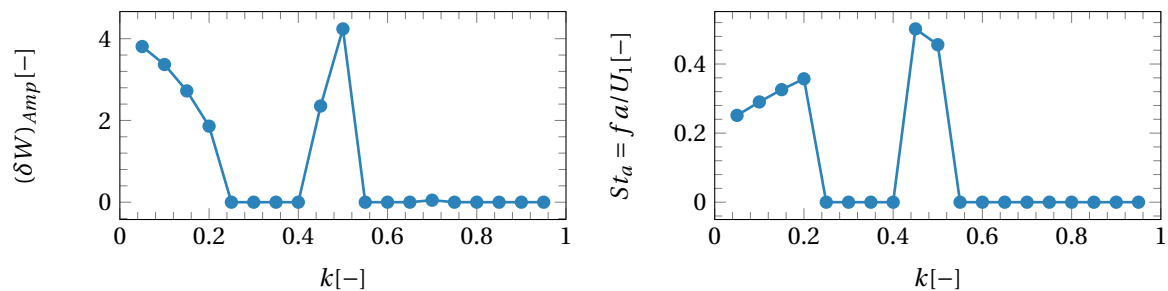


Figure 6.3: Flutter amplitude (left) and frequency (right) versus nondimensional shock impingement location.

Naturally, and by observing the flutter amplitudes and frequencies in Fig. 6.3, it is expected that shock impingement near the leading edge will produce inherently different flutter behaviour compared to the mid-point impingement case. This was the case in the results by Visbal [2014], who observed a strong increase in LCO frequency for shock impingement close to the front of the panel. The opposite can be observed here, yielding a strong significant increase in response amplitude for shock impingement at  $k = 0.05$ . Therefore, the temporal response for three different chordwise impingement points,  $k = 0.05$ ,  $k = 0.15$  and  $k = 0.50$ , is shown in Fig. 6.4. The significant difference in flutter frequencies and amplitudes becomes immediately clear. While the  $k = 0.15$  and  $k = 0.50$  responses look qualitatively similar, the  $k = 0.05$  case shows a distinctly different, less sinusoidal response. As a first step to identify the cause of this discrepancy, the frequency content obtained with the Prony method for the three responses is shown in Fig. 6.5. It can be observed that the spectra for  $k = 0.15$  and  $k = 0.50$  both show one distinct peak at the frequencies shown in Fig. 6.3, except for the static deflection given by the amplitude value at  $St_a = 0$ , while panel impingement very near the leading edge introduces a second, low frequency oscillation. The latter occurs at  $St_a = 0.125$ , half of the frequency of the other peak ( $St_a = 0.250$ ). Smaller peaks in the spectrum can be observed at other harmonics of the fundamental frequency of the first peak, a phenomenon which also occurs for the other impingement points.

To get a feeling for the nature of the panel motion, the mean deflection and deflection bounds for  $k = 0.05$ ,  $k = 0.15$  and  $k = 0.50$  are shown in Fig. 6.6. As expected, shock impingement very near the leading edge produces a rather flat mean deflection, due to the small steady pressure difference existing over the plate. Significant movement of the panel can be observed over its entire length though. Moving the shock more aft to  $k = 0.15$  strongly increases the mean panel deflection, with a dominant downward peak located at the quarter

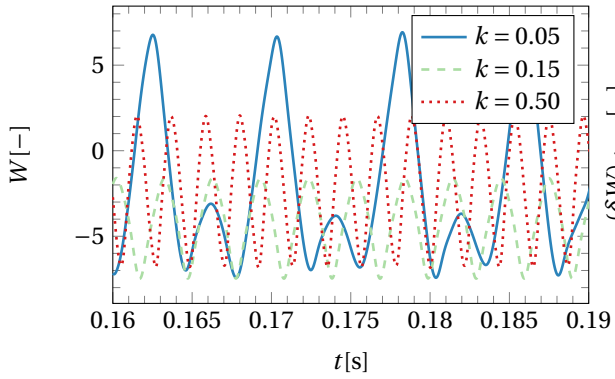


Figure 6.4: Panel responses for different shock impingement locations.

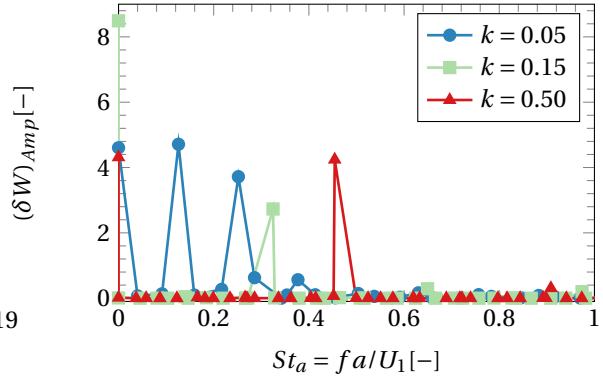


Figure 6.5: Frequency content for the panel responses for different shock impingement locations.

chord point. Panel unsteadiness now seems to be more confined towards the region downstream of the panel midpoint. Finally, shock impingement at the  $k = 0.50$  point yields a typical second mode deformation, with the first upward peak being about 50% higher than the second downward one. Panel motion looks more or less point symmetric around the panel midpoint, although significantly more deviation from the mean panel shape can be seen downstream of the shock impingement point.

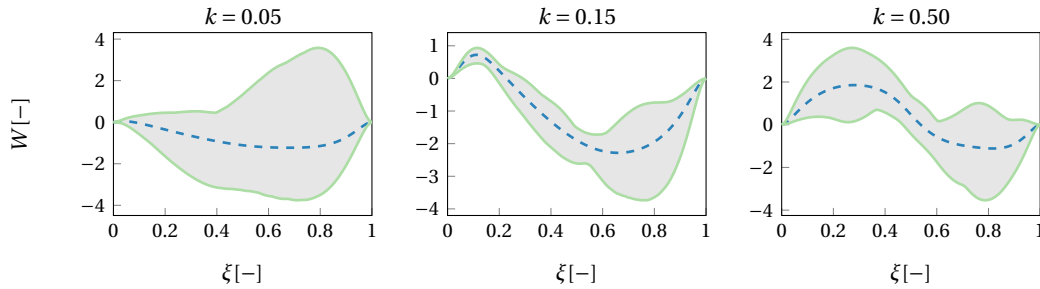


Figure 6.6: Deflection ranges for three different shock impingement points. (—) Deflection bounds, (---) Mean deflection

Another tool which can help understanding the flutter characteristics is modal analysis. Fig. 6.7 shows the progression of the panel deflection's modal content in time for each shock impingement point. Although quantitatively significantly different, the responses for  $k = 0.15$  and  $k = 0.50$  show a qualitatively similar response, as also indicated by Fig. 6.5. A coupling between the second and third mode with a 180 degree phase shift can be observed, with the first mode content mainly indicating the mean downward deflection. The latter is more visible in the  $k = 0.15$  case, as already implied by Fig. 6.6. Shock impingement at the panel midpoint also induces more second mode activity, which can be attributed to the strong asymmetry being introduced into the pressure field by the shock. The response for  $k = 0.05$  on the other hand looks significantly different. A dominant low frequency first mode response can now be observed, which explains the first peak in Fig. 6.5. Its frequency is exactly half of the high frequency second mode oscillation. This dominant first mode content is attributed to the shock impinging almost upstream of the panel, introducing only a slight asymmetry into the steady pressure difference over the panel.

To clarify why significantly different flutter responses occur for different shock impingement locations, RMS pressure contour plots and instantaneous wall-pressure fluctuations in time are shown in Fig. 6.8. RMS values have been obtained by taking the square root of the squared pressure-fluctuation field, averaged over 100 non-dimensional timesteps  $t^* = tU/a$ . Looking at the RMS contour plots for the different shock impingement points, multiple key areas can be identified. Concerning the source of unsteadiness, the reflected shock separates the upstream flowfield from the more unsteady downstream section of the panel. This can also be clearly seen in the temporal evolution of the wall-pressure fluctuations (Figs. 6.8(b), 6.8(d) and 6.8(f)) and was already predicted earlier after examination of the deflection bounds given by Fig. 6.4. Another interesting observation is the fact that the reflected shock shows a significant flapping motion, especially for shock impingement at the panel midpoint. This can be attributed to the local change in panel slope at the shock

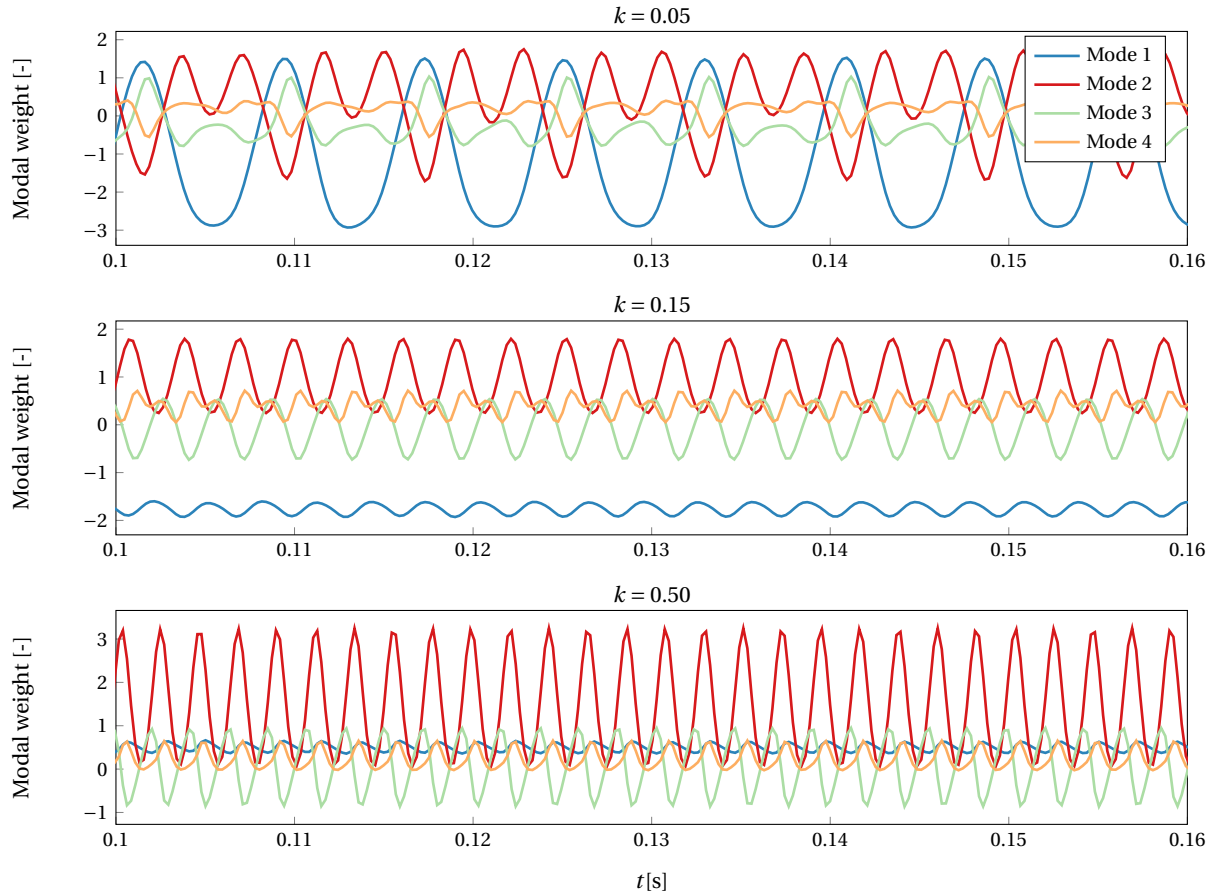


Figure 6.7: Modal decomposition of the panel response for three different shock impingement points.

impingement point, the effect of which was already estimated to be non-negligible based on analytical results in Section 4.2.4. It must be noted that unsteadiness of the impinging shock due to interaction with the shock formed at the panel leading edge is marginal, leading to motion of the shock foot which is only noticeable in the  $k = 0.50$  case. This implies that this interaction does not lie at the source of the panel flutter. Thirdly, the panel trailing edge can be identified as another major source of pressure fluctuations. This can be attributed to most of the unsteady panel motion taking place near the end of the panel, as well as the unsteadiness of the trailing edge expansion fan. This can be clearly seen in Fig. 6.4 as well. Looking at Figs. 6.8(b), 6.8(d) and 6.8(f), it can be observed that for all shock impingement locations, an alternation of compression and expansion waves can be found to originate at the panel leading edge. These seem to propagate downstream at more or less constant speed due to coupling with the panel motion, where they travel through the shock foot and are amplified accordingly. These strong waves continue moving towards the panel trailing edge, after which they are convected downstream. This travelling wave phenomenon is strongly coupled to panel motion, as a distinct difference can be observed between the  $k = 0.05$  case and the two other shock impingement locations. The strongest discrepancy can be observed near the trailing edge, where in the  $k = 0.15$  and  $k = 0.50$  case a constant alternation from recompression to expansion occurs. Due to the mean panel motion being significantly downward, the pressure field near the panel trailing edge is dominated by strong expansion of the flow, especially for  $k = 0.15$ . For the most upstream shock impingement location, much stronger pressure fluctuations occur, on the order of three times the freestream static pressure  $p_1$ . The flowfield downstream of the shockfoot is now dominated by a very strong recompression at the trailing edge, which alternates with weaker compression and expansion. It can be stated that the wall pressure temporal evolution in general looks more complex than other two cases, which can most likely be attributed to the increased modal activity, as shown by Fig. 6.7. It can be argued that the strong first mode activity is made possible by the upstream shock position, yielding a mean deflection which resembles the first structural modeshape.

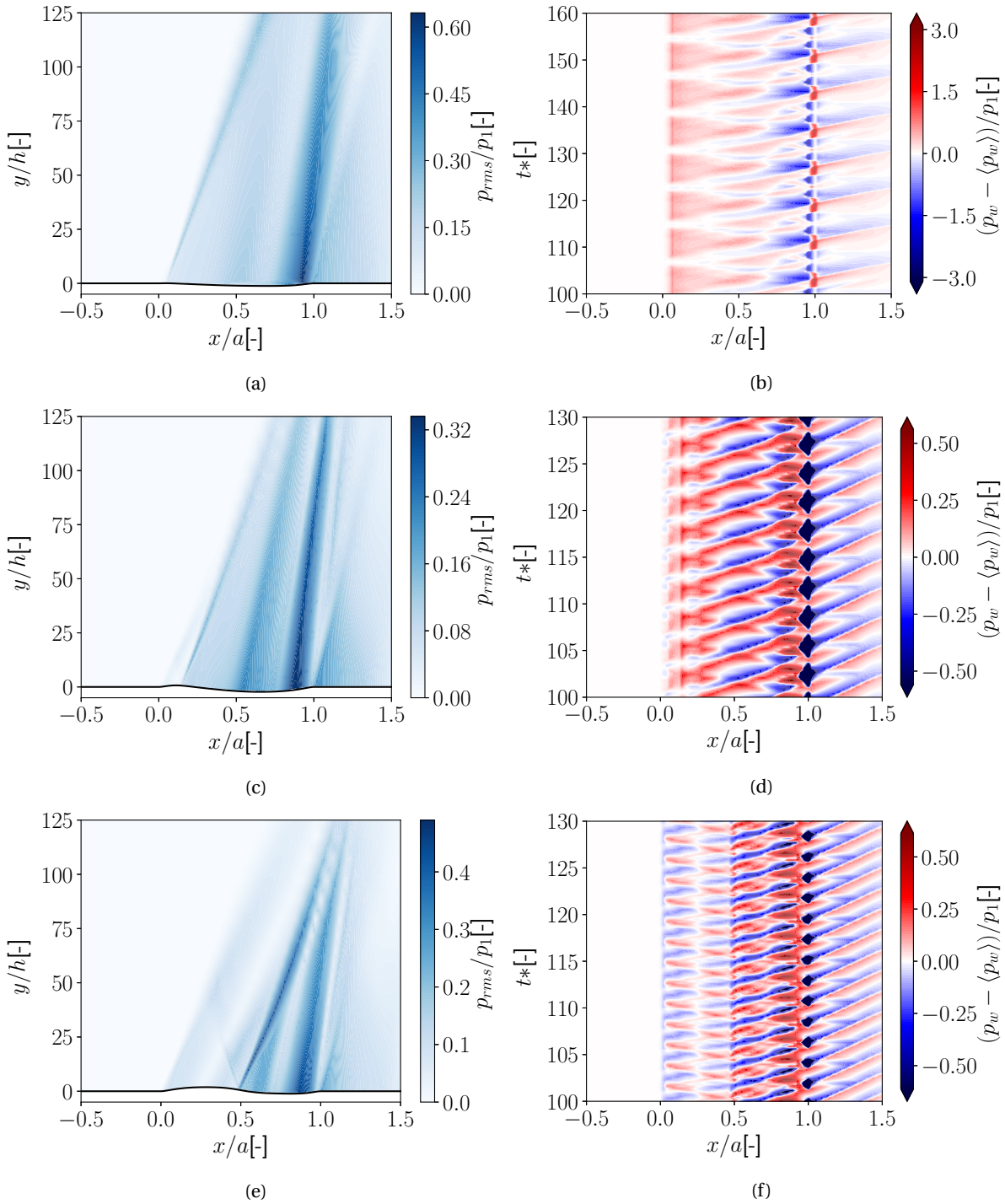


Figure 6.8: RMS-pressure contours and wall-pressure fluctuations in the  $x$ - $t$  plane for  $k = 0.05$  (top),  $k = 0.15$  (mid) and  $k = 0.50$  (bottom).

### 6.3.2. Parametric Effects

In this section the effect of changing the panel thickness and settling chamber total pressure is investigated for two shock positions:  $k = 0.15$  and  $k = 0.50$ . Looking at Eq. (3.4) it becomes clear that increasing  $h/a$ , i.e. increasing the panel thickness, will reduce the nondimensional dynamic pressure, most likely reducing panel unsteadiness. On the other hand, increasing  $p_{t,0}$  and thus the test section dynamic pressure  $q_1$  will increase  $\lambda$  and is therefore expected to increase panel motion. In the following results,  $h/a = 0.002$  and  $p_{t,0} = 3.5$  bar unless mentioned otherwise.

Looking at Fig. 6.9, it can be seen that increasing the total pressure indeed slightly increases panel amplitude and flutter frequency for  $k = 0.15$ , but for  $k = 0.5$  the effect is not so straightforward. For total pressures exceeding 4 bars, all panel motion is damped. The author argues this can be attributed to the steady panel deformation becoming too large due to the increased dynamic pressure in the tunnel, inducing a large amount of stiffness. This can be observed in Fig. 6.10, where it becomes clear that midpoint shock impingement yields a significantly increased mean panel deflection compared to the  $k = 0.15$  case. It can thus be postulated that a flexible thin panel could be employed to induce large deflections at certain dynamic pressures, and consequently damp panel unsteadiness.

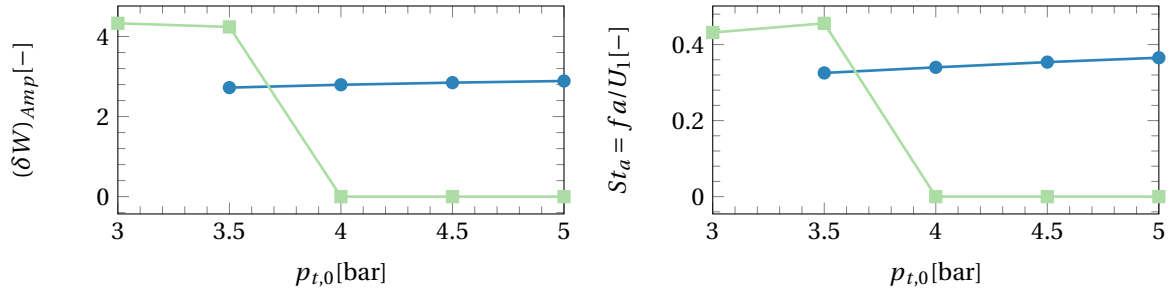


Figure 6.9: Flutter amplitude (left) and frequency (right) versus settling chamber total pressure. ( $\bullet$ )  $k = 0.15$ , ( $\blacksquare$ )  $k = 0.50$

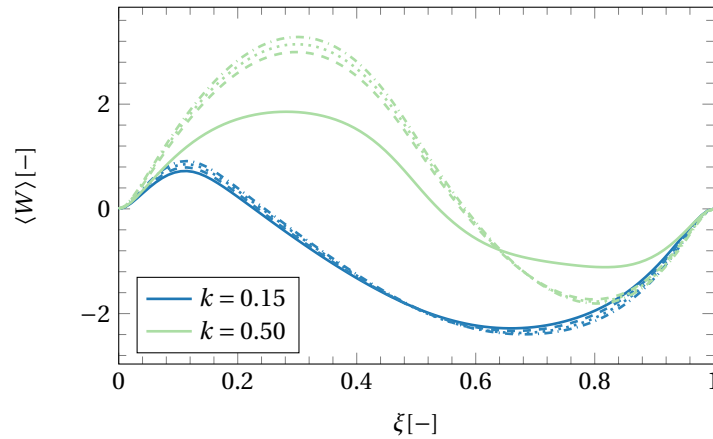


Figure 6.10: Mean panel deflection for different shock locations and settling chamber total pressures  $p_{t,0}$ .  $p_{t,0} = 3.5$  bar (—), 4.0 bar (---), 4.5 bar (.....), 5.0 bar (-.-.-)

The effect of panel thickness is shown in Fig. 6.11. As expected, increasing  $h/a$  significantly reduces the amplitude of the LCO, while also slightly reducing its frequency. The rate of decrease seems to be nearly identical for both shock impingement points, absolute value-wise. For thickness-to-length ratio's exceeding  $3.0 \cdot 10^{-3}$ , all panel motion is damped out.

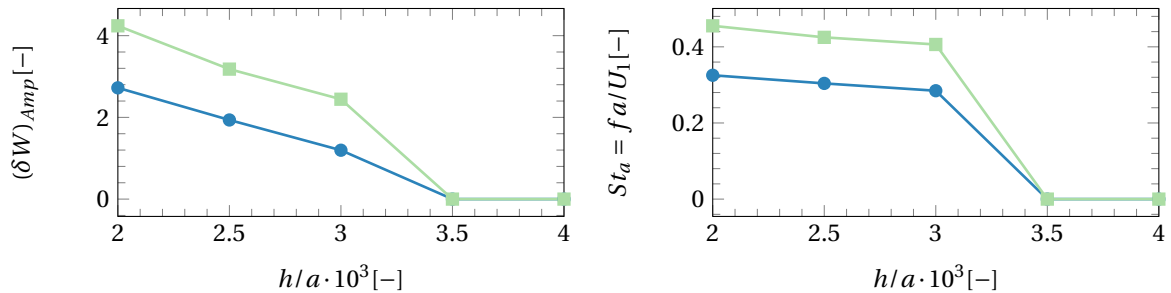


Figure 6.11: Flutter amplitude (left) and frequency (right) versus panel thickness-to-length ratio. ( $\bullet$ )  $k = 0.15$ , ( $\blacksquare$ )  $k = 0.50$

### 6.3.3. Effect of Initial Condition

In order to rule out any dependency of the statistically converged panel response on the initial conditions of the simulation, two different initial conditions are investigated here. As a first option, the panel is released immediately, i.e. simultaneously with the start of the impinging shock development. Due to the distance between the upper boundary of the domain and the panel, it takes some time for the shock to actually impinge on the panel. As a result, the panel first experiences the freestream static pressure on the upper surface, while the theoretical, significantly higher, cavity pressure is already imposed. This yields strong initial panel deflections, as indicated by the 'undeveloped IC' case in Fig. 6.12. Note that this initial condition is always employed for the 2D simulations presented in this chapter.

The second initial condition entails freezing all structural nodes until the inviscid shock system has completely developed. The result, labelled 'developed IC', clearly yields a reduction in transient deflections and converges to the exact same LCO, naturally showing a phase-shift compared to the first IC. It must be noted though that no significant computational benefit was obtained, as both initial conditions converged to the LCO after more or less equal integration times.

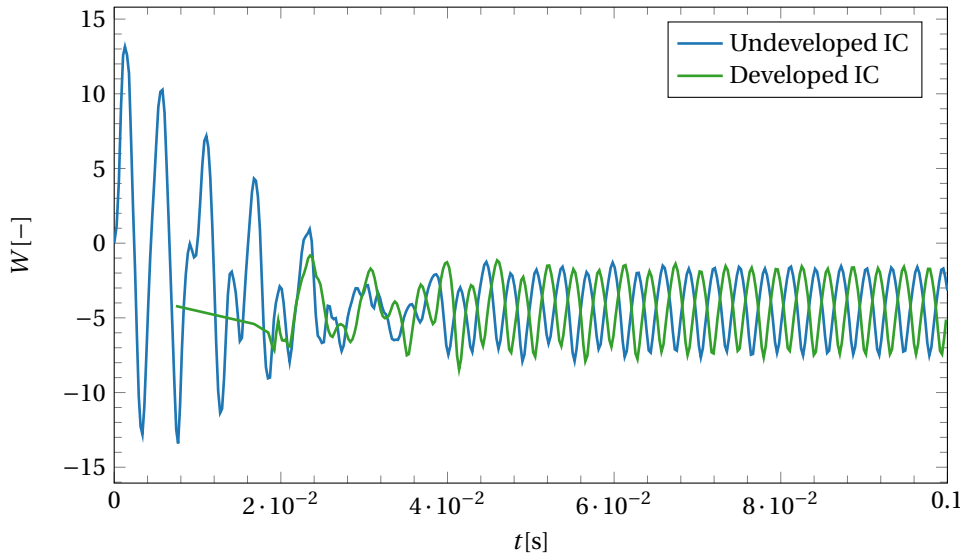


Figure 6.12: Panel response for different initial conditions.

In short, it can be concluded that the initial condition has no lasting effect on the obtained flutter motion. It can thus be argued that other transient effects, such as the normal shock occurring during tunnel start-up, will not affect the statistically converged panel response.

### 6.3.4. Adaptive Reduced Order Model

As discussed in Section 5.2, the Adaptive Reduced Order Model by Thari et al. [2017] is employed to reduce the computational overhead introduced by solving the governing structural equations. The effect of increasing the FEM update threshold on flutter amplitude and frequency can be seen in Fig. 6.13. It becomes clear that for  $\epsilon$  values up to 0.125 panel thicknesses, the error with the FEM solution ( $\epsilon = 0$ ) remains negligible. Looking at the computational cost presented in Fig. 6.14 though, more than double the amount of iterations can be performed per second walltime for such a small threshold value.

### 6.3.5. Validity of $\lambda$ as a Parameter to Characterise Flutter

As proven in the previous sections, the response of the panel to a change in panel thickness and tunnel total pressure is far from linear. Since both these parameters affect the nondimensional dynamic pressure  $\lambda^*$ , it can be questioned whether  $\lambda^*$  as given by Eq. (3.4) is still a valid parameter to characterise the flutter response, as is the case for classic panel flutter. To investigate this, the results from the parametric thickness and total pressure study are plotted versus their corresponding nondimensional dynamic pressures and compared with the analytical flutter boundaries. This is shown in Fig. 6.15. It can be seen that in general, based on the visible trends, the analytical model seems to provide a reasonable "worst-case" flutter boundary, i.e. flutter never occurs beneath the critical  $\lambda^*$  value computed with the analytical model. On the other hand, the

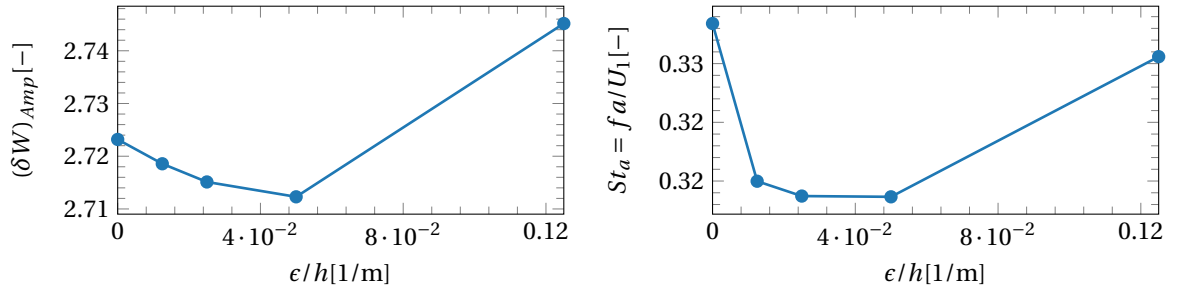


Figure 6.13: Flutter amplitude (left) and frequency (right) versus AROM update threshold in terms of panel thicknesses.

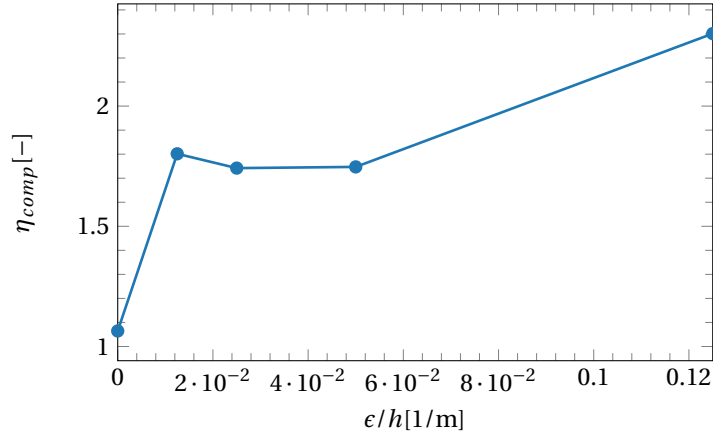


Figure 6.14: Computational efficiency  $\eta_{comp}$  versus AROM update threshold in terms of panel thicknesses. Computational efficiency is defined as iterations per second walltime.

opposite is not true: when  $p_{t,0}$  is increased for  $k = 0.50$ , a sudden damping of the panel motion is observed, as already discussed in Section 6.3.2. Flutter is thus not guaranteed to occur when  $\lambda^*$  exceeds the critical value predicted by the analytical model. Furthermore, reducing the total pressure yields two different flutter amplitudes for an identical nondimensional dynamic pressure!

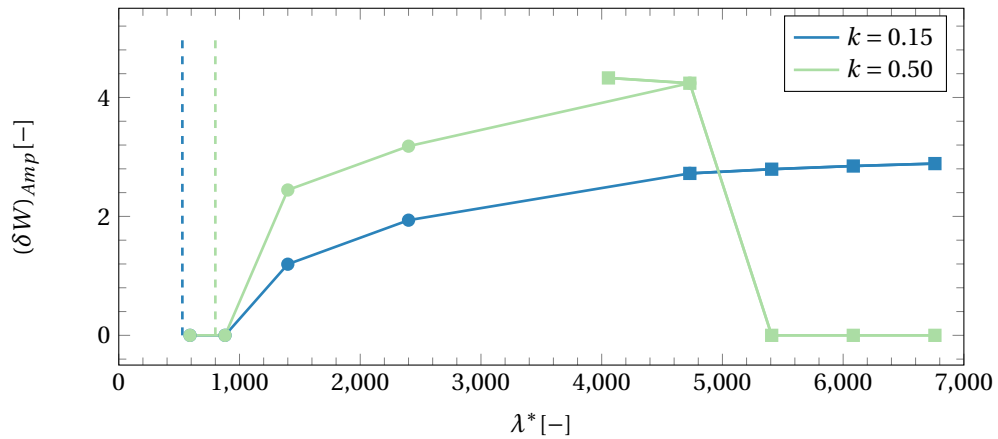


Figure 6.15: Response amplitudes versus nondimensional dynamic pressure for  $k = 0.15$  and  $k = 0.50$ . Analytical flutter boundaries are indicated by (---).  $h/a$  is decreased from  $4.0 \cdot 10^{-3}$  to  $2.0 \cdot 10^{-3}$  (—●—) and  $p_t$  is increased as indicated in Fig. 6.9 (—■—).

To further delve into this peculiar result, two different cases with identical nondimensional dynamic pressures but different panel Young's moduli and different total pressures are simulated. Case one features a total pressure of 3.5 bar and an E-modulus of 62.7 GPa, while for the second case  $p_{t,0}$  and  $E$  are set to 4.0 bars and 71.7 GPa respectively. Note that the Young's modulus of 62.7 GPa is not related to an actual material, but is rather a theoretical value chosen to achieve  $\lambda^* = 5,408$ , identical to case two.

Looking at Fig. 6.16, it becomes clear that indeed the nondimensional dynamic pressure cannot be used to characterise the response of the panel. Case one yields a rapid dampening of the flutter motion, while case two results in a clear LCO. Thus, care must be taken when reporting results in terms of  $\lambda^*$ , since these will not be reproducible if different combinations of the dimensional parameters are taken. This confirms the doubts about  $\lambda$  being an accurate flutter parameter stated in Section 3.3.1.

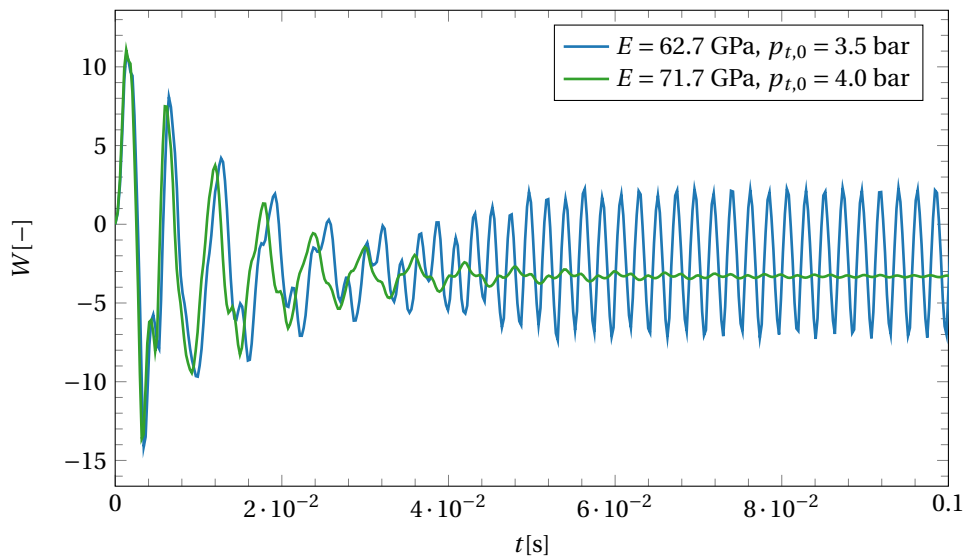


Figure 6.16: Panel responses for identical nondimensional dynamic pressures  $\lambda^*$  of 5,408 obtained at different Young's moduli and total pressures



# 7

## Selection of a Set-Up for Future Analysis by LES and Experiment

Based on the inviscid results and literature on shock-wave/boundary-layer interactions, the most promising case can now be selected for future high fidelity analysis by LES and experiment. First, values for the aerodynamic and structural governing parameters and suitable initial conditions and boundary conditions are selected in Section 7.1. Next, a feasible numerical set-up is identified in Section 7.2, after which the numerical boundary conditions and a possible grid distribution are elaborated on in Section 7.3. Lastly, preliminary experimental results are shown in Section 7.4.

### 7.1. Selection of Values for the Governing Parameters

In this section, based on the governing parameters identified in Section 3.3, values for the aerodynamic parameters are first chosen in Section 7.1.1, after which the structural parameters are selected in Section 7.1.2.

#### 7.1.1. Aerodynamic Parameters

- **Mach number  $M_1$ :** A Mach number of 2.0 is selected, which is in line with the inviscid and analytical results. This allows first of all to operate the tunnel at a total pressure which allows later PIV measurements, as discussed in Section 1.3. At higher Mach numbers, higher total pressures are required to start the windtunnel and the amplitudes of the panel motion will reduce, decreasing the interaction between fluid and structure. Secondly, selecting a Mach number lower than 2, thus 1.5 in the ST-15, could significantly increase the complexity of the flutter behaviour and the interaction with the boundary layer, as elaborated on in Section 3.3.
- **Shock strength  $p_3/p_1$ :** As discussed in Section 6.1, a shock pressure ratio of 3.0 is selected to avoid transition to an ISWBLI, while still maximising the pressure jump and thus the unsteadiness of the panel. This requires a flow deflection angle over the incident shock of  $\vartheta_1 \approx 10.66^\circ$  and a corresponding shock angle  $\sigma_1$  of  $40.04^\circ$ .
- **Boundary layer thickness  $\delta_{ref}/a$ :** Based on the results from different  $M = 2.0$  windtunnel tests performed in the ST-15 [Giepmans et al., 2014; Kallarabail, 2016; Nayak et al., 2017], as summarised in Table 1.2, the boundary layer thickness at the test section inlet can be assumed to equal  $5.2 \times 10^{-3}$  m. This yields a boundary layer thickness to plate length ratio of 19.2.
- **Cavity pressure  $p_c$ :** As mentioned in Section 3.3, setting the cavity pressure such that the steady pressure difference over the panel is minimised will yield the most unsteady behaviour. Neglecting the change in the mean pressure field due to the mean curvature of the panel, this boiled down to setting  $p_c$  equal to the theoretical pressure over the upper surface of the rigid flat plate for the inviscid computations. In the viscous case a spreading and reduction of the shock static pressure jump will occur though, due to the SWBLI and the interaction with the wedge expansion fan respectively (see Section 3.2). This will significantly affect the mean average pressure acting on the upper side of the panel. Assuming the spanwise edges of the panel are free, pressure equalisation between the test section and the cavity will

occur during the actual wind tunnel experiment, which means this significantly altered pressure distribution will affect the cavity pressure. To estimate if an LES of the interaction over a rigid flat plate is required to obtain a close approximation of the cavity pressure, the interaction obtained by Matheis and Hickel [2015] is scaled to the expected boundary layer thickness of 5.2mm and positioned over the panel, assuming the shock theoretically impinges at the panel midpoint. This is illustrated in Fig. 7.1. Integrating the wall-pressure over the panel and averaging yields an approximate cavity pressure of  $2.08 p_1$ , differing only 4.3% from the theoretical inviscid cavity pressure ( $p_c = 2.0 p_1$ ). Thus, with a similar interaction length and expansion fan impingement location,  $p_c = 0.5(p_1 + p_3)$  should yield a reasonably accurate estimate of the cavity pressure. The choice of the interaction by Matheis and Hickel [2015] as a reference SWTBLI will be elaborated on further in this section.

- **Settling chamber conditions**  $p_{t,0}, T_{t,0}$ : Since the total pressure and total temperature in the settling chamber determine the static conditions obtained in the test section, they are included in this list of governing parameters. The total temperature is assumed to equal the ambient static pressure of 288.15K. Looking at Fig. 6.9, 3.5 bars total pressure seems to be the maximum value where inviscid flutter with shock impingement at the panel midpoint still occurs. To maximise the oscillation amplitude and ensure unsteady panel movement, a total pressure of 3.5 bar is thus selected. For Mach 2.0 this yields the following static conditions in the test section:  $p_1 = 45.324 \text{ Pa}$  and  $\rho_1 = 0.986 \text{ kgm}^{-3}$ .
- **Reynolds number**  $Re$ : Given the total temperature of 288.15K and the test section Mach number of 2.0, a test section "freestream" velocity of  $507.3 \text{ ms}^{-1}$  will be obtained. Assuming the temperature dependence of the dynamic viscosity  $\mu_f$  is given by Eq. (2.8), this yields a unit Reynolds number  $Re$  of  $45.8 \times 10^6 \text{ m}^{-1}$  and a boundary layer thickness Reynolds number  $Re_{\delta,ref}$  of  $238 \times 10^3$ . The former is close to what is usually obtained in the ST-15, while the latter is nearly identical to the Reynolds number investigated by Pasquariello et al. [2015, 2017]. In the remainder of this chapter, the interaction obtained by Matheis and Hickel [2015] for a Mach 2 SWTBLI over a rigid flat surface ( $p_3/p_1 \approx 3.0$  at  $\theta = 11^\circ$ ) is taken as a baseline case to predict the viscous interaction extent. It must be noted though, that the Reynolds number considered by Matheis and Hickel [2015] is about a factor of five lower ( $Re_{\delta,imp} = 48.3 \times 10^3$ ) than the  $Re_{\delta,ref}$  considered here. As elaborated on in Section 3.2.2, a growth in the interaction length will occur up to  $Re_{\delta} = 1 \times 10^5$ , while a contraction will take place for Reynolds numbers exceeding that value. It is thus hard to predict what the actual position of the separation and reattachment shocks will be, but since the Mach number and impinging shock angle match (almost) perfectly, the interaction length of  $9.7\delta_{ref}$  is accepted as a first estimate. Note that the effect of panel unsteadiness on the separation extent is also ignored for now, since making an accurate prediction is hard, if not impossible. The selection of this baseline case will be elaborated on in the next section.

### 7.1.2. Structural Parameters

- **Plate thickness**  $h/a$ : As shown by Fig. 6.11, the maximum thickness-to-length ratio at which flutter can still be expected is  $3.0 \cdot 10^{-3}$ . For a panel length of  $10 \times 10^{-2} \text{ m}$ , this yields a maximum panel thickness of 0.3 mm. For that thickness, flutter amplitudes are strongly reduced though, which is undesirable. At the time of writing of this thesis, a fellow thesis student conducted experiments of classic panel flutter in the ST-15 at similar flow conditions as described in Section 7.1.1. For a panel thickness of 0.2 mm, the panel failed structurally during windtunnel shut-down after several runs. Thus, to keep oscillation amplitudes as large as possible and to avoid breaking the panel, a plate thickness of 0.25 mm is selected ( $h/a = 2.5 \cdot 10^{-3}$ ).
- **Length-to-width ratio**  $a/b$ : Since a quasi-2D interaction is desired at the spanwise midplane, the panel length-to-width ratio should be made as small as possible. Since the panel thickness-to-length ratio cannot exceed  $2.5 \cdot 10^{-3}$ , the panel cannot be made shorter than 10 cm, as this would lead to an unacceptably thin panel. Therefore,  $a/b$  can only be reduced by increasing the panel width  $b$ . The latter is limited by the test section width, and a certain spacing should be kept between the tunnel sidewalls and the flexible panel to avoid interaction with the sidewall boundary layer. Thus, a maximum width of 10 cm is selected, yielding a square panel ( $a/b = 1.0$ ).
- **Dynamic pressure**  $\lambda$ : As stated earlier, Eq. (3.4) yields a nondimensionalisation of the dynamic pressure  $q$  with respect to the material properties and the plate thickness-to-length ratio. Even though it was shown in Section 6.3.5 that  $\lambda$  is not a valid parameter to predict the flutter behaviour, it was selected in Section 3.3.1 as a governing structural parameter and is therefore also considered here. Since

it was decided earlier on to manufacture the flexible plate out of aerospace grade aluminium Al7075-T6 (see Section 6.1 for the material properties), the nondimensional dynamic pressure can be computed. Taking the freestream velocity and density as stated in Section 7.1.1, and the selected  $h/a$  of  $2.5 \cdot 10^{-3}$ , a dynamic pressure  $q_1$  of 127 kPa and a nondimensional variant  $\lambda^*$  of 2,423 are obtained.

- **Air/plate mass ratio  $\mathcal{M}$ :** Given the static test section conditions obtained at  $M = 2.0$  and the selected total conditions, and the structural and material properties of the plate,  $\mu_s$  equals 0.141. This is close to the value usually employed for panel flutter calculations, as stated in Section 7.1.2. Anyhow, changes in  $\mathcal{M}$  on the order of magnitude considered here are bound to only marginally affect the flutter response [Dowell, 1967].
- **Shock impingement location  $k$ :** Considering the shock impingement point, choosing a value for the governing parameter is not so straightforward. Examining Fig. 6.3, it is clear that in the inviscid case two options ensure significant unsteady motion of the panel: placing the shockfoot within 0.2 panel lengths away from the leading edge, or moving the shock impingement point into the region spanned by  $0.45 \leq x/a \leq 0.50$ . In the viscous case, this cannot simply be replicated, since a spreading of the shock pressure jump will occur as discussed in Section 3.2. Indeed, looking at the LES results obtained by Matheis and Hickel [2015], the chosen impinging shock strength will lead to a strong interaction and consequently a mean separation bubble. As a result, two wall pressure jumps will occur instead of one, more specifically one centred around the separation point and one located around the point where the shear layer reattaches to the plate, with a more or less constant pressure plateau underneath the separation bubble. The author argues that these pressure jumps should be located in the unsteady regions identified by the inviscid computations in order to maximise the odds of unsteadiness in the viscous case. To examine whether or not the pressure jumps correspond to these regions, an illustration of the interaction observed by Matheis and Hickel [2015] is aligned with the corresponding wall pressure distribution and the inviscid regions of unsteadiness indicated by their respective flutter amplitudes. This is possible by converting the interaction length in terms of  $\delta_{ref}$  to  $x/a$  by assuming the boundary layer thickness will equal 5.2mm, as discussed in Section 7.1.1. A clear pressure rise up to the separation plateau can be observed, while the second pressure rise at reattachment is reduced due to the wedge trailing edge PME fan interacting with the reflected shock system. Looking at Fig. 7.1, it becomes clear that an inviscid shock impingement location at the panel midpoint ( $k = 0.5$ ) will ensure the separation pressure jump falls completely within the unsteady region at the leading edge ( $x_s \approx k = 0.08$ ). The second jump at the reattachment point is located aft of the midplane unsteady region though ( $x_r \approx k = 0.56$ ). This is slightly undesirable, but it is clear that the wedge PME fan strongly limits the second pressure jump. Thus, positioning the separation shock foot in the leading edge unsteady region is the main goal, which is achieved for  $k = 0.5$ .
- **Distance between shock and expansion fan impingement  $L$ :** In order to get a similar cavity pressure and interaction length as Matheis and Hickel [2015], it is crucial that the first expansion wave of the PME fan is located at a similar distance  $L$  away from the inviscid shock impingement point. The strong sensitivity of the extent of the separated region on this parameter was already elaborated on in Section 3.2.2. According to inviscid computations,  $L$  should therefore equal  $6.4\delta_{ref}$ .

In the selection of the aerodynamic and structural parameters, the Mach 2.0 interaction by Matheis and Hickel [2015] was selected as a reference SWTBLI to qualitatively estimate the effect of the turbulent boundary layer on the interaction extent. At the time of writing, another high fidelity LES result was available: the Mach 3.0 interaction by Pasquariello et al. [2017]. The key parameters are listed in Table 7.1, and the interaction extents are illustrated in Fig. 7.1. It becomes clear that the chosen experimental set-up matches the Mach number  $M_1$ , shock strength  $p_3/p_1$  and expansion fan distance  $L$  of Matheis and Hickel [2015], but a strong difference in Reynolds number  $Re_\delta$  is obtained. The opposite is true for the interaction by Pasquariello et al. [2017], which features a nearly matching Reynolds number of  $203 \times 10^3$ , but a higher Mach number, a much stronger shock pressure jump and a strongly reduced distance between the shock impingement point and expansion fan. The latter is even negative, which indicates the PME fan directly affects the impinging shock. All this results in a longer interaction length compared to the one obtained by Matheis and Hickel [2015], as can be seen in Fig. 7.1. This can most likely be attributed to the stronger shock. Next to that, shock angles are significantly reduced due to the higher Mach number. The author argues the combined effect of a much higher shock strength (increased interaction length) and a reduced  $L$  will yield more uncertainty regarding

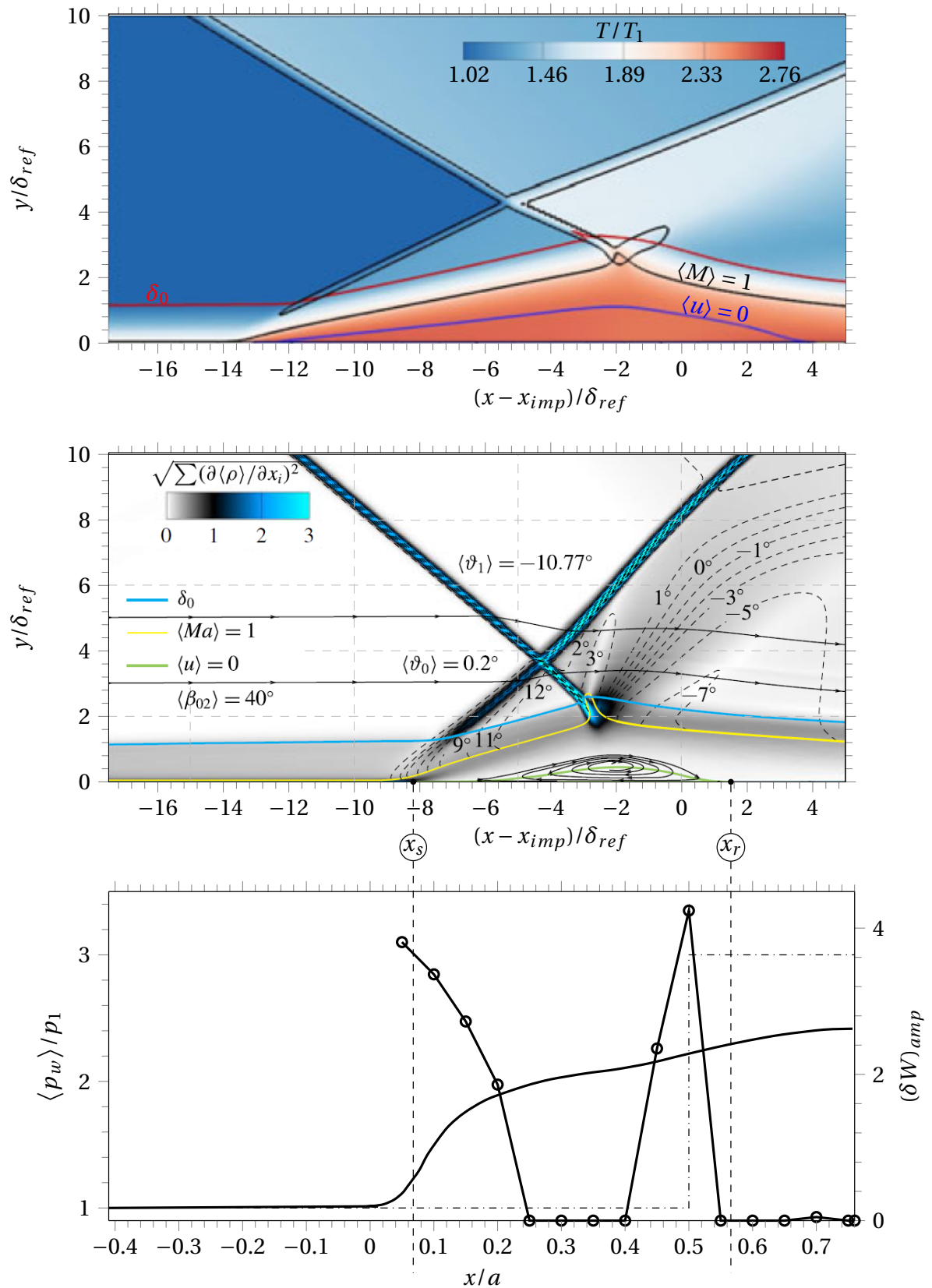


Figure 7.1: Strong SWTBLI by Pasquariello et al. [2017] (top) and Matheis and Hickel [2015] (mid) and the corresponding wall pressure distribution for the SWTBLI [Matheis and Hickel, 2015]; —, and the inviscid reflection; --- (bottom). The stability of the plate at  $x/a$  is indicated by the flutter amplitude corresponding to shock impingement at that location; ●—.

the interaction length at the chosen experimental conditions compared to only a different Reynolds number. Therefore, the interaction by Matheis and Hickel [2015] is selected as a qualitative baseline.

	$M_1[-]$	$p_3/p_1[-]$	$\vartheta_1[^\circ]$	$Re_{\delta,ref}[-]$	$L[\delta_{ref}]$
Thesis	2.0	3.0	10.66	$238 \times 10^3$	6.43
Matheis and Hickel [2015]	2.0	3.0	10.77	$48.3 \times 10^3$	6.43
Pasquariello et al. [2017]	3.0	10.3	19.60	$203 \times 10^3$	-3.64

Table 7.1: Parameters used to select a reference SWTBLI

### 7.1.3. Initial Conditions and Boundary Conditions

- **Initial condition:** The most straightforward initial condition to implement entails immediately applying the theoretical cavity pressure to the bottom of the flexible plate, while the impinging shock is still developing. As discussed in Section 6.3.3, this leads to a transient with large (non-physical) deflections. It was proven that no significant computational benefit could be obtained by first letting the shock system develop, but it does reduce the magnitude of the initial panel deformations. It must be noted that a major portion of the computational overhead can be attributed to the the mesh located in the cavity to account for panel motion. Thus, it is desirable to keep the number of cells in the cavity as low as possible, and therefore the second initial condition is selected.
- **Plate boundary condition:** Clamped leading and trailing edge boundary conditions were prescribed for the inviscid computations. Therefore, keeping also the reproducibility of the experiment in the ST-15 in mind, clamped boundary conditions are the obvious choice for the LES. To promote 2D behaviour at the spanwise midplane and pressure equalisation with the cavity, the spanwise edges are left free.

## 7.2. Numerical Set-Up

The key aerodynamic and structural parameters were selected based on 2D inviscid results and literature in Section 7.1. The resulting numerical set-up is described here. A Mach 2.0 spatially developing turbulent boundary layer enters the computational domain with a local boundary layer thickness  $\delta_{ref}$  of 5.2 mm. The total pressure and total temperature are defined in the settling chamber and equal 3.5 bar and 288.15 K respectively. The unit Reynolds number  $Re = U_1/\nu_1$  based on the static test section conditions presented in Table 7.3 equals  $45.8 \times 10^5$ , while the Reynolds number based on the inlet boundary layer thickness  $Re_{\delta,ref} = U_1\delta_{ref}/\nu_1$  is  $238 \times 10^3$ . These values are summarised in Table 7.2.

A wedge-shaped shock-generator with a length of 81.8 mm is positioned such that the trailing edge is located  $g = 96$  mm above the panel leading edge. This leads to the shock impinging halfway the 10 cm long flexible panel ( $k = 0.50$ ), and the first expansion wave of the PME fan impinging  $6.43 \delta_{ref}$  downstream of  $x_{imp}$ . This implies a nondimensional channel height to wedge width ratio  $g^+ = g/w$  of 1.15. The wedge geometries are illustrated in Fig. 7.2 and summarised in Table 7.4. The 0.25 mm thick compliant panel is manufactured out of a 7075-T6 aluminium alloy, which has a Young's modulus of  $E_s = 71.7 \times 10^9$  Pa, a Poisson's ratio of  $\nu_s = 0.33$  and a density of  $\rho_s = 2800 \text{ kg m}^{-3}$ . The panel is square with a side of 10 cm and is clamped at the leading and trailing edges. The spanwise edges are left free to induce two-dimensional behaviour of the panel and pressure equalisation between the test section and the cavity. This leads to a theoretical cavity pressure of  $p_c = k \cdot p_1 + (k - 1) \cdot p_3$ , or 90.7 kPa.

$M_1[-]$	$p_3/p_1[-]$	$\vartheta_1[^\circ]$	$p_c[\text{Pa}]$	$p_{t,0}[\text{bar}]$	$T_{t,0}[\text{K}]$	$\delta_{ref}[\text{mm}]$	$Re[1/\text{m}]$	$Re_{\delta,ref}[-]$
2.0	3.0	10.66	90,649	3.5	288.15	5.2	$45.8 \times 10^6$	$238 \times 10^3$

Table 7.2: Aerodynamic parameters

Apart from the relative positioning of the expansion fan with respect to the shock impingement point, two other geometric parameters are affected by the wedge placement and dimensions. These are not necessarily



$\theta_w [^\circ]$	$L_w [\text{mm} \delta_{ref}]$	$h_w [\text{mm} \delta_{ref}]$	$g [\text{mm} \delta_{ref}]$	$x_e [\text{mm}]$	$g^+ [-]$	$L [\text{mm} \delta_{ref}]$
10.66	81.8   15.73	111.5   21.53	96.0   18.6	0.0	1.149	33.43   6.43

Table 7.4: Wedge properties

outlined in Table 7.4, the ratio of channel inlet height to throat height equals 1.16, more than 5% smaller than the maximum critical value of 1.22. The ST-15 should therefore start without any foreseeable problems.

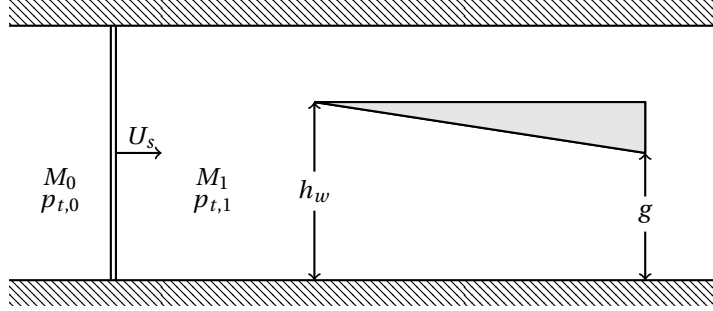


Figure 7.3: Sketch of the test section during tunnel start-up

Secondly, the ratio of channel width to throat height, i.e. the effective aspect ratio  $W/g$  of the channel formed between compliant panel and the wedge, is a good indicator of the three-dimensionality of the interaction. Wang et al. [2015] found that an aspect ratio larger than 2 should provide a two-dimensional interaction at the panel midplane. The source of this three-dimensionality is the interaction of the impinging shock with the tunnel sidewall boundary layers, which creates additional swept SWBLI's on the spanwise walls, along with corresponding separated flow regions. The latter are known to be conical in nature, appearing to originate from a virtual origin located upstream of the shock generator apex [Lu, 1993]. Due to this conical behaviour, the shock foot only penetrates the sidewall boundary layer up to a certain penetration Mach number  $M_p$ . Next to that, the sidewall shock interacts with the main impinging shock, curving it. For the case under consideration, a channel aspect ratio of 1.6 is obtained, which should be sufficiently large to yield quasi-2D behaviour at the panel midplane.

### 7.3. Boundary Conditions and Grid Distribution

The computational domain is indicated by the dashed lines in Fig. 7.2 and spans a rectangular box of dimensions  $L_x = 210$  mm,  $L_y = 96$  mm and  $L_z = 24$  mm, with the upstream boundary placed at  $x = -90$  mm. This yields an upper boundary which coincides exactly with the wedge trailing edge. In terms of boundary layer thicknesses, the domain is given by  $L_x \approx 40.4\delta_{ref}$ ,  $L_y \approx 18.5\delta_{ref}$  and  $L_z = 4.6\delta_{ref}$ . This is close to the domain size of  $L_x \times L_y \times L_z = 50\delta_{ref} \times 20\delta_{ref} \times 4.5\delta_{ref}$  determined by Pasquariello et al. [2017], which yields a sufficiently wide domain to obtain a converged separation bubble size and converged skin friction recovery downstream of the interaction. Since the IBM framework is employed to simulate motion of the flexible panel, a numerical cavity of certain depth is required to account for panel motion. Inviscid simulations at the flow conditions given in Table 7.2 and  $h/a = 2.5 \cdot 10^{-3}$  have been conducted for  $k = 0.15$  and  $k = 0.50$ . Looking at Fig. 6.6, these shock impingement points should give a good estimate of the deflection range for any shock location, also for more upstream shock impingement points ( $k = 0.05$ ). Since the separation shock-foot is expected to be located around that region, the author is confident the predicted deflection range is close to the viscous results. Looking at the maximum downward deflections during both the transient panel motion and the converged LCO shown in Fig. 7.4, it can be concluded that a cavity depth of 1 mm should be more than sufficient to account for the panel LCO, while a 2 mm cavity will be required to incorporate the transient. By first letting the shock system develop over a rigid plate, and subsequently releasing the plate, transient motion can be limited though. This was described in Section 6.3.3, and it was shown that deflections during the transient never exceeded the LCO amplitude. Using a developed flow IC will thus allow to limit the cavity depth to only 1 mm. The approach of selecting the extent of the cavity based on inviscid results has been employed successfully for SWTBLI by Pasquariello et al. [2015].

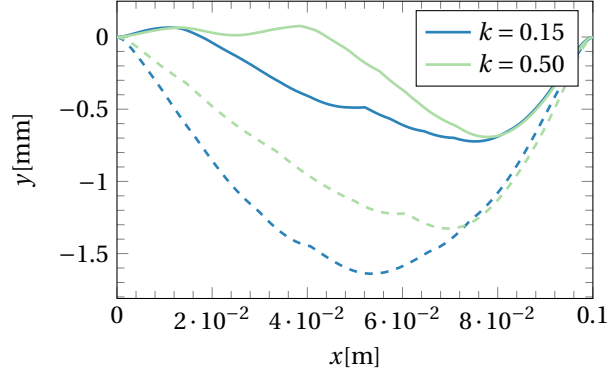


Figure 7.4: Maximum downward deflections for  $h/a = 2.5 \cdot 10^{-3}$  during transient (---) and converged oscillatory panel motion (—)

At the inflow patch, a digital filter (DF) based boundary condition is prescribed to generate turbulent inflow conditions. The method by Klein et al. [2003] is employed, which artificially reproduces the first and second order one point statistics of a precursor zero pressure gradient TBL simulation. The latter has been allowed to develop temporally until the desired boundary layer thickness of  $\delta_{ref} = 5.2\text{mm}$  was obtained. Since artificial turbulence is generated, a spatial transient downstream of the inlet is unavoidable. Pasquariello et al. [2017] determined a required transient length of  $12\delta_{ref}$  based on mean and RMS velocity profiles, while Grilli et al. [2013] obtained a transient length of  $8\delta_{ref}$ . With the inclusion of sidewall effects, Wang et al. [2015] report a transient length of  $12\delta_{ref}$ . Thus, the streamwise extent of the domain size is limited by two factors: the spatial transient introduced by the DF and the generation of the shock at the upper boundary. Based on the wedge properties, the incident shock enters the domain at  $x = -0.064$  or  $12.3$  boundary layer thickness's upstream of the panel leading edge. Thus, placing the domain inlet at  $x = -90\text{mm}$  ensures the impinging shock can be generated at the desired location while also providing a sufficient spacing of  $17.3\delta_{ref}$  between the expected start of the SWBLI and the inlet (including some spacing to mitigate Reynolds number and unsteadiness related interaction length uncertainty) to accommodate the DF transient.

Similarly to the inviscid computations, as introduced in Section 6.1, the impinging shock and expansion fan are introduced at the upper domain boundary as Riemann Invariants. The impinging shock is generated at the appropriate streamwise location by prescribing the Rankine-Hugoniot conditions corresponding to an oblique shock with angle  $\sigma_1 = 40.0^\circ$ , while the flow conditions in the wedge trailing edge expansion fan are determined by employing Prandtl-Meyer expansion theory. Note that the development of the boundary layer on the shock-generator wall is neglected. At the outflow, linear extrapolation of all flow variables is used, and symmetric boundary conditions are imposed at the spanwise domain faces. The latter implies a two-dimensional interaction, which can indeed be expected given the considered set-up [Wang et al., 2015]. Considering the fluid-structure interaction, the upper surface of the compliant panel is modelled as an adiabatic wall.

The grid is discretised based on the viscous lengthscale  $l^+$ , which can be computed as follows. Based on several boundary layer measurements conducted during experiments in the ST-15, a skin friction coefficient  $C_f$  of  $1.9 \times 10^{-3}$  can be expected at the domain inlet [Giepmans et al., 2014; Kallarbil, 2016; Nayak et al., 2017; Tambe et al., 2017]. Thus, the wall shear stress  $\tau_w = \mu_w(\partial u / \partial y)|_w$  can be computed using

$$\tau_w = \frac{1}{2} C_f \rho_1 U_1^2. \quad (7.3)$$

This yields a wall shear stress of  $241 \text{ N m}^{-2}$ . Next, the friction velocity  $u_\tau$  can be determined as follows.

$$u_\tau = \sqrt{\frac{\tau_w}{\rho_w}} \quad (7.4)$$

Thus, the density at the wall is required to obtain  $u_\tau$ . This can be computed by assuming the static temperature in the boundary layer follows the well-known Crocco-Busemann relation, which yields Eq. (7.5) for the adiabatic wall temperature.

$$T_w = T_1 \left( 1 + r \frac{\gamma - 1}{2} M_1^2 \right) \quad (7.5)$$

A recovery factor  $r$  of 0.89 is assumed, which corresponds to a Prandtl number of 0.72, a value often employed for turbulent boundary layers. Assuming the fluid behaves as an ideal gas and noting that the boundary layer static pressure is constant in  $y$ ,  $\rho_w$  can be determined. This yields a skin friction velocity of  $20.5 \text{ m s}^{-1}$ . Assuming the viscosity at the wall follows Eq. (2.8), the viscous lengthscale  $l^+ = \nu_w / u_\tau$  can be computed. For the given flow conditions, this yields  $l_w = 1.46 \mu\text{m}$  and consequently a friction Reynolds number  $Re_\tau = \delta_{ref} / l^+$  of 3,552. The main boundary layer parameters are summarised in Table 7.5.

$\rho_w [\text{kg/m}^3]$	$T_w [\text{K}]$	$\mu_w [\text{Ns/m}^2]$	$\tau_w [\text{N/m}^2]$	$u_\tau [\text{m/s}]$	$l^+ [\mu\text{m}]$	$Re_\tau [-]$
0.576	274	$1.73 \times 10^{-5}$	241	20.5	1.46	3,552

Table 7.5: Boundary layer characteristics

Based on the viscous lengthscale, an estimate of the mesh size can be made. Near the wall,  $N_x = 2,128$  and  $N_z = 608$  are taken, yielding  $\Delta x^+ = 68$  and  $\Delta z^+ = 27$ . The amount of cells in both  $x$  and  $z$  direction is systematically reduced with increasing  $y$ , as shown in Fig. 7.5.

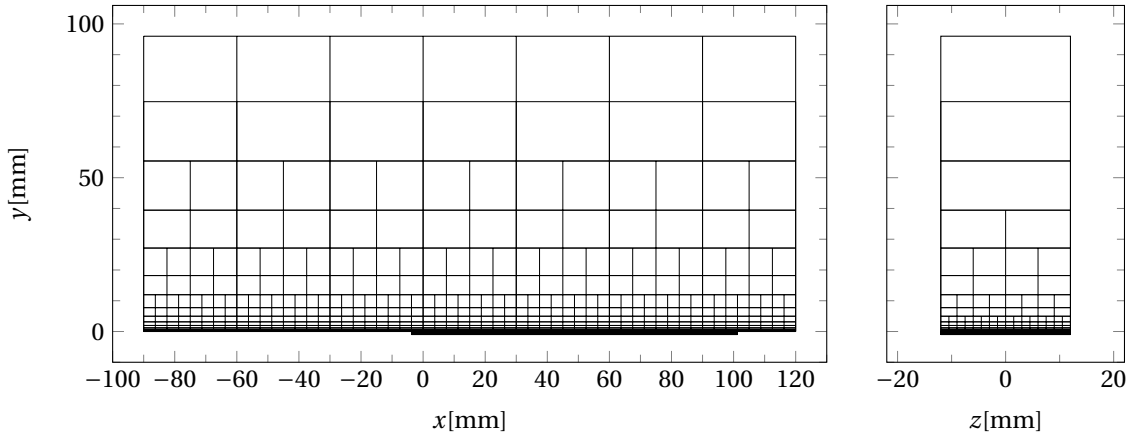


Figure 7.5: Grid distribution for the LES mesh. Only blocks are shown, with each block containing  $N_{x,b} \times N_{y,b} \times N_{z,b} = 38 \times 20 \times 36 = 27,360$  cells.

Concerning the mesh distribution in the wall-normal direction, a hyperbolic grid stretching is applied which follows

$$y_j = \frac{L_y \cdot \tanh\left(\frac{\beta_y(y-1)}{N_y-1}\right)}{\tanh(\beta_y)}, \quad (7.6)$$

where  $\beta_y$  is the stretching factor, which was set to 3.55. By discretising the  $y$ -dimension with  $N_y = 320$  cells, the first cell reaches up to  $y^+ \approx 2$ . This effectively places the first cell center at  $y_{min}^+ = 1$ , wall-resolving the boundary layer. The 1 mm deep cavity mesh is discretised by assuming the  $y^+$  value of the first cell as a constant spacing. In combination with the discretisation of the test section mesh, this yields a total amount of 438 million cells. The structural discretisation is kept the same as for the inviscid computations, featuring 196 quadratic hexahedral elements in the  $x$ -direction, two elements in the wall-normal direction and one element in the spanwise direction. The latter is justified because quasi two-dimensional flow behaviour is expected at the panel midplane.

Considering the required time integration, an initial estimate can be made as follows. Given the current streamwise domain extent, a flow-through time (FTT) of  $40.4 \delta_{ref} / U_1$  can be expected. Looking at the inviscid panel responses shown in Fig. 7.6, a transient period of about 0.06 seconds should be taken before the response starts to resemble an LCO. Note that an undeveloped IC was used for these computations, but it was proven in Section 6.3.3 that the duration of the transient is not significantly affected by the chosen initial condition. This implies a transient duration of  $5,850 \delta_{ref} / U_1 \approx 150$  FTT. Next, it would be desirable

to simulate at least 10 low frequency oscillations of the separation shock. Based on well-resolved long time-integration results by Pasquariello et al. [2017], these oscillations should occur at a separation length Strouhal number of  $St_{L,sep} = 0.04$ . Assuming a separation extent of  $9.7\delta_{ref}$  as predicted by Matheis and Hickel [2015], the timescale of the separation bubble breathing should equal  $t_{LF} = 242.5\delta_{ref}/U_1$ . Thus, to resolve 10 oscillations an extra  $2,425\delta_{ref}/U_1$  or 60 FTT should be added, yielding a total simulation time of  $8,275\delta_{ref}/U_1 \approx 205$  FTT.

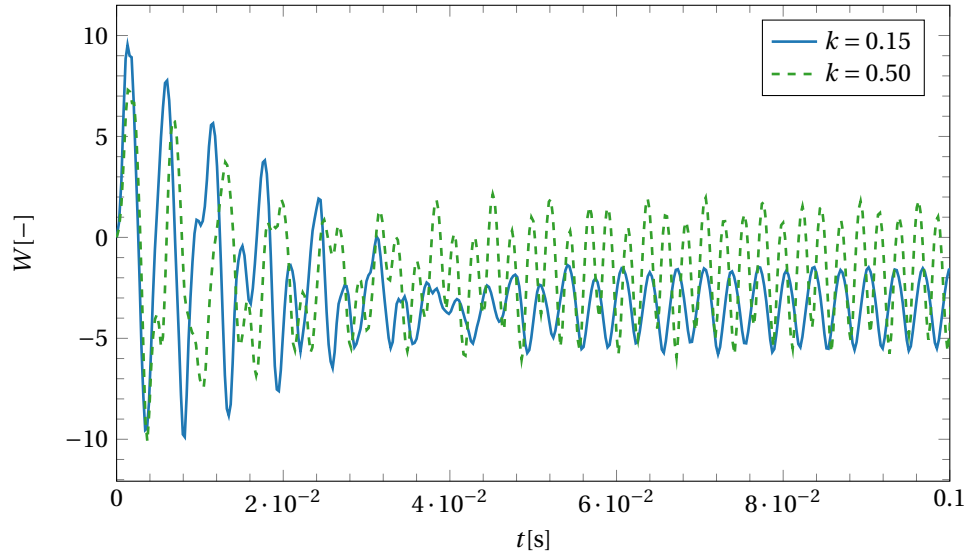


Figure 7.6: Panel responses including transient for  $k = 0.15$  and  $k = 0.50$

## 7.4. Preliminary Experimental Results

At the time of writing, a fellow thesis student <sup>†</sup> was conducting Mach 2.0 windtunnel experiments of classic panel flutter in the ST-15. He was so kind to conduct a preliminary experiment of a 0.2 mm thick Al 7075-T6 clamped panel subject to an impinging shock. The spanwise edges were left free, resulting in the same plate boundary conditions as selected for the LES and experiment. A wedge of a previously conducted experiment was used, and as a result, the generated shock was rather weak. The wedge featured a flow turning angle  $\vartheta_1$  of only 5 degrees, and had a length  $w$  of 147 mm. At the tested position, a very low channel height to wedge width ratio  $g^+$  of 0.46 was obtained. This resulted in a strongly aft position of the wedge TE PME fan, as can be clearly seen in the Schlieren image presented in Fig. 7.7. The distance between the first expansion wave and the shock impingement point at  $k = 0.37$  is estimated to have equalled  $22\delta_{ref}$ , much more than the  $6.43\delta_{ref}$  envisioned for the experiment. Given the total settling chamber pressure and temperature of 2.5 bar and 288 K respectively, a boundary layer thickness Reynolds number  $Re_{\delta,ref}$  of  $170 \times 10^3$  was obtained.

Looking at the Schlieren snapshot in Fig. 7.7, it becomes clear that a very small interaction is obtained, which seems to feature a small separation bubble. This can most likely be attributed to the very weak shock, inducing an estimated inviscid shock system pressure jump of only 1.7. Even though the shock impingement point, the shock strength and the dynamic pressure are all less favourable for flutter compared to the conditions chosen for the future experiment, the panel was found to oscillate at about 450 Hz, or  $St_a = 0.088$ , and the typical low-frequency shock motion was observed. This strongly increases the confidence in the chosen set-up, but only time will tell if it also induces flutter.

<sup>†</sup>Corresponding author: L. Mathijssen  
*E-mail:* lucas.mathijssen@gmail.com  
*Tel:*+31(0)65 357 4397

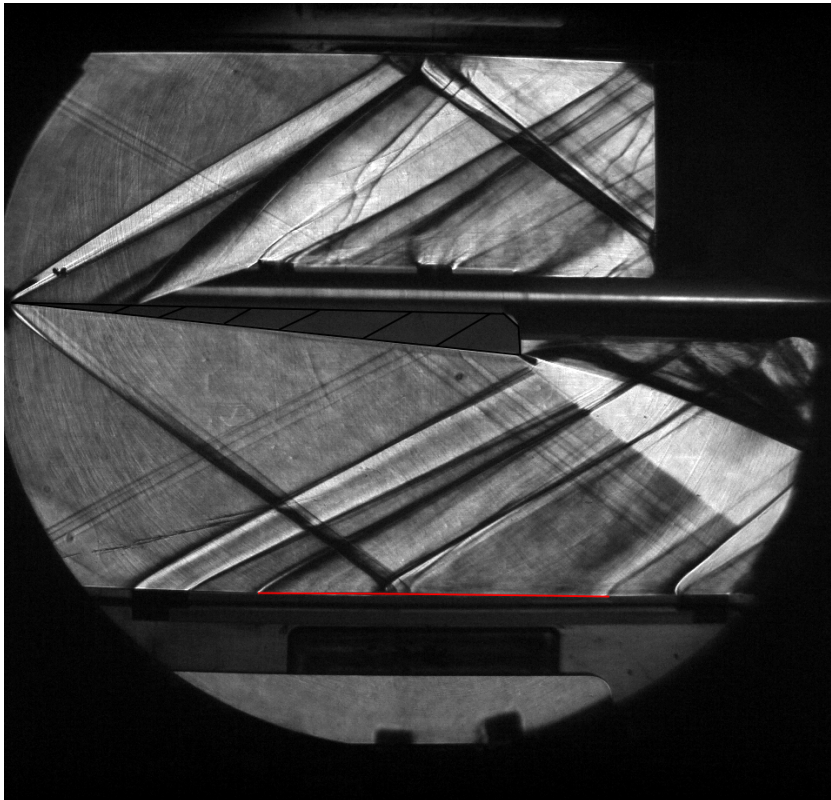
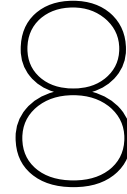


Figure 7.7: Schlieren image of the preliminary experiment. The flexible panel is indicated by the red line, while the wedge is filled with a black diagonal line pattern.





# Conclusion

In this chapter, conclusions are drawn based on the results presented in Chapter 4, Chapter 6 and Chapter 7. Next to that, recommendations for future work are given in Section 8.2.

## 8.1. Conclusions

First of all, it can be concluded that panel flutter is governed by a multitude of parameters. In the case of shock impingement, the shock strength and cavity pressure are dominant aerodynamic parameters, while from a structural point of view the plate thickness, the nondimensional dynamic pressure, the shock impingement location and the relative positioning of the shock-generator PME fan all have a significant effect on the flutter behaviour.

Considering the analytical model, it can be concluded that the state-of-the-art model by Ye and Ye [2018] lacks accuracy to correctly predict panel flutter with shock impingement. This was mainly attributed to the transverse steady pressure difference being ignored, which erroneously resulted in a flat plate reference state for the eigenvalue analysis. In an attempt to improve the model, the steady pressure difference and subsequent mean panel deformation were incorporated. This led to a successful prediction of the initial stiffening of the panel for weak shocks, as observed by Visbal [2012, 2014], but a reversal of the trend for higher shock strengths was not obtained. This proved that, due to nonlinear effects of the mean flowfield, linear stability analysis cannot be employed to predict flutter behaviour of panels subject to an impinging shock. Based on preliminary analytical calculations, it was found that the nonlinearity is mainly linked to the impinging shock passively adapting to the local change in panel slope at the shock impingement point and the significant Mach number variation along the panel. Both these effects limit the applicability of the employed linear piston theory. Looking at the obtained inviscid results, it can be stated that the analytical flutter boundaries do provide an upper bound on the flutter-free region, and can thus be used to design flutter-free structures.

Regarding the inviscid computations, the sensitivity of the flutter behaviour of clamped panels with respect to shock impingement point, panel thickness and dynamic pressure was investigated, effectively extending the research by Visbal [2012, 2014]. First of all, it can be concluded that a strong dependency on the shock impingement location exists. Two unsteady regions were identified: one close to the panel leading edge, and one around the panel midpoint. The modal content of the response was found to be more or less consistent for all shock locations, except for shock impingement close to the leading edge ( $k = 0.05$ ). For the former, mainly second and third mode content was observed, while for the latter a coupling between a low frequency first mode and higher frequency second mode oscillation was obtained.

The effect of an increased panel thickness was found to be a damping of the LCO, while a more non-homogeneous behaviour with increasing dynamic pressure was observed. The latter was found to either amplify or damp panel motion, depending on shock impingement location. This behaviour indicated that the nondimensional dynamic pressure is not a valid parameter to characterise panel flutter with shock impingement, which was confirmed by investigating two cases with identical nondimensional dynamic pressure, but different Young's moduli and total pressures. Flutter was observed in one case, while a steady solution was obtained for the other.

Next, a set-up for future analysis by LES and experiments had to be selected, a process during which it became clear that inviscid computations only provide limited insight in the viscous result. Especially the interaction length of the SWTBLI is subject to a significant amount of uncertainty, which is attributable to the Reynolds number, the shock strength, the relative positioning of the expansion fan, panel unsteadiness and low frequency motion of the separation shock. Since no results of a SWTBLI over a rigid plate at the chosen conditions is available in literature, it is hard to predict the mean location of the separated shock foot. The interaction by Matheis and Hickel [2015] was found to differ from the chosen set-up only in Reynolds number though, and was thus selected as a baseline SWTBLI case. By letting the shock impinge at the panel midpoint and overlaying the viscous interaction with the flexible panel, it was found that the expected interaction length should place the separation shock foot in the unsteady region close to the leading edge. Total pressure and panel thickness were selected based on the inviscid results, while wedge dimensions were carefully selected with the interaction length and windtunnel limitations in mind. Confidence in the set-up is increased by examining a recent ST-15 windtunnel experiment conducted by a fellow thesis student at less favourable conditions for flutter, which was found to induce an LCO.

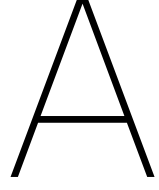
In short, it can be concluded that the chosen set-up minimises uncertainty regarding the interaction length as much as possible, and maximises the probability of an interaction with strong panel unsteadiness. The set-up avoids the problems encountered by Daub et al. [2015b] and Pasquariello et al. [2015] by 1) letting the spanwise panel edges free and not sealing them with soft foam, 2) employing a rigid non-rotating shock-generator, and 3) ensuring a deep cavity. Next to that, inviscid computations with different initial conditions were conducted and it became apparent that these do not affect the converged statistically stationary response. Lastly, an initial estimation of the LES grid distribution and required integration time have shown that the numerical experiment should be feasible from a computational point of view. It can thus be concluded that an experiment has been designed which is both achievable numerically and in the windtunnel.

## 8.2. Recommendations

Concerning the analytical model, integrating the governing equation in time instead of employing linear stability analysis might yield interesting results. Furthermore, it could be insightful to incorporate a passively adapting reflected shock strength. Secondly, since it was proven the nondimensional dynamic pressure is not a reliable parameter to characterise flutter, an empirical model could be constructed based on inviscid computations. It should include all dimensional parameters making up the classic nondimensional dynamic pressure and ideally also the shock impingement point. Concerning the latter, it is still unclear why certain shock locations induce flutter while others do not. This could be an interesting topic for future research, and perhaps a link can be found with the structural eigenfrequencies and/or their alteration due to mean panel deformation.

A logical follow-up on the thesis is actually conducting the coupled large-eddy simulation. With the numerical set-up already designed, this should be rather straightforward. As a next step, the experiment should be conducted in the ST-15, which should also be feasible. Indeed, in this thesis strong emphasis was placed on the reproducibility of the numerical experiment in actual experimental conditions attainable in the ST-15. Thus, if all goes well, validation of numerical tools for coupled SWTBLI should be possible in the near future.

Other effects which will occur in real-life applications involving SWTBLI are heat transfer to the panel and double sided flow. Therefore, it would be very interesting to use the validated numerical tools to conduct numerical simulations of shock-wave/boundary-layer interaction coupled to a non-adiabatic flexible plate and/or a flexible plate subject to a supersonic flow at both sides.



## Four Mode Jacobian Entries at the Flat Plate Equilibrium Solution

$$\begin{aligned}
a_{51} &= \left[ (n-1) \left( \frac{1}{2} - \frac{1}{2} \cos(2\pi k) \right) \right] \lambda_{u,l} - \pi^4 + R_x^T \pi^2 = a_{51}^0 \lambda_{u,l} + a_{51}^\epsilon \\
a_{52} &= \left[ \frac{4}{3} (1+n+2m) + (n-1) \left( -\frac{2}{3} \cos(3\pi k) + 2 \cos(\pi k) \right) \right] \lambda_{u,l} = a_{52}^0 \lambda_{u,l} \\
a_{53} &= \left[ (n-1) \left( -\frac{3}{4} - \frac{3}{4} \cos(4\pi k) + \frac{3}{2} \cos(2\pi k) \right) \right] \lambda_{u,l} = a_{53}^0 \lambda_{u,l} \\
a_{54} &= \left[ \frac{8}{15} (1+n+2m) + (n-1) \left( -\frac{4}{5} \cos(5\pi k) + \frac{4}{3} \cos(3\pi k) \right) \right] \lambda_{u,l} = a_{54}^0 \lambda_{u,l} \\
a_{55} &= \left[ -\left( \sqrt{R_{Mu,r}n} + \sqrt{R_{Md}m} \right) + \left( \sqrt{R_{Mu,r}n} - \sqrt{R_{Mu,l}} \right) \left( k - \frac{\sin(2\pi k)}{2\pi} \right) \right] \sqrt{\lambda_{u,l}} = a_{55}^0 \sqrt{\lambda_{u,l}} \\
a_{56} &= \left[ \left( \sqrt{R_{Mu,r}n} - \sqrt{R_{Mu,l}} \right) \left( \frac{\sin(\pi k)}{\pi} - \frac{\sin(3\pi k)}{3\pi} \right) \right] \sqrt{\lambda_{u,l}} = a_{56}^0 \sqrt{\lambda_{u,l}} \\
a_{57} &= \left[ \left( \sqrt{R_{Mu,r}n} - \sqrt{R_{Mu,l}} \right) \left( \frac{\sin(2\pi k)}{2\pi} - \frac{\sin(4\pi k)}{4\pi} \right) \right] \sqrt{\lambda_{u,l}} = a_{57}^0 \sqrt{\lambda_{u,l}} \\
a_{58} &= \left[ \left( \sqrt{R_{Mu,r}n} - \sqrt{R_{Mu,l}} \right) \left( \frac{\sin(3\pi k)}{3\pi} - \frac{\sin(5\pi k)}{5\pi} \right) \right] \sqrt{\lambda_{u,l}} = a_{58}^0 \sqrt{\lambda_{u,l}}
\end{aligned} \tag{A.1}$$

$$\begin{aligned}
a_{61} &= \left[ -\frac{4}{3} (1+n+2m) + (n-1) \left( -\frac{1}{3} \cos(3\pi k) - \cos(\pi k) \right) \right] \lambda_{u,l} = a_{61}^0 \lambda_{u,l} \\
a_{62} &= \left[ (n-1) \left( \frac{1}{2} - \frac{1}{2} \cos(4\pi k) \right) \right] \lambda_{u,l} - 16\pi^4 + R_x^T 4\pi^2 = a_{62}^0 \lambda_{u,l} + a_{62}^\epsilon \\
a_{63} &= \left[ \frac{12}{5} (1+n+2m) + (n-1) \left( -\frac{3}{5} \cos(5\pi k) + 3 \cos(\pi k) \right) \right] \lambda_{u,l} = a_{63}^0 \lambda_{u,l} \\
a_{64} &= \left[ (n-1) \left( -\frac{4}{3} - \frac{2}{3} \cos(6\pi k) + 2 \cos(2\pi k) \right) \right] \lambda_{u,l} = a_{64}^0 \lambda_{u,l} \\
a_{65} &= \left[ \left( \sqrt{R_{Mu,r}n} - \sqrt{R_{Mu,l}} \right) \left( \frac{\sin(\pi k)}{\pi} - \frac{\sin(3\pi k)}{3\pi} \right) \right] \sqrt{\lambda_{u,l}} = a_{65}^0 \sqrt{\lambda_{u,l}} \\
a_{66} &= \left[ -\left( \sqrt{R_{Mu,r}n} + \sqrt{R_{Md}m} \right) + \left( \sqrt{R_{Mu,r}n} - \sqrt{R_{Mu,l}} \right) \left( k - \frac{\sin(4\pi k)}{4\pi} \right) \right] \sqrt{\lambda_{u,l}} = a_{66}^0 \sqrt{\lambda_{u,l}} \\
a_{67} &= \left[ \left( \sqrt{R_{Mu,r}n} - \sqrt{R_{Mu,l}} \right) \left( \frac{\sin(\pi k)}{\pi} - \frac{\sin(5\pi k)}{5\pi} \right) \right] \sqrt{\lambda_{u,l}} = a_{67}^0 \sqrt{\lambda_{u,l}} \\
a_{68} &= \left[ \left( \sqrt{R_{Mu,r}n} - \sqrt{R_{Mu,l}} \right) \left( \frac{\sin(2\pi k)}{2\pi} - \frac{\sin(6\pi k)}{6\pi} \right) \right] \sqrt{\lambda_{u,l}} = a_{68}^0 \sqrt{\lambda_{u,l}}
\end{aligned} \tag{A.2}$$

$$\begin{aligned}
a_{71} &= \left[ (n-1) \left( \frac{3}{4} - \frac{1}{4} \cos(4\pi k) - \frac{1}{2} \cos(2\pi k) \right) \right] \lambda_{u,l} = a_{71}^0 \lambda_{u,l} \\
a_{72} &= \left[ -\frac{12}{5} (1+n+2m) + (n-1) \left( -\frac{2}{5} \cos(5\pi k) - 2 \cos(\pi k) \right) \right] \lambda_{u,l} = a_{72}^0 \lambda_{u,l} \\
a_{73} &= \left[ (n-1) \left( \frac{1}{2} - \frac{1}{2} \cos(6\pi k) \right) \right] \lambda_{u,l} - 81\pi^4 + R_x^T 9\pi^2 = a_{73}^0 \lambda_{u,l} + a_{73}^\epsilon \\
a_{74} &= \left[ \frac{24}{7} (1+n+2m) + (n-1) \left( -\frac{4}{7} \cos(7\pi k) + 4 \cos(\pi k) \right) \right] \lambda_{u,l} = a_{74}^0 \lambda_{u,l} \\
a_{75} &= \left[ \left( \sqrt{R_{Mu,r}n} - \sqrt{R_{Mu,l}} \right) \left( \frac{\sin(2\pi k)}{2\pi} - \frac{\sin(4\pi k)}{4\pi} \right) \right] \sqrt{\lambda_{u,l}} = a_{75}^0 \sqrt{\lambda_{u,l}} \\
a_{76} &= \left[ \left( \sqrt{R_{Mu,r}n} - \sqrt{R_{Mu,l}} \right) \left( \frac{\sin(\pi k)}{\pi} - \frac{\sin(5\pi k)}{5\pi} \right) \right] \sqrt{\lambda_{u,l}} = a_{76}^0 \sqrt{\lambda_{u,l}} \\
a_{77} &= \left[ -\left( \sqrt{R_{Mu,r}n} + \sqrt{R_{Md}m} \right) + \left( \sqrt{R_{Mu,r}n} - \sqrt{R_{Mu,l}} \right) \left( k - \frac{\sin(6\pi k)}{6\pi} \right) \right] \sqrt{\lambda_{u,l}} = a_{77}^0 \sqrt{\lambda_{u,l}} \\
a_{78} &= \left[ \left( \sqrt{R_{Mu,r}n} - \sqrt{R_{Mu,l}} \right) \left( \frac{\sin(\pi k)}{\pi} - \frac{\sin(7\pi k)}{7\pi} \right) \right] \sqrt{\lambda_{u,l}} = a_{78}^0 \sqrt{\lambda_{u,l}}
\end{aligned} \tag{A.3}$$

$$\begin{aligned}
a_{81} &= \left[ -\frac{8}{15} (1+n+2m) + (n-1) \left( -\frac{1}{5} \cos(5\pi k) - \frac{1}{3} \cos(3\pi k) \right) \right] \lambda_{u,l} = a_{81}^0 \lambda_{u,l} \\
a_{82} &= \left[ (n-1) \left( \frac{4}{3} - \frac{1}{3} \cos(6\pi k) - \cos(2\pi k) \right) \right] \lambda_{u,l} = a_{82}^0 \lambda_{u,l} \\
a_{83} &= \left[ -\frac{24}{7} (1+n+2m) + (n-1) \left( -\frac{3}{7} \cos(7\pi k) - 3 \cos(\pi k) \right) \right] \lambda_{u,l} = a_{83}^0 \lambda_{u,l} \\
a_{84} &= \left[ (n-1) \left( \frac{1}{2} - \frac{1}{2} \cos(8\pi k) \right) \right] \lambda_{u,l} - 256\pi^4 + R_x^T 16\pi^2 = a_{84}^0 \lambda_{u,l} + a_{84}^\epsilon \\
a_{85} &= \left[ \left( \sqrt{R_{Mu,r}n} - \sqrt{R_{Mu,l}} \right) \left( \frac{\sin(3\pi k)}{3\pi} - \frac{\sin(5\pi k)}{5\pi} \right) \right] \sqrt{\lambda_{u,l}} = a_{85}^0 \sqrt{\lambda_{u,l}} \\
a_{86} &= \left[ \left( \sqrt{R_{Mu,r}n} - \sqrt{R_{Mu,l}} \right) \left( \frac{\sin(2\pi k)}{2\pi} - \frac{\sin(6\pi k)}{6\pi} \right) \right] \sqrt{\lambda_{u,l}} = a_{86}^0 \sqrt{\lambda_{u,l}} \\
a_{87} &= \left[ \left( \sqrt{R_{Mu,r}n} - \sqrt{R_{Mu,l}} \right) \left( \frac{\sin(\pi k)}{\pi} - \frac{\sin(7\pi k)}{7\pi} \right) \right] \sqrt{\lambda_{u,l}} = a_{87}^0 \sqrt{\lambda_{u,l}} \\
a_{88} &= \left[ -\left( \sqrt{R_{Mu,r}n} + \sqrt{R_{Md}m} \right) + \left( \sqrt{R_{Mu,r}n} - \sqrt{R_{Mu,l}} \right) \left( k - \frac{\sin(8\pi k)}{8\pi} \right) \right] \sqrt{\lambda_{u,l}} = a_{88}^0 \sqrt{\lambda_{u,l}}
\end{aligned} \tag{A.4}$$

# B

## Entries for the Four Mode Routh-Hurwitz Criterion

$$t_1 = A_1 - \frac{A_7 A_0}{A_6 - \frac{A_5}{A_7}} - \frac{\left( A_5 - \frac{A_7(A_4 - \frac{A_3}{A_7})}{A_6 - \frac{A_5}{A_7}} \right) A_0}{\left( A_6 - \frac{A_5}{A_7} \right) \left( A_3 - \frac{A_7(A_2 - \frac{A_1}{A_7})}{A_6 - \frac{A_5}{A_7}} \right)} \quad (\text{B.1})$$

$$A_4 - \frac{A_3}{A_7} - \frac{A_7(A_4 - \frac{A_3}{A_7})}{A_5 - \frac{A_7(A_4 - \frac{A_3}{A_7})}{A_6 - \frac{A_5}{A_7}}}$$

$$t_2 = A_3 - \frac{A_7(A_2 - \frac{A_1}{A_7})}{A_6 - \frac{A_5}{A_7}} - \frac{\left( A_5 - \frac{A_7(A_4 - \frac{A_3}{A_7})}{A_6 - \frac{A_5}{A_7}} \right) \left( A_2 - \frac{A_1}{A_7} - \frac{\left( A_6 - \frac{A_5}{A_7} \right) \left( A_1 - \frac{A_7 A_0}{A_6 - \frac{A_5}{A_7}} \right)}{A_5 - \frac{A_7(A_4 - \frac{A_3}{A_7})}{A_6 - \frac{A_5}{A_7}}} \right)}{\left( A_6 - \frac{A_5}{A_7} \right) \left( A_3 - \frac{A_7(A_2 - \frac{A_1}{A_7})}{A_6 - \frac{A_5}{A_7}} \right)} \quad (\text{B.2})$$

$$A_4 - \frac{A_3}{A_7} - \frac{A_7(A_4 - \frac{A_3}{A_7})}{A_5 - \frac{A_7(A_4 - \frac{A_3}{A_7})}{A_6 - \frac{A_5}{A_7}}}$$

$$t_3 = A_2 - \frac{A_1}{A_7} - \frac{\left( A_6 - \frac{A_5}{A_7} \right) \left( A_1 - \frac{A_7 A_0}{A_6 - \frac{A_5}{A_7}} \right)}{A_5 - \frac{A_7(A_4 - \frac{A_3}{A_7})}{A_6 - \frac{A_5}{A_7}}} \quad (\text{B.3})$$

$$t_4 = \left( A_4 - \frac{A_3}{A_7} - \frac{\left( A_6 - \frac{A_5}{A_7} \right) \left( A_3 - \frac{A_7 \left( A_2 - \frac{A_1}{A_7} \right)}{A_6 - \frac{A_5}{A_7}} \right)}{A_5 - \frac{A_7 \left( A_4 - \frac{A_3}{A_7} \right)}{A_6 - \frac{A_5}{A_7}}} \right) \left( A_1 - \frac{A_7 A_0}{A_6 - \frac{A_5}{A_7}} - \frac{\left( A_5 - \frac{A_7 \left( A_4 - \frac{A_3}{A_7} \right)}{A_6 - \frac{A_5}{A_7}} \right) A_0}{A_4 - \frac{A_3}{A_7} - \frac{\left( A_6 - \frac{A_5}{A_7} \right) \left( A_3 - \frac{A_7 \left( A_2 - \frac{A_1}{A_7} \right)}{A_6 - \frac{A_5}{A_7}} \right)}{A_5 - \frac{A_7 \left( A_4 - \frac{A_3}{A_7} \right)}{A_6 - \frac{A_5}{A_7}}} \right) \right) \quad (\text{B.4})$$

$$t_5 = A_3 - \frac{A_7 \left( A_2 - \frac{A_1}{A_7} \right)}{A_6 - \frac{A_5}{A_7}} - \frac{\left( A_5 - \frac{A_7 \left( A_4 - \frac{A_3}{A_7} \right)}{A_6 - \frac{A_5}{A_7}} \right) \left( A_2 - \frac{A_1}{A_7} - \frac{\left( A_6 - \frac{A_5}{A_7} \right) \left( A_1 - \frac{A_7 A_0}{A_6 - \frac{A_5}{A_7}} \right)}{A_5 - \frac{A_7 \left( A_4 - \frac{A_3}{A_7} \right)}{A_6 - \frac{A_5}{A_7}}} \right)}{A_4 - \frac{A_3}{A_7} - \frac{\left( A_6 - \frac{A_5}{A_7} \right) \left( A_3 - \frac{A_7 \left( A_2 - \frac{A_1}{A_7} \right)}{A_6 - \frac{A_5}{A_7}} \right)}{A_5 - \frac{A_7 \left( A_4 - \frac{A_3}{A_7} \right)}{A_6 - \frac{A_5}{A_7}}} \right)} \quad (\text{B.5})$$

# Bibliography

- Adams, N.A. , Hickel, S. , and Franz, S. . Implicit Subgrid-Scale Modeling by Adaptive Deconvolution. *Journal of Computational Physics*, 200(2):412 – 431, 2004. ISSN 0021-9991. doi: [10.1016/j.jcp.2004.04.010](https://doi.org/10.1016/j.jcp.2004.04.010).
- Agostini, L. , Larchevêque, L. , Dupont, P. , Debiève, J.-F. , and J.P., Dussauge . Zones of Influence and Shock Motion in a Shock/Boundary-Layer Interaction. *AIAA Journal*, 50(6):1377–1387, 2012. doi: [10.2514/1.J051516](https://doi.org/10.2514/1.J051516).
- Alder, M. . Development and Validation of a Fluid–Structure Solver for Transonic Panel Flutter. *AIAA Journal*, 53(12):3509–3521, 2015. doi: [10.2514/1.J054013](https://doi.org/10.2514/1.J054013).
- Andreopoulos, J. and Muck, K. C. . Some New Aspects of the Shock-Wave/Boundary-Layer Interaction in Compression-Ramp Flows. *Journal of Fluid Mechanics*, 180:405–428, 1987. doi: [10.1017/S0022112087001873](https://doi.org/10.1017/S0022112087001873).
- Aubard, G. , Gloerfelt, X. , and Robinet, J.-C. . Large-Eddy Simulation of Broadband Unsteadiness in a Shock/Boundary-Layer Interaction. *AIAA Journal*, 51(10):2395–2409, 2013. doi: [10.2514/1.J052249](https://doi.org/10.2514/1.J052249).
- Baars, W.J. , Ruf, J.H. , and Tinney, C.E. . Non-Stationary Shock Motion Unsteadiness in an Axisymmetric Geometry with Pressure Gradient. *Experiments in Fluids*, 56(5):56–92, 2015. doi: [10.1007/s00348-015-1958-y](https://doi.org/10.1007/s00348-015-1958-y).
- Babinsky, H. . *Shock Wave-Boundary-Layer Interactions*. Cambridge Aerospace Series. Cambridge University Press, 2011. doi: [10.1017/CBO9780511842757](https://doi.org/10.1017/CBO9780511842757).
- Bebernis, T. , Spottswood, S.M. , and Eason, T.G. . High-Speed Digital Image Correlation Measurements of Random Nonlinear Dynamic Response. In *Experimental and Applied Mechanics, Volume 6*, pages 171–186, New York, NY, 2011. Springer New York. ISBN 978-1-4614-0222-0. doi: [10.1007/978-1-4614-0222-0\\_22](https://doi.org/10.1007/978-1-4614-0222-0_22).
- Bebernis, T. , Eason, T.G. , and Spottswood, S.M. . High-Speed 3D Digital Image Correlation Measurements of Long Duration Random Vibration; Recent Advancements and Noted Limitations. In *Proceedings of the ISMA-2012*, Leuven, Belgium, 2012.
- Ben-Dor, G. . *Shock Wave Reflection Phenomena*. Springer-Verlag Berlin Heidelberg, 2007. ISBN 978-3-642-09052-3. doi: [10.1007/978-3-540-71382-1](https://doi.org/10.1007/978-3-540-71382-1).
- Boccaletto, L. , Reijasse, P. , and Dussauge, J.P. . Dynamic Behaviour of a Separation Oblique Shock During Film Cooling Transient Injection. In *37th AIAA Fluid Dynamics Conference and Exhibit*. AIAA 2007-4003, 2007. doi: [10.2514/6.2007-4003](https://doi.org/10.2514/6.2007-4003).
- Boyer, N.R. , McNamara, J.J. , and Gaitonde, D.V. . Study on Shock-Induced Panel Flutter in 2-D Laminar Flow. In *15th Dynamics Specialists Conference*, San Diego, California, U.S.A., 2016. American Institute of Aeronautics and Astronautics. doi: [10.2514/6.2016-1091](https://doi.org/10.2514/6.2016-1091).
- Boyer, N.R. , McNamara, J.J. , Gaitonde, D.V. , Barnes, C.J. , and Visbal, R.M. . Features of Shock-Induced Panel Flutter in Three-Dimensional Inviscid Flow. *Journal of Fluids and Structures*, 83:490–506, 11 2018. doi: [10.1016/j.jfluidstructs.2018.10.001](https://doi.org/10.1016/j.jfluidstructs.2018.10.001).
- Brouwer, K. , Crowell, A.R. , and McNamara, J.J. . Rapid Prediction of Unsteady Aeroelastic Loads in Shock-Dominated Flows. In *56th AIAA/ASCE/AHS/ASC Structures, Structural Dynamics, and Materials Conference*, 2015. doi: [10.2514/6.2015-0687](https://doi.org/10.2514/6.2015-0687).
- Brouwer, K.R. , Gogulapati, A. , and McNamara, J.J. . Interplay of Surface Deformation and Shock-Induced Separation in Shock/Boundary-Layer Interactions. *AIAA Journal*, 55(12):4258–4273, 2017. doi: [10.2514/1.J056030](https://doi.org/10.2514/1.J056030).

- Candel, S. . Concorde and the Future of Supersonic Transport. *Journal of Propulsion and Power*, 20(1):59–68, 2004. doi: [10.2514/1.9180](https://doi.org/10.2514/1.9180).
- Causin, P. , Gerbeau, J.F. , and Nobile, F. . Added-Mass Effect in the Design of Partitioned Algorithms for Fluid–Structure Problems. *Computer Methods in Applied Mechanics and Engineering*, 194(42):4506 – 4527, 2005. doi: [10.1016/j.cma.2004.12.005](https://doi.org/10.1016/j.cma.2004.12.005).
- Chapman, D.R. , Kumen, D.M. , and Larson, H.K. . Investigation of Separated Flows in Supersonic and Subsonic Streams with Emphasis on the Effect of Transition. *NACA Technical Report 1356*, 1957.
- Chaudhuri, A. and Hadjadj, A. . Numerical Simulation of Transient Supersonic Nozzle Flows. 2012. doi: [10.2514/6.2012-952](https://doi.org/10.2514/6.2012-952).
- Cirak, F. , Deiterding, R. , and Mauch, S.P. . Large-Scale Fluid–Structure Interaction Simulation of Viscoplastic and Fracturing Thin-Shells Subjected to Shocks and Detonations. *Computers and Structures*, 85(11):1049 – 1065, 2007. doi: <https://doi.org/10.1016/j.compstruc.2006.11.014>.
- Clemens, N.T. and Narayanaswamy, V. . Low-Frequency Unsteadiness of Shock Wave/Turbulent Boundary Layer Interactions. *Annual Review of Fluid Mechanics*, 46(1):469–492, 2014. doi: [10.1146/annurev-fluid-010313-141346](https://doi.org/10.1146/annurev-fluid-010313-141346).
- Cousteix, J. . *Couche limite laminaire*. Cépaduès, 1988.
- Cousteix, J. . *Turbulence et couche limite*. Cépaduès, 1989.
- Culler, A.J. and McNamara, J.J. . Impact of Fluid-Thermal-Structural Coupling on Response Prediction of Hypersonic Skin Panels. *AIAA Journal*, 49(11):2393–2406, 2011. ISSN 0001-1452. doi: [10.2514/1.J050617](https://doi.org/10.2514/1.J050617).
- Daub, D. , Willems, S. , and Gülhan, A. . Experiments on the Interaction of a Fast-Moving Shock with an Elastic Panel. *AIAA Journal*, 54(2):670 – 678, 2015b. ISSN 0001-1452. doi: [10.2514/1.J054233](https://doi.org/10.2514/1.J054233).
- Davis, G. and Bendiksen, O. . Transonic Panel Flutter. In *34th Structures, Structural Dynamics and Materials Conference*, La Jolla, CA, U.S.A., 1993. American Institute of Aeronautics and Astronautics. doi: [10.2514/6.1993-1476](https://doi.org/10.2514/6.1993-1476).
- Dickens, J.M. , Nakagawa, J.M. , and Wittbrodt, M.J. . A Critique of Mode Acceleration and Modal Truncation Augmentation Methods for Modal Response Analysis. *Computers & Structures*, 62(6):985 – 998, 1997. ISSN 0045-7949. doi: [10.1016/S0045-7949\(96\)00315-X](https://doi.org/10.1016/S0045-7949(96)00315-X).
- Délery, J. and Dussauge, J.P. . Some Physical Aspects of Shock Wave/Boundary Layer Interactions. *Shock Waves*, 19(6):453 – 468, Jul 2009. ISSN 1432-2153. doi: [10.1007/s00193-009-0220-z](https://doi.org/10.1007/s00193-009-0220-z).
- Dolling, D.S. and Brusniak, L. . Separation Shock Motion in Fin, Cylinder, and Compression Ramp - Induced Turbulent Interactions. *AIAA Journal*, 27(6):734–742, 1989. doi: [10.2514/3.10173](https://doi.org/10.2514/3.10173).
- Dolling, D.S. and Erengil, M.E. . Unsteady Wave Structure near Separation in a Mach 5 Compression Ramp Interaction. *AIAA Journal*, 29(5):728–735, 1991. doi: [10.2514/3.10647](https://doi.org/10.2514/3.10647).
- Domaradzki, J.A. and Adams, N.A. . Direct Modelling of Subgrid Scales of Turbulence in Large Eddy Simulations. *Journal of Turbulence*, 3:N24, 2002. doi: [10.1088/1468-5248/3/1/024](https://doi.org/10.1088/1468-5248/3/1/024).
- Dowell, E.H. . Nonlinear Oscillations of a Fluttering Plate. *AIAA Journal*, 4(7):1267–1275, 07 1966. doi: [10.2514/3.3658](https://doi.org/10.2514/3.3658).
- Dowell, E.H. . Nonlinear Oscillations of a Fluttering Plate. II. *AIAA Journal*, 5(10):1856–1862, 1967. doi: [10.2514/3.4316](https://doi.org/10.2514/3.4316).
- Dowell, E.H. . Panel Flutter - a Review of the Aeroelastic Stability of Plates and Shells. *AIAA Journal*, 8(3): 385–399, 1970. ISSN 0001-1452. doi: [10.2514/3.5680](https://doi.org/10.2514/3.5680).
- Dowell, E.H. . Generalized Aerodynamic Forces on a Flexible Plate Undergoing Transient Motion in a Shear Flow with an Application to Panel Flutter. *AIAA journal*, 9(5):834–841, 1971. doi: [10.2514/3.6283](https://doi.org/10.2514/3.6283).

- Dowell, E.H. . Aerodynamic Boundary Layer Effects on Flutter and Damping of Plates. *Journal of Aircraft*, 10 (12):734–738, 12 1973. doi: [10.2514/3.60298](https://doi.org/10.2514/3.60298).
- Dowell, E.H. and Hall, K.C. . Modeling of Fluid-Structure Interaction. *Annual Review of Fluid Mechanics*, 33 (1):445–490, 2001. doi: [10.1146/annurev.fluid.33.1.445](https://doi.org/10.1146/annurev.fluid.33.1.445).
- Dowell, E.H. and Voss, H.M. . Theoretical and Experimental Panel Flutter Studies in the Mach Number Range 1.0 to 5.0. *AIAA Journal*, 3(12):2292–2304, 1965. ISSN 0001-1452. doi: [10.2514/3.3359](https://doi.org/10.2514/3.3359).
- Dupont, P. , Haddad, C. , and Debiève, J. F. . Space and Time Organization in a Shock-Induced Separated Boundary Layer. *Journal of Fluid Mechanics*, 559:255–277, 2006. doi: [10.1017/S0022112006000267](https://doi.org/10.1017/S0022112006000267).
- Erengil, M.E. and Dolling, D.S. . Physical Causes of Separation Shock Unsteadiness in Shock Wave Turbulent Boundary Layer Interactions. In *24th AIAA Fluid Dyn. Conf.*, Orlando, FL, 1993. AIAA 1993-3134.
- Farhat, C. and Lesoinne, M. . Two Efficient Staggered Algorithms for the Serial and Parallel Solution of Three-Dimensional Nonlinear Transient Aeroelastic Problems. *Computer Methods in Applied Mechanics and Engineering*, 182(3):499 – 515, 2000. doi: [10.1016/S0045-7825\(99\)00206-6](https://doi.org/10.1016/S0045-7825(99)00206-6).
- Farhat, C. , Lesoinne, M. , and Maman, N. . Mixed Explicit/Implicit Time Integration of Coupled Aeroelastic Problems: Three-Field Formulation, Geometric Conservation and Distributed Solution. *International Journal for Numerical Methods in Fluids*, 21(10):807–835, 1995. doi: [10.1002/flid.1650211004](https://doi.org/10.1002/flid.1650211004).
- Farhat, C. , Lesoinne, M. , and Le Tallec, P. . Load and Motion Transfer Algorithms for Fluid/Structure Interaction Problems with Non-Matching Discrete Interfaces: Momentum and Energy Conservation, Optimal Discretization and Application to Aeroelasticity. *Computer Methods in Applied Mechanics and Engineering*, 157(1):95 – 114, 1998. ISSN 0045-7825. doi: [10.1016/S0045-7825\(97\)00216-8](https://doi.org/10.1016/S0045-7825(97)00216-8).
- Farhat, C. , van der Zee, K.G. , and Geuzaine, P. . Provably second-order time-accurate loosely-coupled solution algorithms for transient nonlinear computational aeroelasticity. *Computer Methods in Applied Mechanics and Engineering*, 195(17):1973 – 2001, 2006. doi: [10.1016/j.cma.2004.11.031](https://doi.org/10.1016/j.cma.2004.11.031).
- Flaszynski, P. , Doerffer, P. , Szwaba, R. , and Kaczynski, M. , P. and Piotrowicz. Shock Wave Boundary Layer Interaction on Suction Side of Compressor Profile in Single Passage Test Section. *Journal of Thermal Science*, 24(6):510–515, Nov 2015. doi: [10.1007/s11630-015-0816-9](https://doi.org/10.1007/s11630-015-0816-9).
- Fung, Y.C. . *Foundations of Solid Mechanics*. International Series in Dynamics. Prentice Hall, 1965. ISBN 9780133299120.
- Gan, J. and Zha, G. . Delayed Detached Eddy Simulation of Supersonic Panel Aeroelasticity Using Fully Coupled Fluid Structure Interaction with High Order Schemes. In *34th AIAA Applied Aerodynamics Conference*, Washington, D.C., 2016. AIAA 2016-4046. doi: [10.2514/6.2016-4046](https://doi.org/10.2514/6.2016-4046).
- Ganapathisubramani, B. , Clemens, N. T. , and Dolling, D. S. . Low-Frequency Dynamics of Shock-Induced Separation in a Compression Ramp Interaction. *Journal of Fluid Mechanics*, 636:397–425, 2009. doi: [10.1017/S0022112009007952](https://doi.org/10.1017/S0022112009007952).
- Garnier, E. , Adams, N. , and Sagaut, P. . *Large Eddy Simulation for Compressible Flows*. Scientific Computation. Springer Netherlands, 2009. doi: [10.1007/978-90-481-2819-8](https://doi.org/10.1007/978-90-481-2819-8).
- Geurts, B.J. . Inverse Modeling for Large-Eddy Simulation. *Physics of Fluids*, 9(12):3585–3587, 1997. doi: [10.1063/1.869495](https://doi.org/10.1063/1.869495).
- Giepman, R.H.M , Schrijer, F.F.J. , and van Oudheusden, B.W. . Flow Control of an Oblique Shock Wave Reflection with Micro-Ramp Vortex Generators: Effects of Location and Size. *Physics of Fluids*, 26, 2014. doi: [10.1063/1.4881941](https://doi.org/10.1063/1.4881941).
- Gogulapati, A. , Deshmukh, R. , Crowell, A.R. , McNamara, J.J. , Vyas, V. , Wang, X.Q. , Mignolet, M. , Bebernis, T. , Spottswood, S.M. , and Eason, T.G. . Response of a Panel to Shock Impingement: Modeling and Comparison with Experiments. In *55th AIAA/ASME/ASCE/AHS/ASC Structures, Structural Dynamics, and Materials Conference*. AIAA 2014-0148, 2014. doi: [10.2514/6.2014-0148](https://doi.org/10.2514/6.2014-0148).

- Gogulapati, A. , Deshmukh, R. , McNamara, J.J. , Vyas, V. , Wang, X.Q. , Mignolet, M. , Beberniss, T. , Spottswood, S.M. , and Eason, T.G. . Response of a Panel to Shock Impingement: Modeling and Comparison with Experiments - Part 2. In *56th AIAA/ASCE/AHS/ASC Structures, Structural Dynamics, and Materials Conference*. AIAA 2015-0685, 2015. doi: [10.2514/6.2015-0685](https://doi.org/10.2514/6.2015-0685).
- Gordnier, R.E. and Visbal, M.R. . Development of a Three-Dimensional Viscous Aeroelastic Solver for Nonlinear Panel Flutter. *Journal of Fluids and Structures*, 16(4):497– 527, 2002. ISSN 0889-9746. doi: [10.1006/jfls.2000.0434](https://doi.org/10.1006/jfls.2000.0434).
- Gottlieb, S. and Shu, C.-W. . Total Variation Diminishing Runge-Kutta Schemes. *Mathematics of Computation*, 67(221):73–85, 1998.
- Grilli, M. , Schmid, P.J. , Hickel, S. , and Adams, N.A. . Analysis of Unsteady Behaviour in Shockwave Turbulent Boundary Layer Interaction. *Journal of Fluid Mechanics*, 700:16–28, 2012. doi: [10.1017/jfm.2012.37](https://doi.org/10.1017/jfm.2012.37).
- Grilli, M. , Hickel, S. , and Adams, N.A. . Large-Eddy Simulation of a Supersonic Turbulent Boundary Layer over a Compression–Expansion Ramp. *International Journal of Heat and Fluid Flow*, 42:79 – 93, 2013. doi: [10.1016/j.ijheatfluidflow.2012.12.006](https://doi.org/10.1016/j.ijheatfluidflow.2012.12.006).
- Grossman, I.J. and Bruce, P.J.K. . Confinement Effects on Regular–Irregular Transition in Shock-Wave–Boundary-Layer Interactions. *Journal of Fluid Mechanics*, 853:171–204, 2018. doi: [10.1017/jfm.2018.537](https://doi.org/10.1017/jfm.2018.537).
- Guo, X. and Mei, C. . Application of Aeroelastic Modes on Nonlinear Supersonic Panel Flutter at Elevated Temperatures. *Computers and Structures*, 84(24):1619 – 1628, 2006. ISSN 0045-7949. doi: [10.1016/j.compstruc.2006.01.041](https://doi.org/10.1016/j.compstruc.2006.01.041).
- Guobiao, C. , Dingqiang, Z. , and Xiaoying, Z. . Coupling Simulation of Heat Transfer and Temperature of the Composite Walled Nozzle of Rocket. In *2007 IEEE Aerospace Conference*, pages 1–12, 2007.
- Hadjadj, A. . Large-Eddy Simulation of Shock/Boundary-Layer Interaction. *AIAA Journal*, 50(12):2919–2927, 2012. doi: [10.2514/1.J051786](https://doi.org/10.2514/1.J051786).
- Hadjadj, A. , Perrot, Y. , and Verma, S. . Numerical Study of Shock/Boundary Layer Interaction in Supersonic Overexpanded Nozzles. *Aerospace Science and Technology*, 42:158 – 168, 2015. ISSN 1270-9638. doi: [10.1016/j.ast.2015.01.010](https://doi.org/10.1016/j.ast.2015.01.010).
- Hashimoto, A. , N., Yagi. , and Nakamura, Y. . Effects of Boundary Layer on Supersonic Panel Flutter. *Journal of the Japan Society for Aeronautical and Space Sciences*, 55(639):159–164, 2007. doi: [10.2322/jjsass.55.159](https://doi.org/10.2322/jjsass.55.159).
- Hashimoto, A. , Aoyama, T. , and Nakamura, Y. . Effects of Turbulent Boundary Layer on Panel Flutter. *AIAA Journal*, 47(12):2785–2791, 2009. doi: [10.2514/1.35786](https://doi.org/10.2514/1.35786).
- Hedgepeth, J.M. . Flutter of Rectangular Simply Supported Panels at High Supersonic Speeds. *Journal of the Aeronautical Sciences*, 24(8):563–573, 1957. doi: [10.2514/8.3908](https://doi.org/10.2514/8.3908).
- Hickel, S. and Larsson, J. . An Adaptive Local Deconvolution Model for Compressible Turbulence. In *Proceedings of the 2008 Summer Program*, pages 85–96, 2008.
- Hickel, S. , Adams, N.A. , and Domaradzki, J.A. . An Adaptive Local Deconvolution Method for Implicit LES. *Journal of Computational Physics*, 213(1):413 – 436, 2006. ISSN 0021-9991. doi: [10.1016/j.jcp.2005.08.017](https://doi.org/10.1016/j.jcp.2005.08.017).
- Hickel, S. , Adams, N. A. , and Mansour, N. N. . Implicit subgrid-scale modeling for large-eddy simulation of passive-scalar mixing. *Physics of Fluids*, 19(9):095102, 2007. doi: [10.1063/1.2770522](https://doi.org/10.1063/1.2770522).
- Hickel, S. , Egerer, C.P. , and Larsson, J. . Subgrid-scale modeling for implicit large eddy simulation of compressible flows and shock-turbulence interaction. *Physics of Fluids*, 26(10):106101, 2014. doi: [10.1063/1.4898641](https://doi.org/10.1063/1.4898641).
- Hilber, H. M. , Hughes, T. J. R. , and Taylor, R. L. . Improved Numerical Dissipation for Time Integration Algorithms in Structural Dynamics. *Earthquake Engineering & Structural Dynamics*, 5(3):283–292, 1977. doi: [10.1002/eqe.4290050306](https://doi.org/10.1002/eqe.4290050306).

- Houbolt, J.C. . *A Study of Several Aerothermoelastic Problems of Aircraft Structures in High-Speed Flight*. PhD thesis, ETH Zürich, 1958.
- Hu, X.Y. , Khoo, B.C. , Adams, N.A. , and Huang, F.L. . A Conservative Interface Method for Compressible Flows. *Journal of Computational Physics*, 219(2):553 – 578, 2006. doi: [10.1016/j.jcp.2006.04.001](https://doi.org/10.1016/j.jcp.2006.04.001).
- Humble, R. A. , Elsinga, G. E. , Scarano, F. , and van Oudheusden, B. W. . Three-Dimensional Instantaneous Structure of a Shock Wave/Turbulent Boundary Layer Interaction. *Journal of Fluid Mechanics*, 622:33–62, 2009. doi: [10.1017/S0022112008005090](https://doi.org/10.1017/S0022112008005090).
- Hurwitz, A. . Ueber die Bedingungen, unter welchen eine Gleichung nur Wurzeln mit negativen reellen Theilen besitzt. *Mathematische Annalen*, 46(2):273–284, Jun 1895. ISSN 1432-1807. doi: [10.1007/BF01446812](https://doi.org/10.1007/BF01446812).
- Idris, A.C. , Saad, M.R. , Zare-Behtash, H. , and Kontis, K. . Luminescent Measurement Systems for the Investigation of a Scramjet Inlet-Isolator. *Sensors (Basel, Switzerland)*, 14:6606–6632, 04 2014. doi: [10.3390/s140406606](https://doi.org/10.3390/s140406606).
- Jinks, E.R. , Bruce, P.J. , and Santer, M.J. . Wind Tunnel Experiments with Flexible Plates in Transonic Flows. In *54th AIAA Aerospace Sciences Meeting*, San Diego, California, 2016. AIAA 2016-1553. doi: [10.2514/6.2016-1553](https://doi.org/10.2514/6.2016-1553).
- Kallarail, N.S. . The 3D Separation Behaviour of a Micro-Ramp Controlled Oblique Shock-Wave Reflection, 2016.
- Karagiozis, K. , Kamakoti, R. , Cirak, F. , and Pantano, C. . A Computational Study of Supersonic Disk-Gap-Band Parachutes using Large-Eddy Simulation Coupled to a Structural Membrane. *Journal of Fluids and Structures*, 27(2):175 – 192, 2011. doi: [10.1016/j.jfluidstructs.2010.11.007](https://doi.org/10.1016/j.jfluidstructs.2010.11.007).
- Klein, M. , Sadiki, A. , and Janicka, J. . A Digital Filter Based Generation of Inflow Data for Spatially Developing Direct Numerical or Large Eddy Simulations. *Journal of Computational Physics*, 186(2):652 – 665, 2003. doi: [10.1016/S0021-9991\(03\)00090-1](https://doi.org/10.1016/S0021-9991(03)00090-1).
- Knight, D. , Yan, H. , Panaras, A.G. , and Zheltovodov, A. . Advances in CFD Prediction of Shock Wave Turbulent Boundary Layer Interactions. *Progress in Aerospace Sciences*, 39(2):121–184, 2003. ISSN 0376-0421. doi: [10.1016/S0376-0421\(02\)00069-6](https://doi.org/10.1016/S0376-0421(02)00069-6).
- Knight, D.D. and Degrez, G. . Shock Wave Boundary Layer Interactions in High Mach Number Flows - a Critical Survey of Current Numerical Prediction Capabilities. *AGARD Advisor Report*, 2(319):1–35, 1998.
- Kravchenko, A.G. and Moin, P. . On the Effect of Numerical Errors in Large Eddy Simulations of Turbulent Flows. *Journal of Computational Physics*, 131(2):310–322, 1997. doi: [10.1006/jcph.1996.5597](https://doi.org/10.1006/jcph.1996.5597).
- Kuerten, J. G. M. , Geurts, B. J. , Vreman, A. W. , and Germano, M. . Dynamic Inverse Modeling and its Testing in Large-Eddy Simulations of the Mixing Layer. *Physics of Fluids*, 11(12):3778–3785, 1999. doi: [10.1063/1.870238](https://doi.org/10.1063/1.870238).
- Laurenson, M.R. and McPherson, I.J. . Design Procedures for Flutter-Free Surface Panels. (NASA CR-2801), 03 1977.
- Leissa, A.W. . Vibration of Plates. (NASA-SP-160), 1969.
- Leonard, A. . Energy Cascade in Large-Eddy Simulations of Turbulent Fluid Flows. In *Turbulent Diffusion in Environmental Pollution*, volume 18 of *Advances in Geophysics*, pages 237 – 248. Elsevier, 1975. doi: [10.1016/S0065-2687\(08\)60464-1](https://doi.org/10.1016/S0065-2687(08)60464-1).
- Li, H. and Ben-Dor, G. . A Parametric Study of Mach Reflection in Steady Flows. *Journal of Fluid Mechanics*, 341:101–125, 1997.
- Lighthill, M.J. . Oscillating Airfoils at High Mach Number. *Journal of the Aeronautical Sciences*, 20(6):402–406, 1953. doi: [10.2514/8.2657](https://doi.org/10.2514/8.2657).

- Loginov, M.S. , Adams, N.A. , and Zheltovodov, A.A. . Large-Eddy Simulation of Shock-Wave/Turbulent-Boundary-Layer Interaction. *Journal of Fluid Mechanics*, 565:135–169, 2006. doi: [10.1017/S0022112006000930](https://doi.org/10.1017/S0022112006000930).
- Lu, F.K. . Quasiconical Free Interaction Between a Swept Shock and a Turbulent Boundary Layer. 31(4):686–692, 1993. doi: [10.2514/3.11604](https://doi.org/10.2514/3.11604).
- Matheis, J. and Hickel, S. . On the Transition between Regular and Irregular Shock Patterns of Shock-Wave/Boundary-Layer Interactions. *Journal of Fluid Mechanics*, 776:200–234, 2015. doi: [10.1017/jfm.2015.319](https://doi.org/10.1017/jfm.2015.319).
- Mei, C. , Abdel-Motagaly, K. , and Chen, R. . Review of Nonlinear Panel Flutter at Supersonic and Hypersonic Speeds. *Applied Mechanics Reviews*, 52(10):321 – 332, 01 1999. ISSN 0003-6900. doi: [10.1115/1.3098919](https://doi.org/10.1115/1.3098919).
- Mei, G. , Zhang, J. , Xi, G. , Sun, X. , and Chen, J. . Analysis of Supersonic and Transonic Panel Flutter Using a Fluid-Structure Coupling Algorithm. *Journal of Vibration and Acoustics*, 136(3):031013–031013–11, 2014. doi: [10.1115/1.4027135](https://doi.org/10.1115/1.4027135).
- Meyer, M. , Devesa, A. , Hickel, S. , Hu, X.Y. , and Adams, N.A. . A Conservative Immersed Interface Method for Large-Eddy Simulation of Incompressible Flows. *Journal of Computational Physics*, 229(18):6300 – 6317, 2010. doi: [10.1016/j.jcp.2010.04.040](https://doi.org/10.1016/j.jcp.2010.04.040).
- Miller, B. , Crowell, A. , and McNamara, J. . Modeling and Analysis of Shock Impingements on Thermo-Mechanically Compliant Surface Panels. In *53rd AIAA/ASME/ASCE/AHS/ASC Structures, Structural Dynamics and Materials Conference*. AIAA 2012-1548, 2012. doi: [10.2514/6.2012-1548](https://doi.org/10.2514/6.2012-1548).
- Mittal, R. , Dong, H. , Bozkurttas, M. , Najjar, F.M. , Vargas, A. , and von Loebbecke, A. . A Versatile Sharp Interface Immersed Boundary Method for Incompressible Flows with Complex Boundaries. *Journal of Computational Physics*, 227(10):4825 – 4852, 2008. ISSN 0021-9991. doi: [10.1016/j.jcp.2008.01.028](https://doi.org/10.1016/j.jcp.2008.01.028).
- Morgan, B. , Duraisamy, K. , Nguyen, N. , Kawai, S. , and Lele, S. K. . Flow Physics and RANS Modelling of Oblique Shock/Turbulent Boundary Layer Interaction. *Journal of Fluid Mechanics*, 729:231–284, 2013. doi: [10.1017/jfm.2013.301](https://doi.org/10.1017/jfm.2013.301).
- Muhlstein, L. , Gaspers, P.A. , and Riddle, D. . An Experimental Study of the Influence of the Turbulent Boundary Layer on Panel Flutter. (NASA-TN-D-4486), 1968.
- Nayak, K. , Giepmans, R.H.M. , Schrijer, F.F.J. , and van Oudheusden, B.W. . Tomographic-PIV investigation of the 3D Separation Behaviour of a Micro-Ramp Controlled SWBLI. In *52nd 3AF International Conference on Applied Aerodynamics*, 2017.
- Nichols, J.W. , Larsson, J. , Bernardini, M. , and Pirozzoli, S. . Stability and Modal Analysis of Shock-/Boundary Layer Interactions. *Theoretical and Computational Fluid Dynamics*, 31(1):33–50, 2016. doi: [10.1007/s00162-016-0397-6](https://doi.org/10.1007/s00162-016-0397-6).
- Nilsson, A. and Liu, B. . *Vibro-Acoustics, Volume 1*. Springer-Verlag Berlin Heidelberg, 2015. doi: [10.1007/978-3-662-47807-3](https://doi.org/10.1007/978-3-662-47807-3).
- Örley, F. , Pasquariello, V. , Hickel, S. , and Adams, N.A. . Cut-element Based Immersed Boundary Method for Moving Geometries in Compressible Liquid Flows with Cavitation. *Journal of Computational Physics*, 283: 1–22, 2015. ISSN 0021-9991. doi: [10.1016/j.jcp.2014.11.028](https://doi.org/10.1016/j.jcp.2014.11.028).
- Östlund, J. and Muhammad-Klingmann, B. . Supersonic Flow Separation with Application to Rocket Engine Nozzles. *Applied Mechanics Reviews*, 58:143 – 177, 2005. ISSN 0003-6900. doi: [10.1115/1.1894402](https://doi.org/10.1115/1.1894402).
- Pasquariello, V. . *Analysis and Control of Shock-Wave/Turbulent Boundary-Layer Interactions on Rigid and Flexible Walls*. PhD thesis, Technische Universität München, 2018.
- Pasquariello, V. , Hickel, S. , and Adams, N.A. . Extension of the Conservative Immersed Interface Method towards high-order interpolation. In *Sonderforschungsbereich/Transregio 40 - Annual Report*, pages 269–278, 2013.

- Pasquariello, V. , Grilli, M. , Hickel, S. , and Adams, N.A. . Large-Eddy Simulation of Passive Shock-Wave/Boundary-Layer Interaction Control. *International Journal of Heat and Fluid Flow*, 49:116 – 127, 2014. ISSN 0142-727X. doi: [10.1016/j.ijheatfluidflow.2014.04.005](https://doi.org/10.1016/j.ijheatfluidflow.2014.04.005). 8th Symposium on Turbulence and Shear Flow Phenomena (TSFP8).
- Pasquariello, V. , Hickel, S. , Adams, N. , Hammerl, G. , Wall, W. , Daub, D. , Willems, S. , and Gülhan, A. . Coupled Simulation of Shock-Wave/Turbulent Boundary-Layer Interaction over a Flexible Panel. In *6th European Conference for Aeronautics and Space Sciences*, Krakau, 06 2015.
- Pasquariello, V. , Hammerl, G. , Öerley, E. , Hickel, S. , Danowski, C. , Popp, A. , Wall, W. , and Adams, N. . A Cut-Cell Finite Volume - Finite Element Coupling Approach for Fluid-Structure Interaction in Compressible Flow. *Journal of Computational Physics*, 307:670–695, 11 2016. doi: [10.1016/j.jcp.2015.12.013](https://doi.org/10.1016/j.jcp.2015.12.013).
- Pasquariello, V. , Hickel, S. , and Adams, N.A. . Unsteady Effects of Strong Shock-Wave/Boundary-Layer Interaction at High Reynolds Number. *Journal of Fluid Mechanics*, 823:617–657, 2017. doi: [10.1017/jfm.2017.308](https://doi.org/10.1017/jfm.2017.308).
- Piponniau, S. , Dussauge, J. P. , Debiève, J. E. , and Dupont, P. . A Simple Model for Low-Frequency Unsteadiness in Shock-Induced Separation. *Journal of Fluid Mechanics*, 629:87–108, 2009. doi: [10.1017/S0022112009006417](https://doi.org/10.1017/S0022112009006417).
- Pirozzoli, S. and Grasso, F. . Direct Numerical Simulation of Impinging Shock Wave/Turbulent Boundary Layer Interaction at  $M=2.25$ . *Physics of Fluids*, 18(6):065–113, 2006. doi: [10.1063/1.2216989](https://doi.org/10.1063/1.2216989).
- Pirozzoli, S. , Beer, A. , Bernardini, M. , and Grasso, F. . Computational Analysis of Impinging Shock-Wave Boundary Layer Interaction under Conditions of Incipient Separation. *Shock Waves*, 19:487–497, 2009. doi: [10.1007/s00193-009-0215-9](https://doi.org/10.1007/s00193-009-0215-9).
- Pirozzoli, S. , Larsson, J. , Nichols, J.W. , Morgan, B.E. , and Lele, S.K. . Analysis of Unsteady Effects in Shock-/Boundary Layer Interactions. In *Proceedings of the 2010 CTR Summer Program*, Stanford, 2010. Center of Turbulence Research.
- Plotkin, K.J. . Shock Wave Oscillation Driven by Turbulent Boundary-Layer Fluctuations. *AIAA Journal*, 13(8): 1036–1040, 1975. doi: [10.2514/3.60501](https://doi.org/10.2514/3.60501).
- Priebe, S. , Wu, M. , and Martín, M.P. . Direct Numerical Simulation of a Reflected-Shock-Wave/Turbulent-Boundary-Layer Interaction. *AIAA Journal*, 47(5):1173–1185, 2009. doi: [10.2514/1.38821](https://doi.org/10.2514/1.38821).
- Priebe, S. , Tu, J. H. , Rowley, C.W. , and Martín, M. P. . Low-Frequency Dynamics in a Shock-Induced Separated Flow. *Journal of Fluid Mechanics*, 807:441–477, 2016. doi: [10.1017/jfm.2016.557](https://doi.org/10.1017/jfm.2016.557).
- Prony, R. . Essai Expérimental et Analytique Sur les Lois de la Dilatabilité des Fluides élastiques, et sur Celles de la Force Expansive de la Vapeur de l'Eau et de la Vapeur de l'Alcool, á Différentes Temperatures. *Journal de l'École Polytechnique Floréal et Plairial*, 1(22):24–76, 1795.
- Rabey, P.K. and Bruce, P.J. . Experimental 3D Mapping of Reflected Shock - Boundary Layer Interaction Unsteadiness. 01 2019. doi: [10.2514/6.2019-0341](https://doi.org/10.2514/6.2019-0341).
- Rodríguez, A.F. , Rodrigo, L.d.S. , Guillén, E.L. , Rodríguez, J.M.R. , Jiménez, J.M.M. , and Boquete, L. . Coding Prony's Method in MATLAB and Applying it to Biomedical Signal Filtering. *BMC BioInformatics*, 19(1):451, 2018.
- Routh, E.J. . A Treatise on the Stability of a Given State of Motion: Particularly Steady Motion. *Macmillan*, 1877. doi: [10.3390/s140406606](https://doi.org/10.3390/s140406606).
- Shapiro, A.H. and Shapiro, R.E. . *The Dynamics and Thermodynamics of Compressible Fluid Flow*. John Wiley and Sons Inc, 1987. ISBN 9780471066910.
- Shine, S.R. and Nidhi, S.S. . Review on Film Cooling of Liquid Rocket Engines. *Propulsion and Power Research*, 7(1):1 – 18, 2018. ISSN 2212-540X. doi: [10.1016/j.jprr.2018.01.004](https://doi.org/10.1016/j.jprr.2018.01.004).

- Spottswood, S.M. , Eason, T.G. , and Beberniss, T. . Influence of Shock-Boundary Layer Interactions on the Dynamic Response of a Flexible Panel. In *Proceedings of the ISMA-2012, 17-19 September, Leuven, Belgium*, pages 603 – 616, 2012.
- Spottswood, S.M. , Eason, T.G. , and Beberniss, T. . Full-Field, Dynamic Pressure and Displacement Measurements of a Panel Excited by Shock Boundary-Layer Interaction. In *19th AIAA/CEAS Aeroacoustics Conference*. American Institute of Aeronautics and Astronautics, 2013. doi: [10.2514/6.2013-2016](https://doi.org/10.2514/6.2013-2016).
- Steinrück, H. . *Asymptotic Methods in Fluid Mechanics: Survey and Recent Advances*. CISM International Centre for Mechanical Sciences. Springer-Verlag, 2011. ISBN 978-3-7091-1690-6. doi: [10.1007/978-3-7091-0408-8](https://doi.org/10.1007/978-3-7091-0408-8).
- Stewartson, K. and Williams, P.G. . Self-Induced Separation. *Proceedings of the Royal Society of London A: Mathematical, Physical and Engineering Sciences*, 312(1509):181–206, 1969. ISSN 0080-4630. doi: [10.1098/rspa.1969.0148](https://doi.org/10.1098/rspa.1969.0148).
- Stolz, S. and Adams, N. A. . An Approximate Deconvolution Procedure for Large-Eddy Simulation. *Physics of Fluids*, 11(7):1699–1701, 1999. doi: [10.1063/1.869867](https://doi.org/10.1063/1.869867).
- Sun, Z. . *Micro Ramps in Supersonic Turbulent Boundary Layers: An Experimental and Numerical Study*. PhD thesis, Faculty of Aerospace Engineering, TU Delft, 2014.
- Sun, Z. , Schrijer, F.F.J. , Scarano, F. , and van Oudheusden, B.W. . The Three-Dimensional Flow Organization past a Micro-Ramp in a Supersonic Boundary Layer. *Physics of Fluids*, 24(5), 2012. doi: [10.1063/1.4711372](https://doi.org/10.1063/1.4711372).
- Tambe, S. , Schrijer, F.F.J. , and van Oudheusden, B.W. . Effect of Geometry on the Downstream Flow Topology of a Micro Ramp in a Supersonic Turbulent Boundary Layer: An experimental Study. In *7th European Conference For Aeronautics And Space Sciences*, 2017.
- Thari, A. , Pasquariello, V. , Aage, N. , and Hickel, S. . Adaptive Reduced-Order Modeling for Non-Linear Fluid-Structure Interaction. 02 2017.
- Thomas, F.O. , Putnam, C.M. , and Chu, H.C. . On the Mechanism of Unsteady Shock Oscillation in Shock Wave/Turbulent Boundary Layer Interactions. *Experiments in Fluids*, 18(1):69–81, 1994. doi: [10.1007/BF00209362](https://doi.org/10.1007/BF00209362).
- Threadgill, J.A. and Bruce, P.J.K. . Comparison of Unsteady Flow Similarities in Various Shock/Boundary-Layer Interaction Configurations. In *55th AIAA Aerospace Sciences Meeting*, 2017. doi: [10.2514/6.2017-0986](https://doi.org/10.2514/6.2017-0986).
- Touber, E. and Sandham, N. D. . Low-Order Stochastic Modelling of Low-Frequency Motions in Reflected Shock-Wave/Boundary-Layer Interactions. *Journal of Fluid Mechanics*, 671:417–465, 2011. doi: [10.1017/S0022112010005811](https://doi.org/10.1017/S0022112010005811).
- Touber, E. and Sandham, N.D. . Large-Eddy Simulation of Low-Frequency Unsteadiness in a Turbulent Shock-Induced Separation Bubble. *Theoretical and Computational Fluid Dynamics*, 23(2):79–107, 2009. doi: [10.1007/s00162-009-0103-z](https://doi.org/10.1007/s00162-009-0103-z).
- Visbal, M.R. . On the Interaction of an Oblique Shock with a Flexible Panel. *Journal of Fluids and Structures*, 30:219 – 225, 2012. ISSN 0889-9746. doi: [10.1016/j.jfluidstructs.2012.02.002](https://doi.org/10.1016/j.jfluidstructs.2012.02.002).
- Visbal, M.R. . Viscous and Inviscid Interactions of an Oblique Shock with a Flexible Panel. *Journal of Fluids and Structures*, 48:27 – 45, 2014. ISSN 0889-9746. doi: [10.1016/j.jfluidstructs.2014.02.003](https://doi.org/10.1016/j.jfluidstructs.2014.02.003).
- Vreman, B. , Geurts, B. , and Kuerten, H. . A Priori Tests of Large Eddy Simulation of the Compressible Plane Mixing Layer. *Journal of Engineering Mathematics*, 29(4):299–327, 1995. doi: [10.1007/BF00042759](https://doi.org/10.1007/BF00042759).
- Wang, B. , Sandham, N.D. , Hu, Z. , and Liu, W. . Numerical Study of Oblique Shock-Wave/Boundary-Layer Interaction Considering Sidewall Effects. *Journal of Fluid Mechanics*, 767:526–561, 2015. doi: [10.1017/jfm.2015.58](https://doi.org/10.1017/jfm.2015.58).
- Wang, T.S. and Guidos, M.J. . Transient Three-Dimensional Side-Load Analysis of a Film-Cooled Nozzle. *Journal of Propulsion and Power*, 25(6):1272 – 1280, 2009. ISSN 0748-4658. doi: [10.2514/1.41025](https://doi.org/10.2514/1.41025).

- Wu, M. and Martín, M.P. . Analysis of Shock Motion in Shockwave and Turbulent Boundary Layer Interaction using Direct Numerical Simulation Data. *Journal of Fluid Mechanics*, 594:71–83, 2008. doi: [10.1017/S0022112007009044](https://doi.org/10.1017/S0022112007009044).
- Ye, L. and Ye, Z. . Effects of Shock Location on Aeroelastic Stability of Flexible Panel. *AIAA Journal*, pages 1 – 13, 2018. doi: [10.2514/1.J056924](https://doi.org/10.2514/1.J056924).
- Ye, L. , Ye, Z. , and Wang, X. . Aeroelastic Stability Analysis of Heated Flexible Panel Subjected to an Oblique Shock. *Chinese Journal of Aeronautics*, 2018. ISSN 10009361. doi: [10.1016/j.cja.2018.05.019](https://doi.org/10.1016/j.cja.2018.05.019).
- Zauner, M. . Large-Eddy Simulation of a Turbulent Shock-Wave/Boundary-Layer Interaction over a Flexible Panel, 2015.
- Zhou, J. , Yang, Z. , and Gu, Y. . Aeroelastic Stability Analysis of Heated Panel with Aerodynamic Loading on Both Surfaces. *Science China Technological Sciences*, 55(10):2720 – 2726, 2012. doi: [10.1007/s11431-012-4942-2](https://doi.org/10.1007/s11431-012-4942-2).